Staggered and In-line Submerged Jet Arrays for Power Electronics Using Variable Area Discharge Manifolds

by

Michael Andrew Henry

A thesis submitted to the Graduate Faculty of
Auburn University
in partial fulfillment of the
requirements for the Degree of
Master of Science

Auburn, Alabama
August 4, 2018

Keywords: jet impingement, single-phase, spent flow management,
local heat transfer coefficient measurement, water-ethylene glycol, staggered arrays

Approved by

Sushil H. Bhavnani, Co-Chair, Professor of Mechanical Engineering
Roy W. Knight, Co-Chair, Associate Professor of Mechanical Engineering
Daniel K. Harris, Associate Professor of Mechanical Engineering

Abstract

Power electronics packages in electric and hybrid vehicles require dedicated and dynamic cooling to perform reliably. Generally, such packages are designed to spread heat to a large surface area, and employing the radiator flow loop and fluid to provide a more aggressive, liquid-cooling approach to supplement heat spreaders is an appealing idea when considering cost, design, and fabrication. An array of liquid jets is the best single-phase cooling technique for cooling large surfaces. The highest regions of cooling in an array of jets are located at the stagnation points and, to a lesser degree, the fountain regions. One of the more significant issues facing arrays of jets is the degradation of downstream jets caused by the interference of fluid spent by upstream jets. The idea of an angled confining wall to divert the spent flow, and therefore prevent the entrainment of flows, was complemented by investigations into the viability of water-ethylene glycol as a working fluid and staggered arrays. A measurement technique was used to determine the local thermal characteristics for cases of varying jet Reynolds number, plate angle, jet-to-jet pitch, and jet-to-plate height above the surface. Water-ethylene glycol and staggered arrays were compatible and showed improved heat transfer when combined with the angled wall spent fluid management scheme.

Acknowledgements

Thanks go to the members of my advisory committee, Dr. Sushil H. Bhavnani, Dr. Roy W. Knight, and Dr. Daniel K. Harris, for serving upon it. Dr. Bhavnani and Dr. Knight warrant special thanks for the counsel and guidance they've provided in the course of this study.

Thanks go to Dr. John F. Maddox for laying the foundations of this project, and for serving in an auxiliary role for troubleshooting technical issues and tailoring their solutions.

Thanks go to Kayla and Sriram for rounding out a triumvirate, serving as colleagues in times of both academic perseverance and shared comradery.

Finally, thanks go to my mother, father, brother, sister, and grandmother, who were essential throughout this work, and without whom all the steps beforehand would have been impossible.

Table of Contents

Abstract ii

Acknowledgements iii

List of Figures vii

List of Tables x

Nomenclature xi

1 Introduction and Theory 1

1.1 Electronics Thermal Management Considerations 1

1.2 Applicability of Power Electronics Cooling Techniques 3

1.3 Jet Theory 4

1.3.1 Jet Regions 5

2 Literature Review 7

3 Experimental Setup and Procedures 14

3.1 Jet Plates 14

3.2 Flow Chamber and Heat Generation 17

3.3 Flow Loop 19

3.4 Local and Average Surface Measurements 21

4 Results 25

4.1 Overview of Parameters Tested 25

4.1.1 Water-Ethylene Glycol Tests 25

4.1.2 Staggered Array Tests 26

4.2 Water-Ethylene Glycol Results and Discussion 29

4.3 Staggered Array Results and Discussion 33

4.4 Numerical Comparison 39

5 Conclusion 42

5.1 Suggestions for Future Work 44

Bibliography 46

Appendices 50

A Data Acquisition 50

A.1 Procedure 50

A.1.1 Opening the Flow Chamber. 50

A.1.2 Closing the Flow Chamber 51

A.1.3 Replacing the Jet Plate 51

A.1.4 Translating in the *x*-direction 52

A.1.5 Translating in the y-direction. 53

A.1.6 Changing the Height of the Jet Plate 53

A.1.7 Initializing the System 54

A.2 Considerations for Potential Revisions to the Test Chamber Design 54

B Data Reduction 57

B.1 Calculating Local Surface Values 57

B.2 Calculating Average Surface Values 63

C Experimental Uncertainty Analysis 69

C.1 Determining Thermocouple Uncertainty Using Sequential Perturbations 69

C.2 Local Surface Measurement Uncertainties 71

C.3 Surface Average Measurement Uncertainties 72

D Experimental Results 73

D.1 Experimental Data Summary 73

D.2 Experimental Surface Maps 75

List of Figures

IGBT module 2

Overheated module 3

Types of jets 5

Regions of impinging jets 6

Rholfs et. al. [14] thermochromatic liquid crystals. 8

Brunschwiler et. al. [9] flow geometry. 9

Arens et. al. [22] jet arrays with and without variable diameter 10

3.1 Spatial arrangement jet array types 15

(a) Inline 15

(b) Streamwise staggered 15

(c) Transverse staggered 16

3.2 Side view of the angled manifold region 16

3.3 Photograph of 3D-printed jet plates 17

3.4 Cross section of experimental apparatus 18

3.5 Cross section of copper blocks 19

3.6 Flow loop 20

3.7 Photograph of experimental apparatus 21

3.8 Surface map locations 23

4.1 Varying patterns for staggered arrays 26

4.2 Surface maps of water-ethylene glycol at increasing flow rates 29

4.3 Average heat transfer coefficients for water and water-ethylene glycol 30

4.4 Average Nusselt numbers for water and water-ethylene glycol 31

4.5 Surface maps of water-ethylene glycol at increasing manifold angle 32

4.6 Temperature rise surface maps for varying nozzle pattern 34

4.7 Average Nusselt numbers for varying angle and nozzle pattern 35

4.8 Surface maps of staggered plates at increasing angle 36

4.9 Nusselt numbers for varying angle and pitch using plates with the streamwise staggered pattern 37

4.10 Nusselt numbers comparing test with pitch, $P^* = 3$. 38

4.11 Comparison of numerical and experimental surface plots. 40

D.1 Water-ethylene glycol over increasing Reynolds numbers 76

D.2 Water-ethylene glycol over increasing manifold angle. 77

D.3 Water-ethylene glycol with $H^* = 1$ and 2 78

D.4 Streamwise staggered array with $P^* = 3$ and increasing Reynolds number 79

D.5 Streamwise staggered array with $P^* = 4$ and increasing Reynolds number. 80

D.6 Streamwise staggered array with $P^* = 6$ and increasing Reynolds number 81

D.7 Transverse staggered array with $P^* = 6$ and increasing Reynolds number 82

D.8 Streamwise staggered arrays with increasing pitch. 83

D.9 Streamwise staggered compared to transverse staggered 84

D.10 Streamwise staggered increasing angle with $P^* = 4$. 85

D.11 Streamwise staggered increasing angle with $P^* = 6$. 86

D.12 Transverse staggered increasing angle with $P^* = 6$ 87

D.13: Streamwise staggered increasing Reynolds number with $\gamma = 7.5°$ and $P^* = 6$ 88

List of Tables

2.1 Summary of relevant criteria for studies reviewed; liquid working fluid, single 11

2.1 Summary of relevant criteria for studies reviewed; liquid working fluid, array 12

2.1 Summary of relevant criteria for studies reviewed; gaseous working fluid 13

4.1 Geometric parameters of plates for water-ethylene glycol tests 26

4.2 Geometric parameters of plates for staggered tests 27

4.3 Volumetric flow rates used in testing staggered arrays 28

4.4 Varying heights: water compared to WEG 32

4.5 Geometries and results for select papers. 39

B.1 Sample temperature data 57

B.2 Individual and average temperature values 59

B.3 Thermal conductivity of water-ethylene glycol chart 62

B.4 Calculated local surface values 63

B.5 Sample average surface value data, streamwise staggered, water 64

B.6 Estimated local surface values 64

D.1 Summary of experimental data 73

Nomenclature

Acronyms

IGBT	insulated-gate bipolar transistor
MOSFET	metal-oxide-semiconductor field-effect transistor
PID	proportional-integral-derivative
VFD	variable frequency drive
WEG	water-ethylene glycol

English Letter Symbols

A_n	flow area of a nozzle, m^2
D_h	hydraulic diameter, m

D_n	nozzle diameter, m
H	height of nozzles above surface, m
h	local heat transfer coefficient, W/(m^2 · K)
$\bar{h}$	mean heat transfer coefficient, W/(m^2 · K)
k	thermal conductivity, W/(m · K)
L_n	nozzle length, m
N	number of nozzles
Nu_{D_n}	local jet Nusselt number
$\overline{Nu}_{D_n}$	mean jet Nusselt number
P	pitch between nozzles, m
q''	heat flux, W/m^2
Re_{D_n}	jet Reynolds number
U_n	average nozzle velocity, m
$\dot{V}$	volumetric flow rate, L/s
x	horizontal distance in flow direction from center, m

y	horizontal distance perpendicular to flow direction from center jet, m
z	vertical distance above impingement surface, m

Greek Letter Symbols

γ	angle between plate and surface
ν	kinematic viscosity, m^2/s

Superscripts

*	nondimensionalized with respect to D_n

Subscripts

n	nozzle

Chapter 1

Introduction and Theory

1.1 Electronics Thermal Management Considerations

Modern electronics continue to increase in power output and decrease in size, causing a need for cooling strategies more efficient at heat removal and implemented in more proportionate sizes. Traditional air-cooling techniques are not capable of meeting the need, and more aggressive and innovative cooling techniques are being explored, many focusing on liquid cooling. In addition to the key factors of effectiveness and size, considerations must be made with respect to cost, practicality, and reliability.

As thermal management systems tend to serve in auxiliary capacities to enable the reliable use of electronics packages, the general cost and production volume expected for the core product must be considered. For the purposes of a special case or limited market design, the cost associated with the implementation of a given thermal management system is a more negotiable subject; however, these solutions are also needed to address consumer products that operate on a broader market, most notably in the automotive and consumer electronics industries. If a thermal management scheme adds a significant enough portion to the total product cost, then it is not an economic option for high volume production. When applying a revision to a portion of an existing product, the ability for the new strategy to interface with the existing system must be taken under consideration. Relative size, weight, and complexity not appropriately corresponding to the existing structure can severely inhibit the ability of a system to perform the intended function.

Although advanced liquid cooling techniques exist that can provide sufficient cooling on the desired size scale at the surface, the associated equipment for these schemes is often just as, or more, unwieldy as the original design. An example of integrated-gate bipolar transistors mounted on a liquid-cooled cold plate is shown in Figure 1.1.

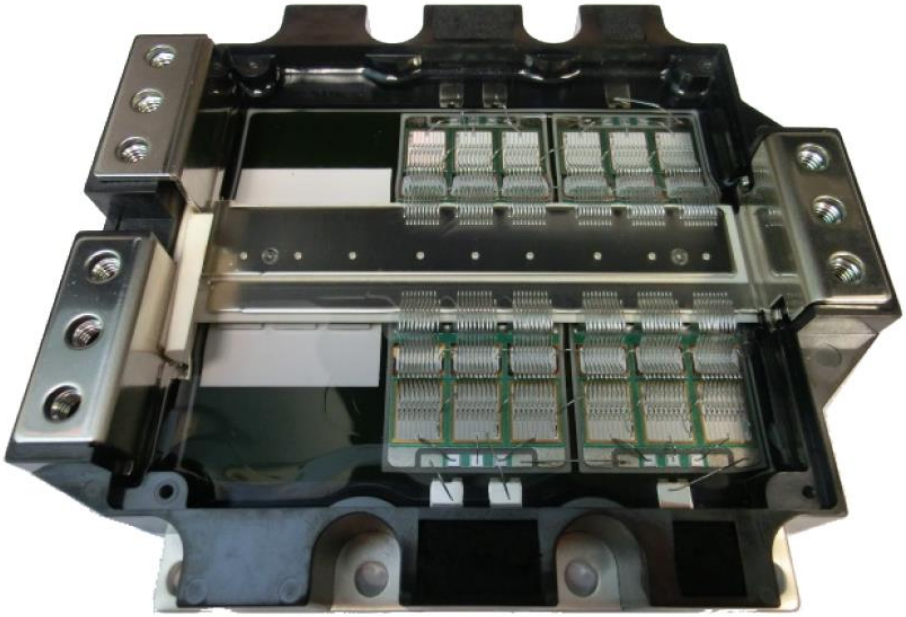

Figure 1.1: An IGBT module mounted on a liquid-cooled cold plate, using thermal grease as a thermal interface material.

When considering a thermal management scheme, the likelihood and magnitude of potential failures must be considered. The failure of a cooling scheme will almost certainly lead to a temperature rise in the target device, which can cause temporary inoperability or permanent damage as can be seen in Figure 1.2 In liquid cooling set-ups, some modes of failure can go as far as damaging components of entirely unrelated systems.

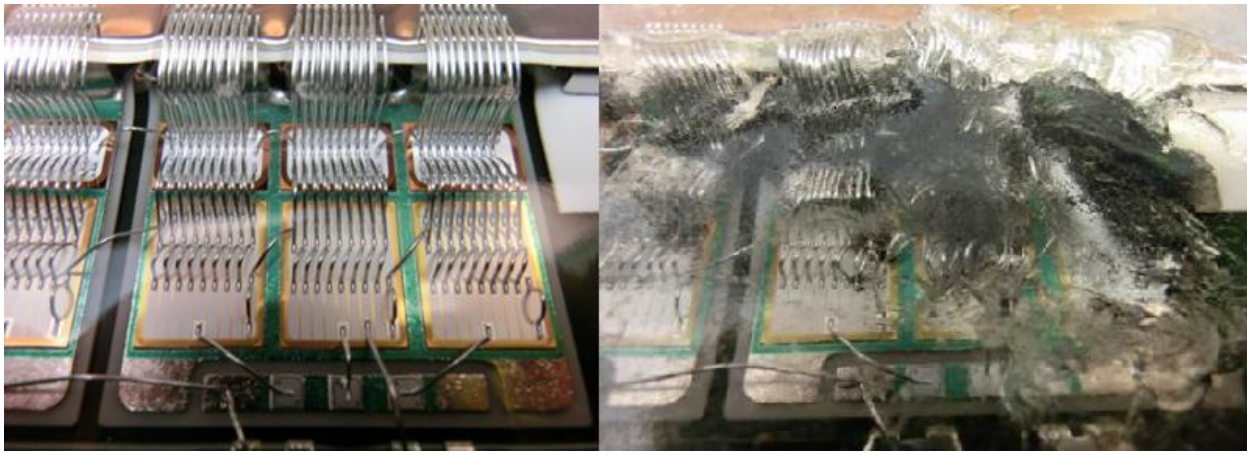

Figure 1.2: IGBT module before (left) and after (right) overheating during operation due to issues with containing the grease interface.

1.2 Applicability of Power Electronics Cooling Techniques in Automotives

Preferred forms of electronics cooling techniques include the employment of two-phase systems, microchannels, and jet impingement. Each of these is characterized by a solid surface rejecting heat into a fluid, and the fluid being removed after receiving excess heat. Two-phase cooling can achieve the highest values of heat transfer coefficient compared to the other techniques, but will typically requires operation in settings with a high degree of environmental control or high capacity cooling in the fluid loop. Microchannels are highly effective on small scales, but require high amounts of pumping power and are costly to manufacture, although additive manufacturing methods are poised to alleviate production costs. Jet impingement can be effective on larger scales than microchannels, but include an inherent non-uniformity to the cooling flow. This will be discussed more in the Chapter 2 literature review.

The electronics being used on board modern electric, hybrid-electric, and military vehicles are no exception to the need for enhanced cooling strategies. Due to the large amounts of heat produced under hood and the outdoor nature of the application, any system employed needs to be

operable on wide ranges of temperature and relative humidity, making two-phase cooling an unreliable choice [1-6]. Some success has been found in laboratory settings by Aranzabal [7], but using R-134a as the working fluid drives up the cost and is prohibited in certain countries, including the United States. The high cost of manufacturing microchannels would drive the product price well above the range that would be acceptable for potential buyers. Jet impingement is operable in a wide range of conditions, and relatively inexpensive to manufacture.

Furthermore, it would be preferable to make use of the resources already on hand within a vehicle, and both two-phase cooling and microchannels would require a significant amount of retrofitting to provide the infrastructure, i.e. condensers, pumps, etc., necessary to operate a flow loop incorporating either cooling plan. The working fluid already conveniently flowing through the existing flow loop is water-ethylene glycol (WEG), and is favored for its primary use for its unlikeliness to change phase. High viscosity fluids like WEG require greater pumping power to achieve the same flow characteristics as more typical electronics coolants, and place a higher emphasis on the weak point of microchannels. Jet impingement provides a cooling option that is compatible with the equipment and fluid on hand, is not as hindered by the viscous working fluid, and with an effective fluid management scheme the non-uniform cooling can be mitigated.

1.3 Jet Theory

Jets are streams of directed fluid, often forced through an aperture and directed at a solid surface either orthogonally (normal jets) or at an angle (oblique). If the aperture is through a thin, flat wall it is called an orifice and the jet exits with a relatively flat velocity profile and poor heat transfer characteristics. If the aperture is through a thicker wall, and turbulent flow is not induced, the exit velocity profile takes on the parabolic shape of pipe flow with good heat transfer properties

and without flow contraction. Depending on the media between the aperture and impinging surface and the manner of removing spent fluid, jets can be classified, either as submerged or free. The different types of jets, based on plate geometry, are demonstrated in Figure 1.3. Fluid flowing through submerged jets exit the orifice into a fluid of the same phase. Free jets exit into fluids of another phase, or potentially of the same phase but with contrasting densities to the point that mixing does not occur. Submerged jets are more suited to compact flow loops than free jets. Several well-regarded reviews have investigated the use of impinging jets in both heat and mass transfer applications [8]. An additional type of jet, not included in Figure 1.3, is a slot jet, which a jet in which the aperture through which flow is directed is significantly elongated along the plate.

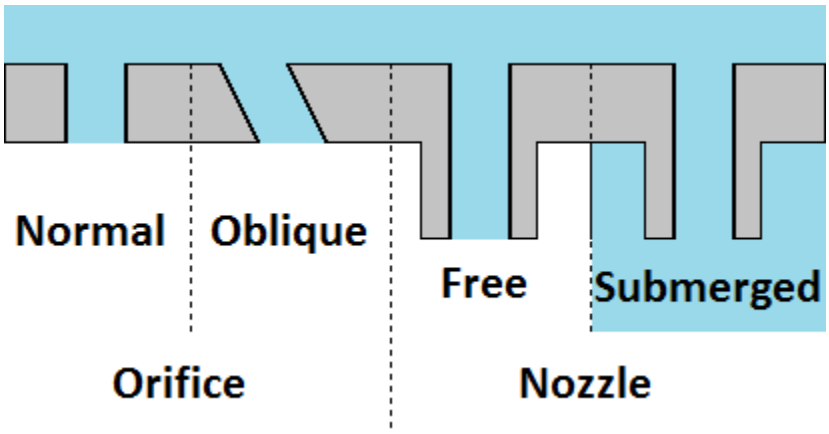

Figure 1.3: Comparison of different geometries for different jet definitions

1.3.1 Jet Regions

Exiting with low pressure and high velocity compared to the nozzle entrance, a submerged jet develops several characteristic flow regions, as shown below in Figure 1.4. Shear forces cause a boundary layer to form between the impinging fluid and the surrounding fluid. A widening effect increases the amount of surface area dynamically cooled at the heated surface, but the integrity of

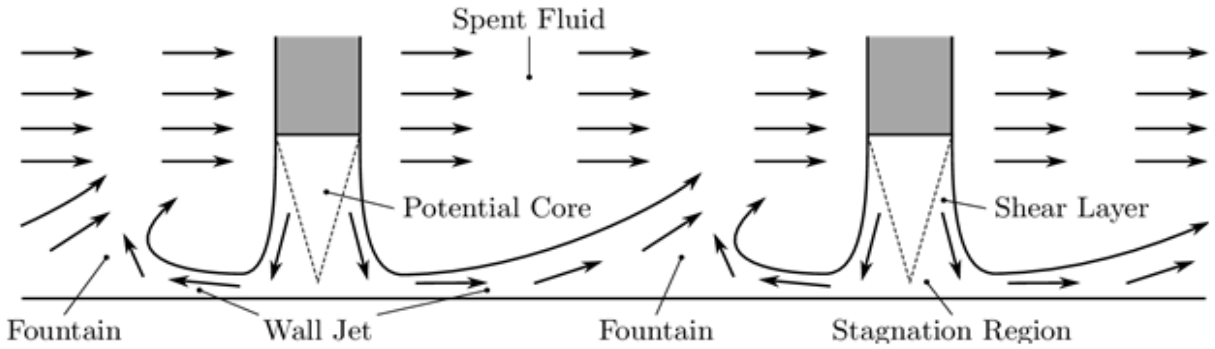

Figure 1.4: Flow and flow regions of neighboring normal, nozzle jets.

the jet diminishes as well. The simultaneous widening and weakening is marked by a conical region called the potential core in which axial velocity remains moderately unaffected by shear forces. If the nozzle outlets aren't sufficiently away from the heated surface ($\sim 2D$), the potential core may not form thereby reducing the amount of heat transfer dramatically. In the region directly in line with the nozzle outlet a stagnation point, or impingement zone, forms in which flow is forced to spread out along the walls, forming new boundary layer regions called wall jets. If an array of jets is used, locations in between the impinging jets experience upward flow called fountains, which break the boundary layers and convey heat from the surface into the spent fluid flow. If spent fluid from all the jets have the same location for outlet flow, care must be taken to ensure that the transitioning flow from the fountain regions doesn't negatively affect the neighboring jets [9, 10]. This is a multifaceted issue and much of the focus in [11-13] was on finding a correlation and optimizing it for height H above the wall, pitch P between the jets, and angle γ of the expanding area available for outflow in normal impinging jets with a single outlet. The highest regions of heat transfer in jet impingement are located at the stagnation points, with secondary maxima located in the fountain regions, where jet-to-jet interactions occur [14, 15].

Chapter 2

Literature Review

As discussed in Chapter 1, the 2016 annual report of the National Renewable Energy Laboratory's Gilbert Moreno [1] supports the idea that the growth of under-hood sensor and computer technologies considered standard in the automotive industry, in both commercial and military applications, has generated a need for a rugged system for cooling electronics modules that produce high amounts of heat. Air-cooling is unlikely to be able to provide an adequate amount of cooling, therefore liquid-cooling options are typically considered and often employ water as the working fluid. General information about the works reviewed is tabulated at the end of the chapter.

Jet impingement cooling is more suitable to automotive applications than two-phase cooling and microchannels due to its low pressure drop and high volumetric flow rate, as well as the wide range of ambient operating conditions that could be expected [2-6]. The primary drawback with jet impingement arrays is the degradation of downstream jets by the exiting flow of the upstream jets [9, 10] as flow from fountain regions are drawn toward an outlet. Consequently, when using an array of jets, strategies for spent fluid management are often considered. This thesis directly expands on one of these in the work of Maddox [11-13] which involves the experimental and numerical investigation of an angled outlet manifold.

There are research groups exploring jet impingement that are not looking explicitly at spent fluid management [4, 5, 8, 14-26], because the application or interest of their study only calls for

a single jet [4, 5, 14, 16, 18, 20, 21,24], a simple line of jets [17, 19], or otherwise had a reason not to employ one, such as inlet flow management through variable sized orifices or induced turbulence [22, 23] or a unique focus on observing interactions with thermochromatic liquid crystals [14], shown in Figure 2.1. Select examples of studies employing single jets without a focus on spent fluid management scheme include Whelan and Robinson [4] who tested varying nozzle inlet and outlet geometries and Kashi and Haustein [20] who focused on effects of nozzle length. Turbulence effects and higher velocities, if they can be achieved so they occur at the surface without degrading the potential core of incoming jets, are preferable for the heightened heat transfer they induce. The prevailing issue in studies on turbulent jets is the high difficulty of conducting accurate analysis and modelling of flow and, in turn, heat transfer effects. As a result, the studies into these schemes almost always require an empirical aspect.

Studies that do investigate spent fluid management can be broken into two categories; strategies that add features to the impinged surface [24-27] or changing the geometry of the outlet

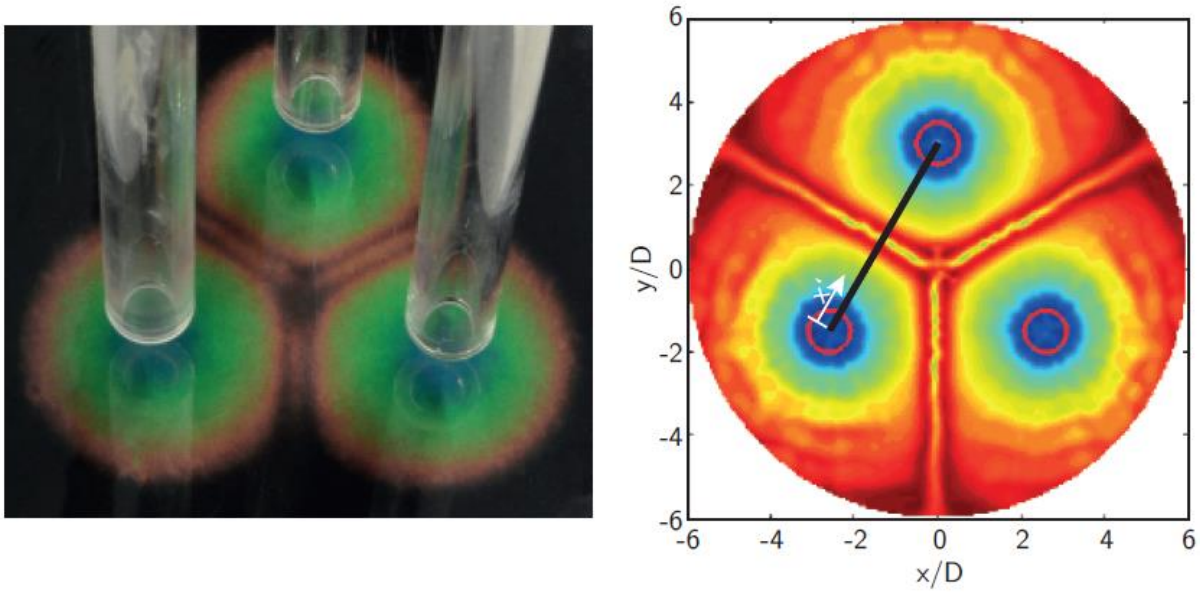

Figure 2.1: Rholfs, et. al. [14] images demonstrating the experimental use of and digital rendering of heat transfer in thermochromatic liquid crystals.

manifold [6, 9, 10, 28-30]. The former of these tend to typically take the form of microchannels that in addition to guiding outlet flow provided extra surface area for heat transfer, and the latter strategies tend to provide multiple exits for outflow. Despite microchannels being a fairly common structure to find added to a surface, they are often only employed, as microfins, as a means of increasing the area available for heat transfer rather than for spent fluid management. One favored form of outlet geometry design is to stagger inlet nozzles and outlet ducts to varying degrees [6, 9, 10]; while effective, this tends to lead complex and often unwieldy geometries, such as with the study conducted by Brunschwiler et. al. [9] in Figure 2.2.

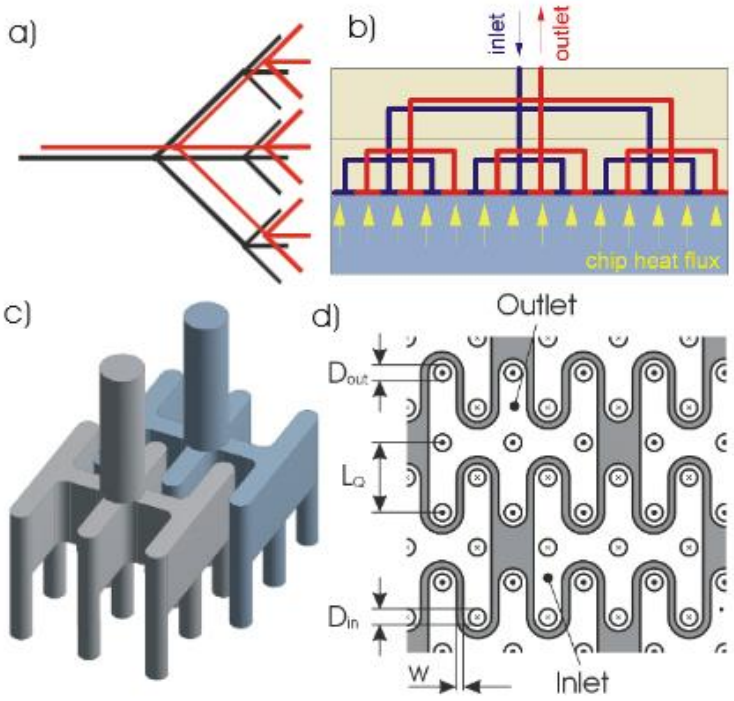

Figure 2.2 : Brunschwiler et. al. [9] graphic to demonstrate a complex, nested flow branches for delivering to and removing from fluid to their heated.

A study conducted by Michna, et. al. [31] is particularly worthy of note in the context of this thesis, as it compares in-line and staggered arrays for micro-cooling applications using the ratio of nozzle area to heated surface. The in-line array with the largest area ratio had the best heat transfer results of all geometries, and the in-line array with the smallest value had the worst values

of all geometries. Of the three staggered arrays, the median value of area ratio performed better than the other two. Michna group noted this was probably due to negative crossflow effects as there is no spent fluid management concept applied. It should also be considered that the jet-to-jet spacing on the staggered array is so low that there is not enough space for fountain effects to properly form. Average Nusselt numbers for water were between 5 and 80 for Reynolds numbers between 50 and 3500.

The influence of reviewed literature on the water-ethylene glycol testing section of this study is limited; however the work by Narumanchi et. al.[5] provides a few reference points for validating certain parameters such as selected flow rates and jet-to-surface heights. Several of the papers reviewed can be considered influential or supporting in some of the design choices made for the staggered portion of testing. Arens et. al. used varying nozzle diameter at array edges, as shown in Figure 2.3 and corroborated the benefits of using an angled manifold,

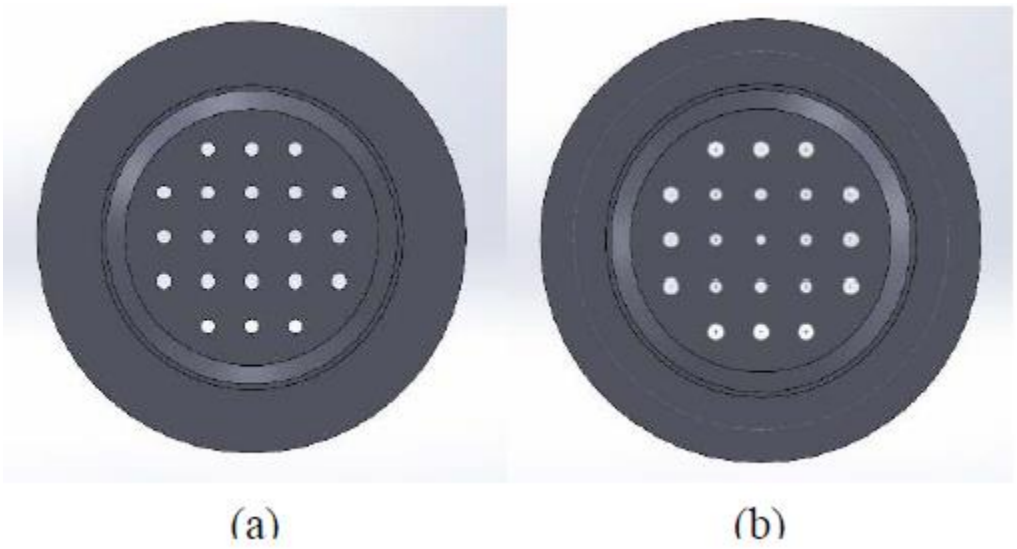

Figure 2.3: Arens et. al. [22] test arrays with (a) constant diameter and (b) decreasing diameter toward the center of the array.

Table 2.1 on the next few pages lists some key details of many of the papers reviewed, many employing interesting geometries, some with interesting working fluids, and a few with a valuable qualitative result. Quantities reported were as presented as results in the paper, or were pulled as ranges and maximum values from charts. Some unit conversions were made for consistency. Varying geometries and scales, as well as the form results are presented make it difficult to unify qualitative results into one type of value (e.g. heat transfer coefficient).

Table 2.1: Summary of relevant criteria from studies reviewed; liquid working fluid, single

Principal Author	Type of Jet(s)	Application/ Working Fluid	Characteristic Heat Transfer Quantity Reported	Extra Notes
Moreno	Free and submerged; single jet	General study[1]/Water	Thermal resistance < 0.2 K/W	Combined with surface features
Whelan	Submerged; single jet	General study/ water	257 kW/m^2	Inlet/outlet geometry studies
Moreno (Narumanchi)	Free and submerged; single jets	Automotive power electronics/ water	Nu ≈ 500 -2500	Combined with microstructures; direct cooling of IGBTs
Narumanchi	Submerged; single jet	Automotive power electronics/ WEG	125 kW/m^{2}K	Combined with microfins on surface
Jorg	Submerged; single jet	Semiconductors/ water	6-12 kW/m^2	Direct cooling of MOSFETs
Sui	Embedded; single jet	Electric vehicles and power trains/ water	Thermal resistance < 0.1 K/W	Direct cooling of MOSFETs/combined with microchannel
Kashi	Submerged; single jet	General study/ water	Nu ≈ 120	Numerical comparison to others' experimental studies; nozzle length

[1]General study is applied to any study that doesn't specify a technology more specific than electronics cooling

Table 2.2: Summary of relevant criteria from studies reviewed; liquid working fluid, array

Principal Author	Type of Jet(s)	Application/ Working Fluid	Characteristic Heat Transfer Quantity Reported	Extra Notes
Lee	Submerged; single, inline and staggered arrays	Comparison/ water	5000 kW/m^2	Jet impingement is comparable or better for square areas of side length 0.07 m or greater
Robinson	Submerged; inline arrays	Comparison/ water	120 kW/m^{2}K	Jet impingement require a lower pressure drop and higher volumetric flow rate
Rattner	Submerged; array of round jets	General study/water	82.3 kW/m^{2}K	Spent flow management, simulation only, microchannel comparison
Aranzabal	Two-phase, submerged array	Electric vehicles/ R-134a	10-12 kW/m^2	Primarily simulation with limited experimental results
Brunschwiler	Submerged; inline array	General study/ water	87 kW/m^{2}K	Spent fluid management; inline outlets staggered with inlets, somewhat complicated outlet channel tessellation
Han	Submerged; array of round jets	Microcoolers/ water	260 W/cm^2	Combined with microchannels; spent flow management
Ditri	Submerged (embedded cooling); array	High power amplifiers/ propylene-glycol water	50 kW/m^{2}K	Microfluidic cooling, combined with microstructures; simulation only
Michna	Submerged microjets; inline and staggered array	General study/ water and air	11 kW/ m^{2}K	Microscale cooling
Karwa	Submerged; array of round jets	Thermoelectric refrigerators/ water	0.025 K/W	Spent flow management
Arens	Sumerged; array of variable size jets	General study/ water	39 kW/m^{2}K	Study had best results with increasing orifice diameter towards edge of circular jet plate

Table 2.3: Summary of relevant criteria from studies reviewed; gaseous working fluid

Principal Author	Type of Jet(s)	Application/ Working Fluid	Characteristic Heat Transfer Quantity Reported	Extra Notes
Onstad	Submerged; staggered array	Cooling of gas turbine blades/ air	Nu ≈ 20-100	Spent fluid management; 6 outlet ports adjacent to each inlet jet
Rohlfs	Submerged; three round jet array	General study/ unspecified gas	General expressions	Employed thermochromatic liquid crystals
Selvaraj	Submerged; slot, line of round jets	Cooling of irradiated materials/air	2.5 kW/m^{2}K	Helium is intended as the working fluid in future works
Leena	Submerged; line of jets	General study/ air	Nu ≈ 6.5	Numerical and experimental; varying heights
Ianiro	Submerged; single and multichannel jets	General study/ air	Nu ≈ 200	Multichannel outlets designed to have a tangential flow
Obot/ Trabold	Submerged; array of jets	General study/ air	Nu ≈ 5-90	Two-part study of controlled crossflow through available outflow directions with varying surface roughness
Yeranee	Inline array of jets	General study/ air	Nu ≈ 120	Numerical and experimental; induced turbulence through entrainment in nozzles

Chapter 3

Experimental Setup and Procedures

3.1 Jet Plates

In order to best observe jet-to-jet interactions, test plates were designed with a central jet and a basic array of neighboring jets; therefore, testing was conducted using 3 x 3 inline arrays and two orientations of 7-nozzled staggered arrays, shown in Figure 3.1. The geometric layouts were described in a Cartesian coordinate system with the origin located on the impinged surface, directly below the central jet with the x-direction along the surface in the downstream direction and the z-direction perpendicular to the surface.

The characteristic length was defined as the diameter of the nozzle exit, D_n. Other significant geometric parameters of the jet plates, shown in Figure 3.2 were nondimensionalized by dividing by the characteristic dimension: P^+ = P/D_n, $L_n^+ = L_n/D_n$, and $H^+ = H/D_n$.

For testing with water-ethylene glycol (WEG) the confining walls were constructed from acrylic, 5.715 mm (0.225") thick. Plates were installed with nozzles of acrylic tubing with outside diameter 6.35 mm (1/4"), and inside diameter 3.175 mm (1/8"), the smallest readily available at the time of fabrication.

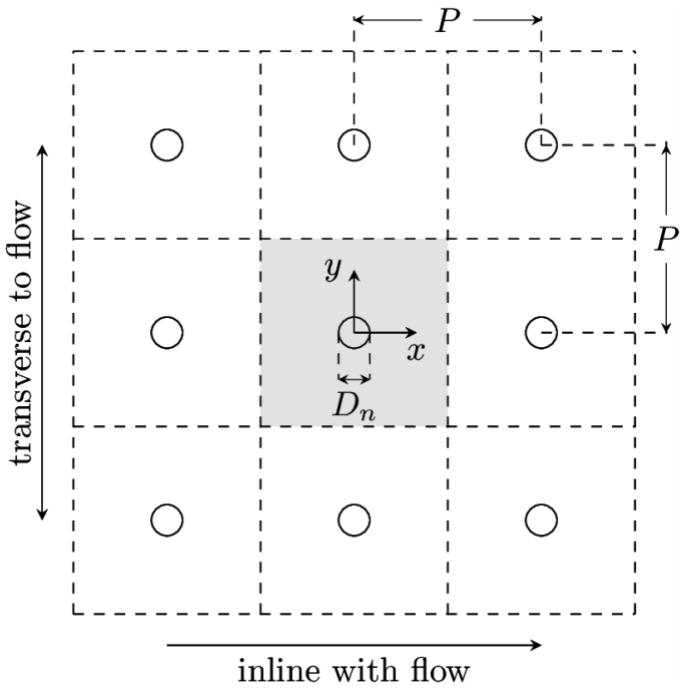

Figure 3.1 (a): Spatial arrangement of inline jet array

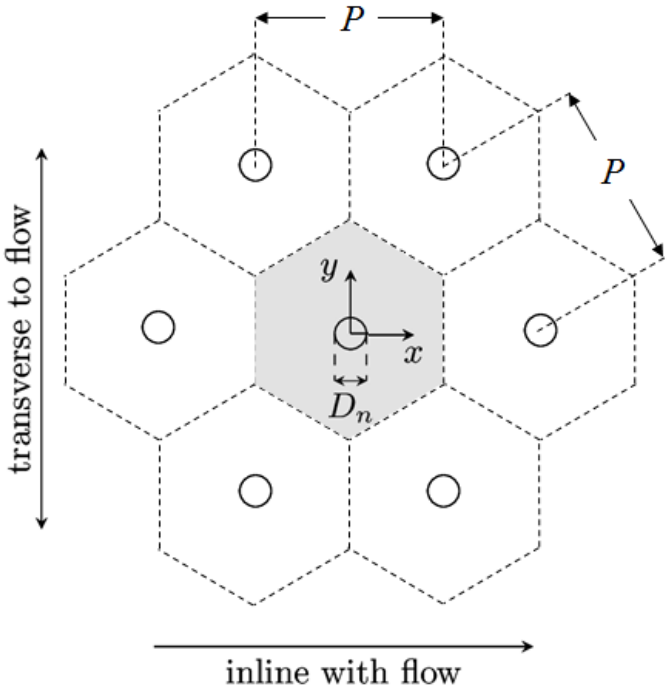

Figure 3.1 (b) Streamwise Staggerd

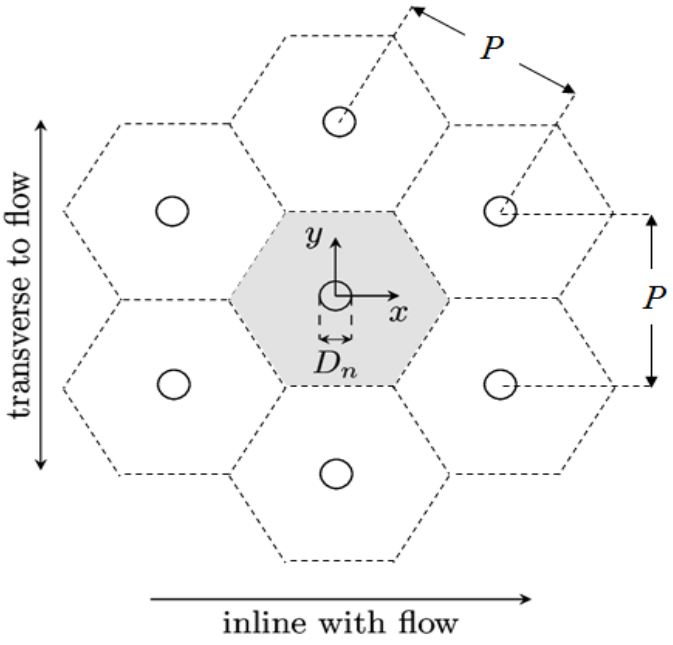

Figure 3.1 (c): Transverse Staggered

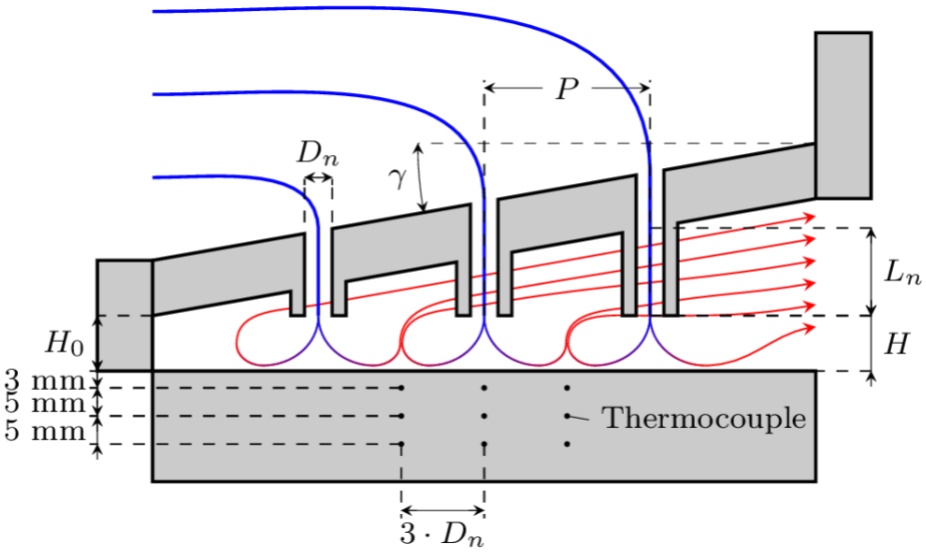

Figure 3.2: Side cross-section of jet plate

Plates measure approximately 7.62 cm (3”) by 7.62 cm (3”) , and .635 cm (1/4”) gaskets are epoxied to each edge to prevent flow between the jet plate and the adjusting walls. For testing with water, plates were fabricated using polymer deposition 3D printing on Cubicon Single printers, modelled in AutoCad. The material used in producing the plates was ABS plastic, and the dimensions were kept the same. Figure 3.3 shows a pair of the printed plates for reference. After printing, plates were treated top-down with acetone vapor for a smoother surface finish.

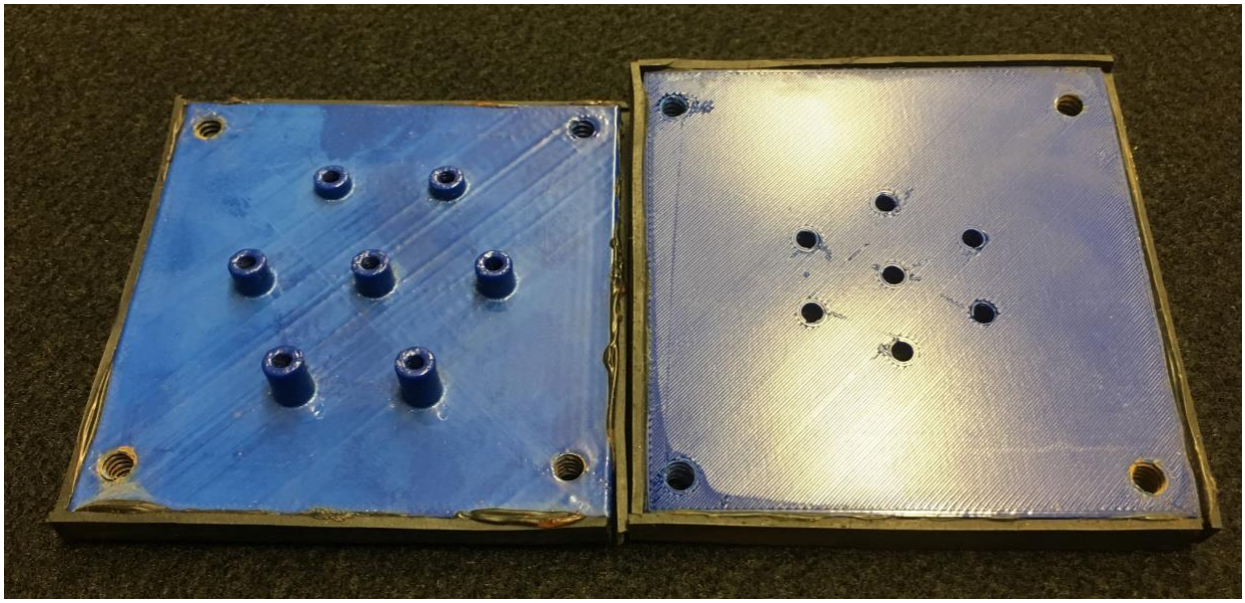

Figure 3.3: Underside (left) and topside (right) of printed jet plates.

3.2 Flow Chamber and Heat Generation

The flow chamber, shown in Figure 3.4, is compatible with inline arrays with pitch $P^+ \leq 8$ and a jet height of $H^+ \leq 6$. At larger pitches, jet-to-jet interactions have minimal effects [8]. With spent fluid management, the optimized height is expected to be less than two jet diameters above the surface. The manifold outlet is capable of accommodating angles up to $\gamma = 45°$.

The flow chamber consists of an exterior and interior chamber, the latter of which is movable to allow jet plates to be translated along the surface along the flow, in the x-direction, as well as transversely to the flow, in the y-direction. Rubber gaskets were used to keep the working fluid from flowing over or around the inner chamber, and inner plenum walls direct the fluid through the jet plate. Set screws were used to position the inner chamber walls to translate them to the desired positions, and to adjust the height of the jet plate above the surface.

The base of the chamber was manufactured out of thermally resilient garolite, mounted with a pair of copper blocks, shown in Figure 3.5. The upper block was used as the impingement surface as well as for thermal measurements. The lower block, measuring 10.16 cm × 10.16 cm × 7.63 cm (4" × 4" × 3"), was implanted with eight 1.27 cm × 10.16 cm (1/2" × 4") cylindrical cartridge heaters, which were wired in parallel and powered by a direct current (DC) power supply. The power supplied during testing was 500 W, and the blocks were connected by a layer of Sil-Pad 800 and surrounded by foam insulation to reduce heat losses.

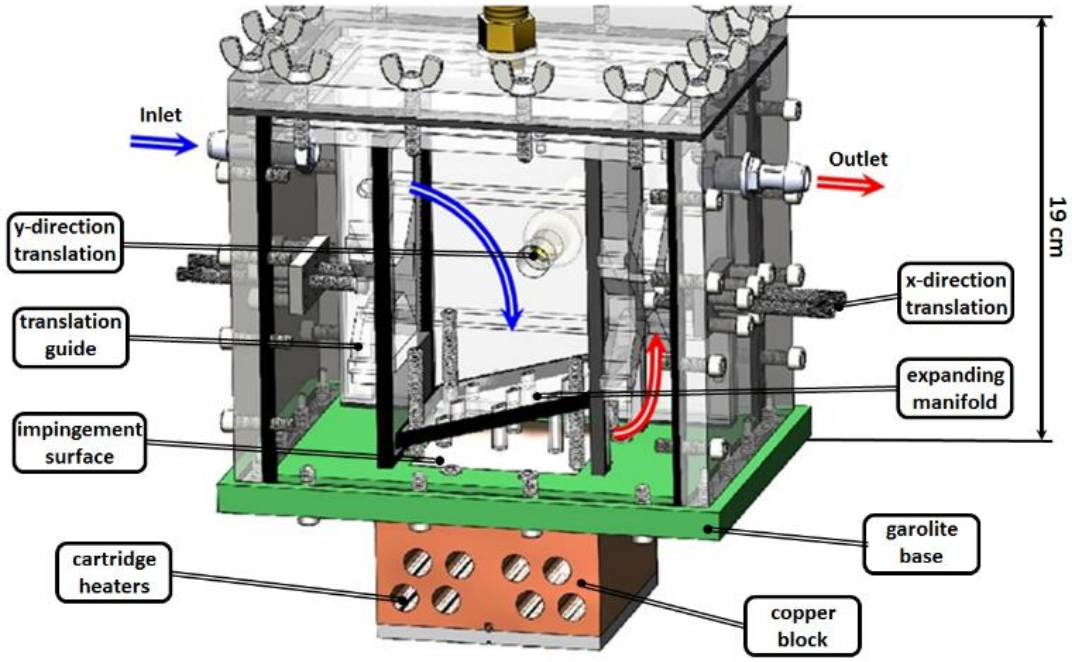

Figure 3.4: Cross-section of jet impingement chamber.

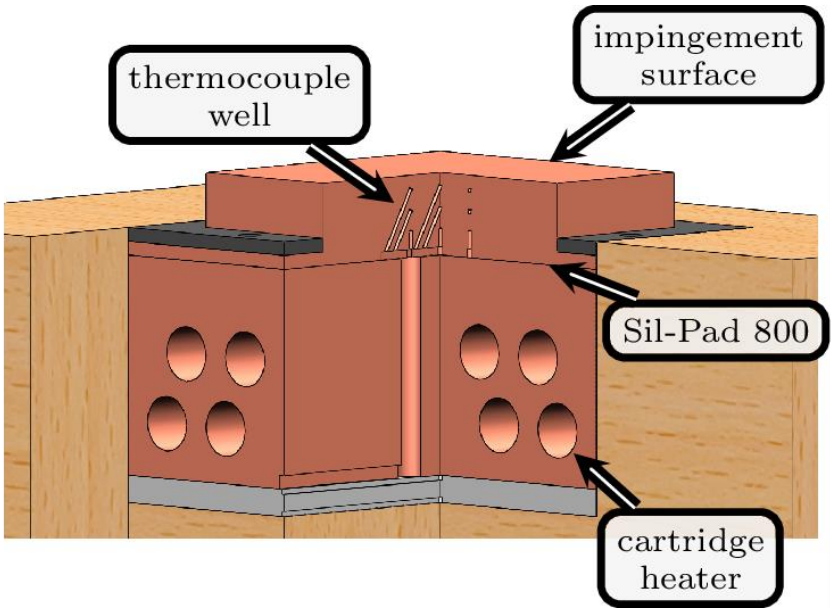

Figure 3.5: Cross-section of copper blocks

3.3 Flow Loop

The flow loop shown in Figure 3.6 illustrates the path of a single-phase working fluid, either deionized water or a volumetrically balanced mixture of 50% water and 50% ethylene glycol. Flow was driven by an Iwaki magnetic pump with a three-phase induction motor, which was modulated by a Lenze SMVector variable frequency drive (VFD). The set point of the VFD was directed by a software proportional-integral-derivative (PID) controller. An Omega FTB4700 turbine flow meter monitored the volumetric flow rate, and an Arduino Uno read in the flowmeter data and delivered it to the PID program. The temperature of inlet and outlet flows of the impingement chamber, as well as an ambient temperature were measured using k-type thermocouples. A NESLAB RTE-220 chiller was used

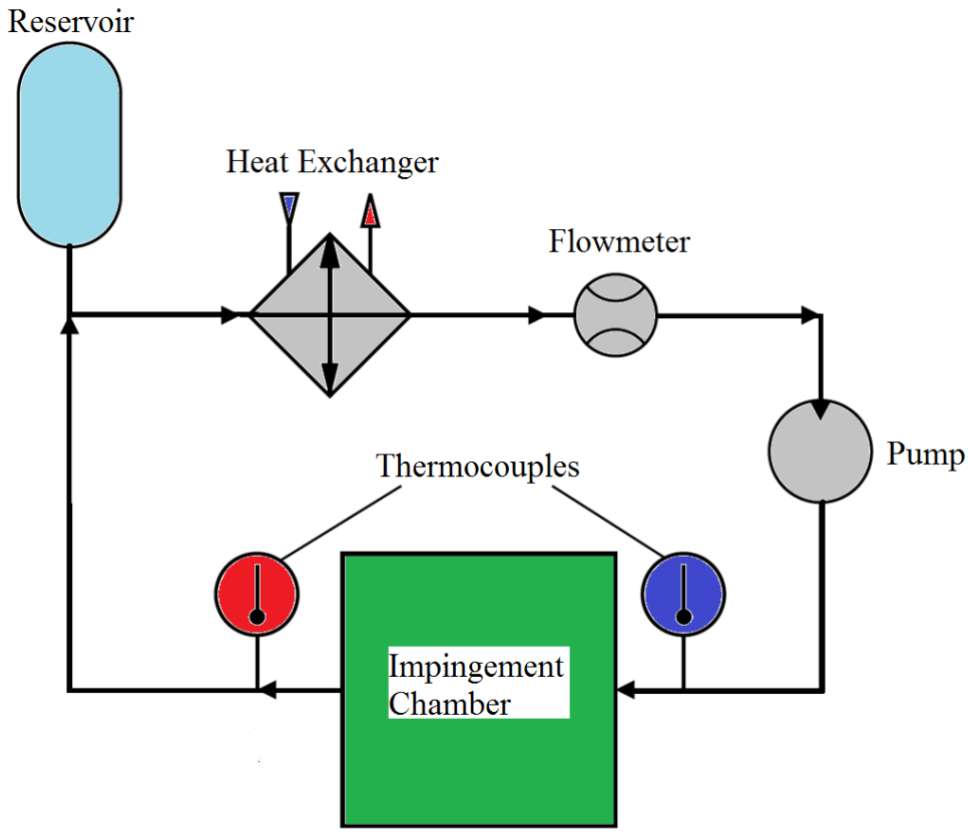

Figure 3.6: Flow loop diagram

to supply chilled water to a heat exchanger, keeping the inlet fluid temperature at approximately 30℃. A jet Reynolds number, representing the equivalent Reynolds number in a given nozzle, using the total volumetric flow rate was used to categorize the tests.

$$Re_D = \frac{U_n D_n}{\nu}. \tag{3.1}$$

Where U_n is the mean inlet nozzle velocity, ν is the kinematic viscosity, and D_n is the hydraulic diameter of a single nozzle. The nozzle velocities are expected to be non-uniform, with

downstream nozzles exhibiting higher flow rates as predicted by Maddox's computational fluid dynamics (CFD) study [13]. A photograph of the experiment is provided below in Figure 3.7.

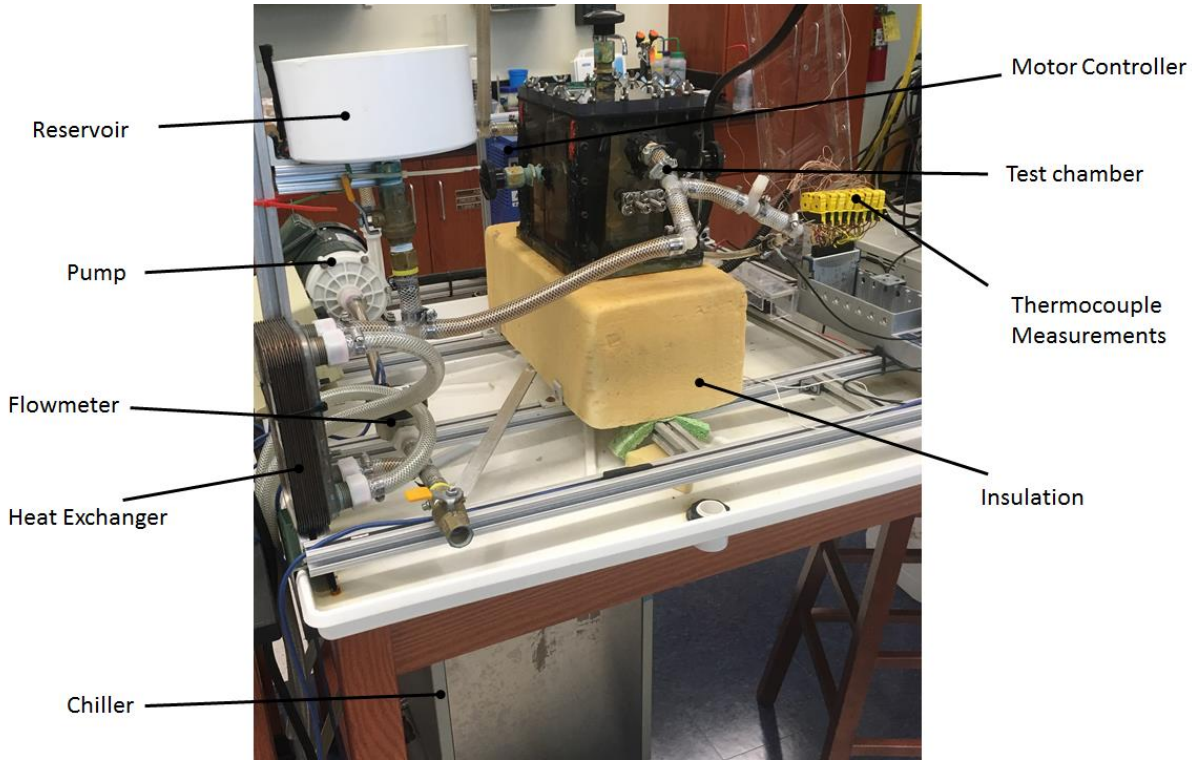

Figure 3.7: Photograph of experimental setup

3.4 Local and Average Surface Measurements

Twelve k-type thermocouples were embedded in the measurement block, in four groups of three at locations of 3 mm, 8 mm, 13 mm from the surface, as shown in Figure 3.2 and visible in Figure 3.5. The thermocouple wires were adhered within 1 mm wells drilled in the measurement blocks by a thermally conductive silver paste. The surface temperature, $T_{surface}$, of the measurement block was extrapolated by applying a linear fit to the twelve embedded

thermocouple groups., and combined with the inlet fluid temperature, $T_{inlet} \approx 30℃$, to calculate the temperature rise at the surface,

$$\Theta = T_{surface} - T_{inlet}. \tag{3.2}$$

The measurement block was used as a heat flux meter by using the gradient measured by the thermocouples and the known thermal conductivity of copper to determine the local surface heat fluxes directly above the thermocouple groups,

$$\dot{q}'' = -k \frac{\partial T}{\partial z}\Big|_{z=0}. \tag{3.3}$$

By combining equations (3.2) and (3.3), the local heat transfer coefficient above each thermocouple group was then estimated,

$$h = \frac{\dot{q}''}{\Theta}. \tag{3.4}$$

These values were in turn used, along with the nozzle diameter and known thermal properties of water and WEG at a mean fluid temperature, to calculate the local Nusselt number,

$$Nu_{D_h} = \frac{hD_h}{k_{fluid}}. \tag{3.6}$$

The focus area on the impinged surface for this study is the region around a singular central jet. In order to fully characterize this region one thermocouple group was located directly underneath the jet, one group was located three nozzle diameters upstream, one group was located three nozzle diameters downstream, and only one group located three nozzle diameters in a transverse direction as reasonable symmetry is assumed about $y = 0$. By translating the jet plate one diameter at a time across the surface in both the inline, x^*, and transverse, y^*, a regular grid of data points can be formed in relation to the jet positions. A diagram of the data points clustered

around the thermocouple groups that monitor them is provided in Figure 3.7. It is important to note that the measurement locations are inversely related to the direction the plate translation, i.e. when the jet plate has been translated one diameter downstream, the measurements are taken one diameter upstream of the nozzles.

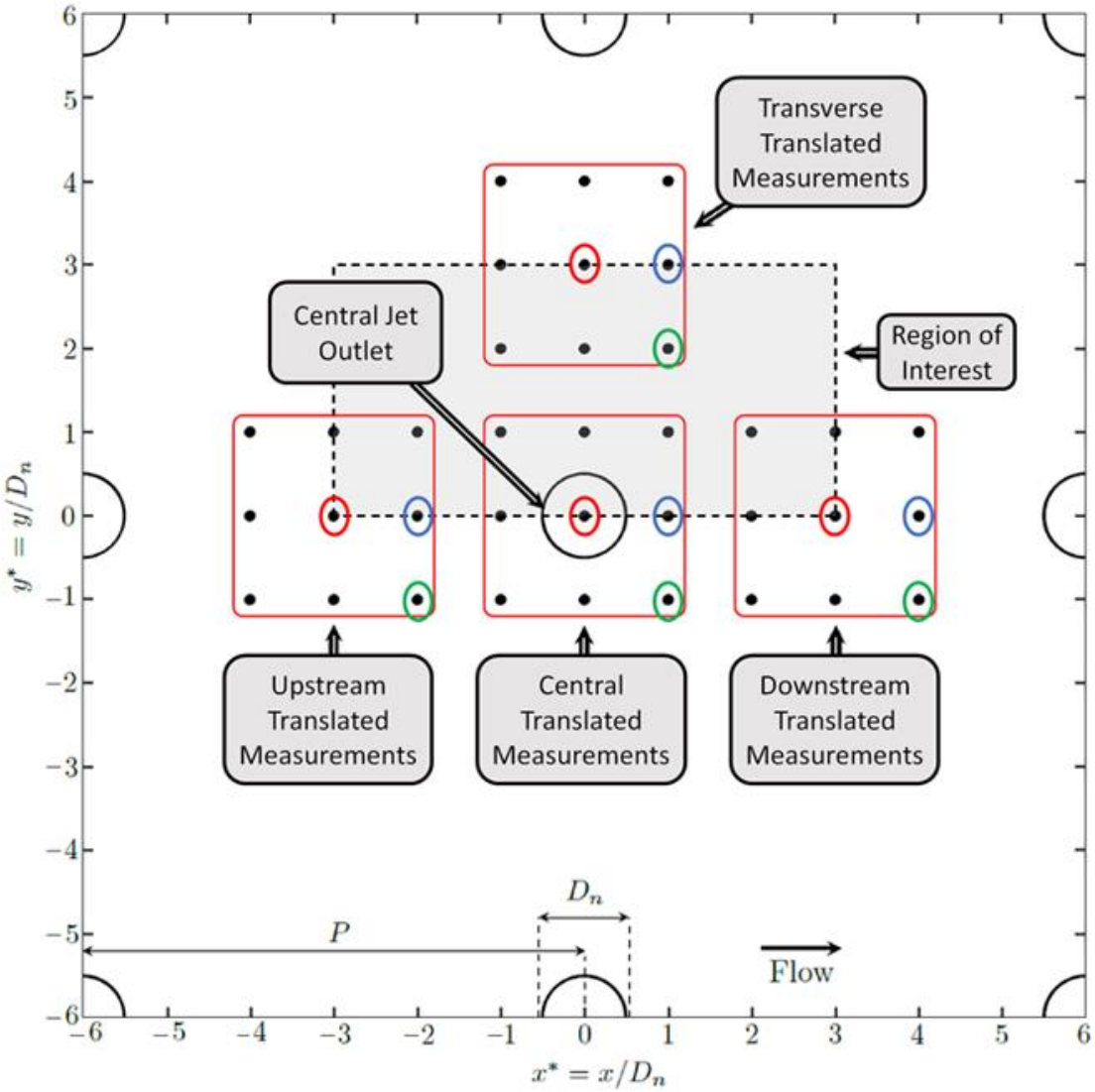

Figure 3.8: Surface measurement locations

Finally, mean values of the heat transfer coefficient and Nusselt number were found by integrating over the area of interest shown in Figure 3.7, half the area of the central jet in an inline array with a pitch of $P^+ = 6$,

$$\overline{Nu}_{D_n} = \frac{2}{(P^+)^2}\int_{-P^+/2}^{P^+/2}\int_0^{P^+/2}\frac{hD_h}{k_{WEG}}dy^+dx^+. \quad (3.7)$$

A set of sample calculations for the preceding equations are provided in Appendix B. The experimental uncertainties for the local and average surface measurements were determined through the method of sequential perturbations to be: $\pm 1.2\%$ for Θ, $\pm 7.7\%$ for $\dot{q}''$, $\pm 8.8\%$ for h, $\pm 2.5\%$ for $\bar{h}$ when $P^+ = 4$, and $\pm 2\%$ for $\bar{h}$ when $P^+ = 6$. The details of the uncertainty calculations are available in Appendix C. Hardware is initiated by a custom user interface generated for the project, and temperature data read in by a National Instruments data acquisition card is processed along with recorded flow rate data to determine steady state values. The temperature data is also processed and plotted using custom Python codes in a Linux environment.

When acquiring data, each test plate was translated to 9 locations giving the 4 data collection locations a total of 36 points along the surface with the groupings shown above in Figure 3.7. Suppose the first test location is acquired such that the center thermocouple cluster is located directly under the center nozzle; the red ovals represent the locations of the embedded thermocouple groups. After data is collected the test section would be translated 1 D_n in the $-x^*$ direction to the next test location, the thermocouples indicated by blue ovals now represent the locations of the thermocouple groups relative to the central jet outlet. After data collection, suppose the plate is moved 1 D_n in the $+y^*$ direction, the thermocouples are now located at the ovals green ovals. The testing would then carry on in this fashion until a 3 x 3 cluster of locations have been completed.

Chapter 4

Results

4.1 Overview of Parameters Tested

Previous studies with this experimental setup [11-13] focused on proving that using an expanding manifold had an alleviating effect on entrainment of downstream jets into spent flow and developing a general correlation for inline arrays with water as the working fluid. The current experimental study focuses on two major subsequent considerations to be made, and the series of tests can largely be grouped into two categories.

4.1.1 Water-Ethylene Glycol Tests

Due to the primary target application being the cooling of power electronics in electric vehicles by employing the existing radiator flow loop, the validity of the expanding area manifold must be justified with the working fluid of said flow loop, antifreeze or 1:1 volumetric mixture of water-ethylene glycol, which generally has Prandtl numbers 4-5 times those of water [32]. Tests were conducted with varying flow rate, manifold angle, and nozzle-to-surface height. Previously acquired tests with water were used as a reference point. Table 4.1 outlines the geometry characteristics of the plates used in water-ethylene glycol tests.

Table 4.1 Geometric parameters of plates for water-ethylene glycol tests

Pattern	Angle, γ	Pitch, P^*	Height above surface, H^*	Reynolds Numbers
Inline	0	6	1	5100
Inline	5	6	1	2050, 3000, 4050, 5100
Inline	5	6	2	5100
Inline	10	6	1	5100

4.1.2 Staggered Array Tests

Staggered jet arrays are popular and effective in jet-impingement applications as they allow for a greater number of jet-to-jet interactions per jet and provide a more even covering of fountain regions on the surface. Figure 4.1 shows an inline array and two orientations of staggered arrays that were tested, one with a jet located directly upstream of the center jet and measurement area, the other without.

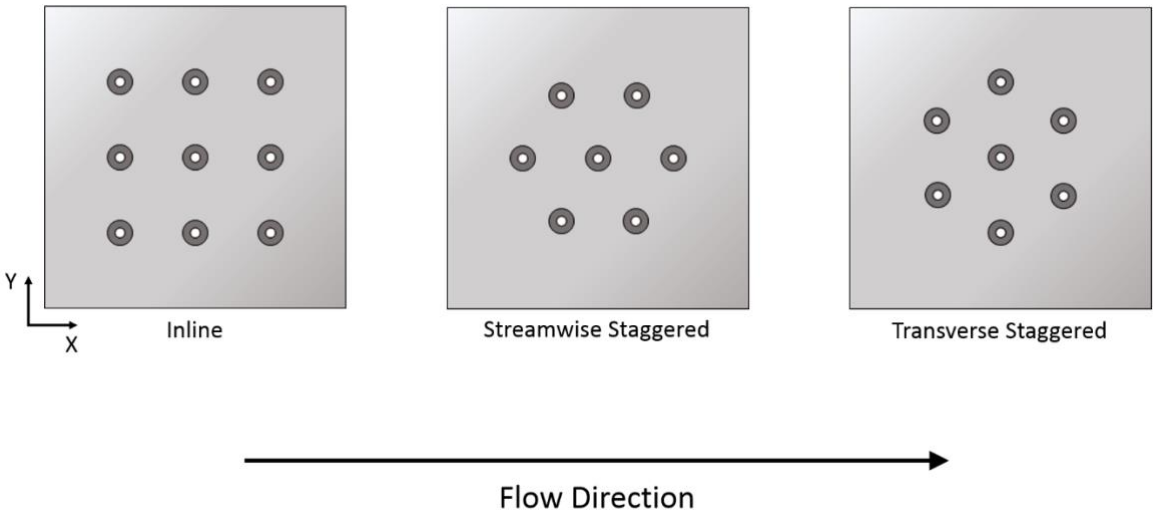

Figure 4.1: Varying patterns for staggered array

In order to introduce a smaller step size between angle values $\gamma = 2.5°$ and $7.5°$ were used instead of $0°$ and $10°$. Varying pitches and flow rates were also examined in the context of

staggered arrays. Table 4.2 outlines the geometric characteristics of the plates used in staggered array tests. Water was selected as the working fluid for the staggered array tests as it is the simpler working fluid to employ.

Table 4.2 Geometric parameters of plates for staggered tests

Pattern	Angle, γ	Pitch, P^*	Reynolds Numbers
Streamwise staggered	5	3	8400, 11200, 14000
Streamwise staggered	2.5	4	5600, 8400, 11200, 14000
Streamwise staggered	5	4	5600, 8400, 11200, 14000
Streamwise staggered	7.5	4	5600, 8400, 11200, 14000
Streamwise staggered	2.5	6	5600, 8400, 11200, 14000
Streamwise staggered	5	6	5600, 8400, 11200, 14000
Streamwise staggered	7.5	6	5600, 8400, 11200, 14000
Transverse staggered	2.5	6	5600, 8400, 11200, 14000
Transverse staggered	5	6	5600, 8400, 11200, 14000
Transverse staggered	7.5	6	5600, 8400, 11200, 14000

In order to be more comparable to earlier work with water [11-13], it was decided that tests should be conducted at the same Reynolds numbers as before. Additionally, nozzle diameter was held constant, meaning the average nozzle velocity, or rather Arduino controlled volumetric flow rates, ~~V,~~ would need to be adjusted.

Using Equation 3.1,

$$Re_D = \frac{U_n D_n}{\nu}, \tag{5.1}$$

and defining volumetric flow as,

$$\forall \approx N A_n U_n \tag{5.2}$$

where N is the number of nozzles and A_n is the area of a single nozzle. The new set values were obtained by the proportion,

$$Re_{D,stag} = \frac{\frac{\forall_{stag}}{N_{stag} A_n} D_n}{\nu} = \frac{\frac{\forall_{inline}}{N_{inline} A_n} D_n}{\nu} = Re_{D,inline} \tag{5.3}$$

Reduced to

$$\begin{gathered} \frac{\forall_{stag}}{N_{stag} A_n} = \frac{\forall_{inline}}{N_{inline} A_n} \\ \forall_{stag} = \frac{N_{stag} \forall_{inline}}{N_{inline}} = \frac{7}{9} \forall_{inline} \end{gathered} \tag{5.4}$$

The Reynolds numbers used in water testing are presented in Table 4.3 below with the corresponding 2.333s for both inline and staggered patterns.

Table 4.3 Volumetric flow rates used in inline and staggered arrays

Re_D	Inline Flow Rates L/s (gpm)	Staggered Flow Rates L/s (gpm)
5600	.1262 (2)	.0982 (1.556)
8400	.1893 (3)	.1472 (2.333)
11200	.2524 (4)	.1963 (3.111)
14000	.3155 (5)	.2454 (3.889)

4.2 Water-Ethylene Glycol Results and Discussion

A complete set of results is provided in Appendix D. The most significant results are presented in the following paragraphs to highlight the effects of varying Reynolds number, manifold angle, and jet-to-surface spacing with water-ethylene glycol flowing through inline arrays.

Surface maps in Figure 4.2 show that for an angled nozzle plate with $\gamma = 5$, $P^* = 6$, and $H^* = 1$, local heat transfer coefficients increase from 2.5 to 3.24 kW/m^2K as WEG flow rates increase from $Re = 2050$ (a) through 3000 (b) and 4050 (c) to 5100 (d). Because $Nu = f(Re)$, it is expected that larger Reynolds numbers will result in greater heat transfer, and this is the case

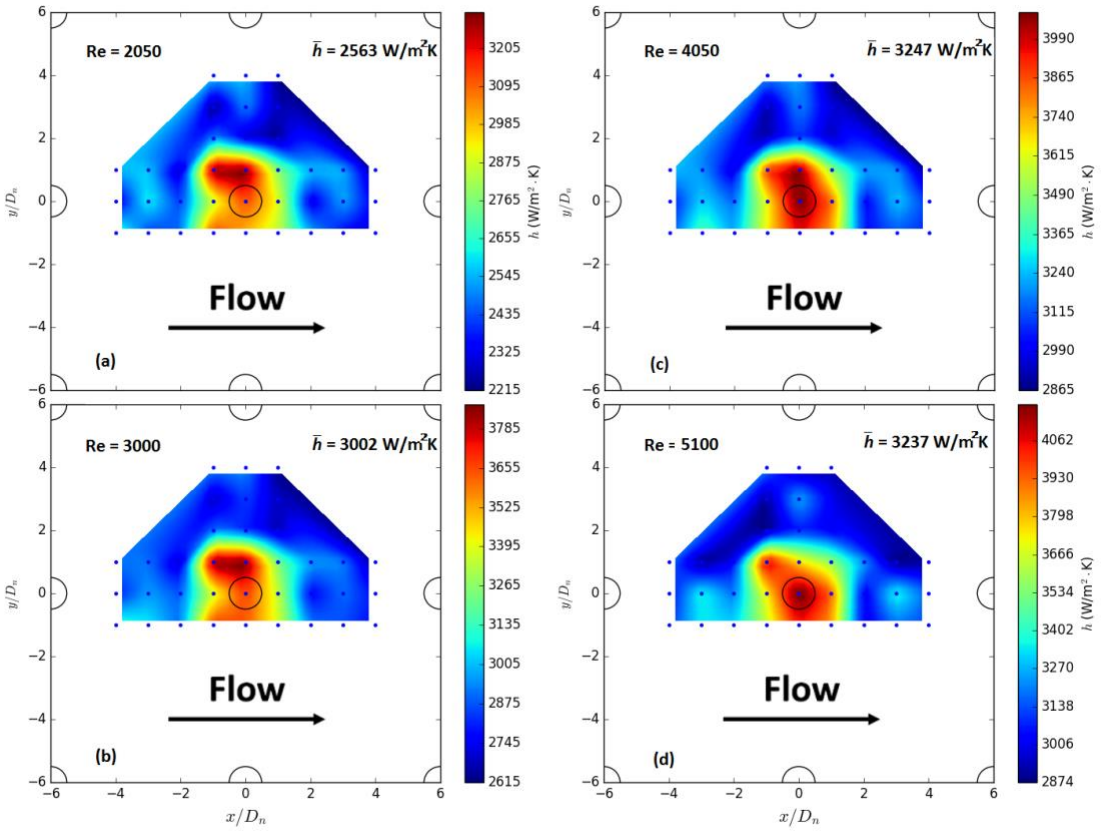

Figure 4.2: Surface heat transfer coefficient maps of water-ethylene glycol at increasing flow rates, plates geometries of $\gamma = 5$, $P^* = 6$, and $H^* = 1$

from $Re = 2050$ to 3000, and to a lesser degree from $Re = 3000$ to 4050. In the case of $Re = 5100$, however, a slight decrease in average heat transfer coefficient is observed. The average temperature rise between the inlet flow and the surface starts at a value of 30.4℃ for the lowest Reynolds number and reduces to 23.7℃ at the highest; this corresponds to a surface temperature of approximately 54.0℃ at the surface.

Also visible in Figure 4.2 is the presence of secondary cooling locations at distances halfway ($P^* = 3$) between the central nozzle and neighboring jets. The high Prandtl number of water-ethylene glycol is a result of both a higher viscosity and lower thermal diffusivity than pure water, meaning the mixture is more resistant to flow and slower at transporting thermal energy through its own fluid medium, and efficiently removing heated fluid from the surface becomes an even more significant consideration than it had been before.

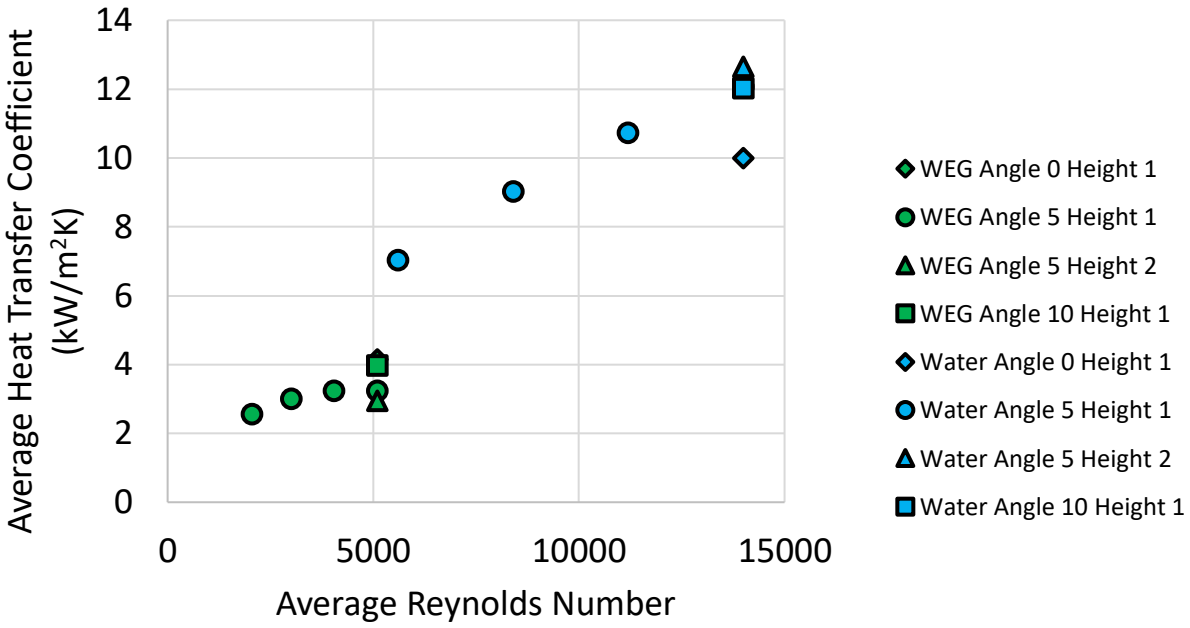

Figure 4.3: Average heat transfer coefficients for water and water-ethylene glycol

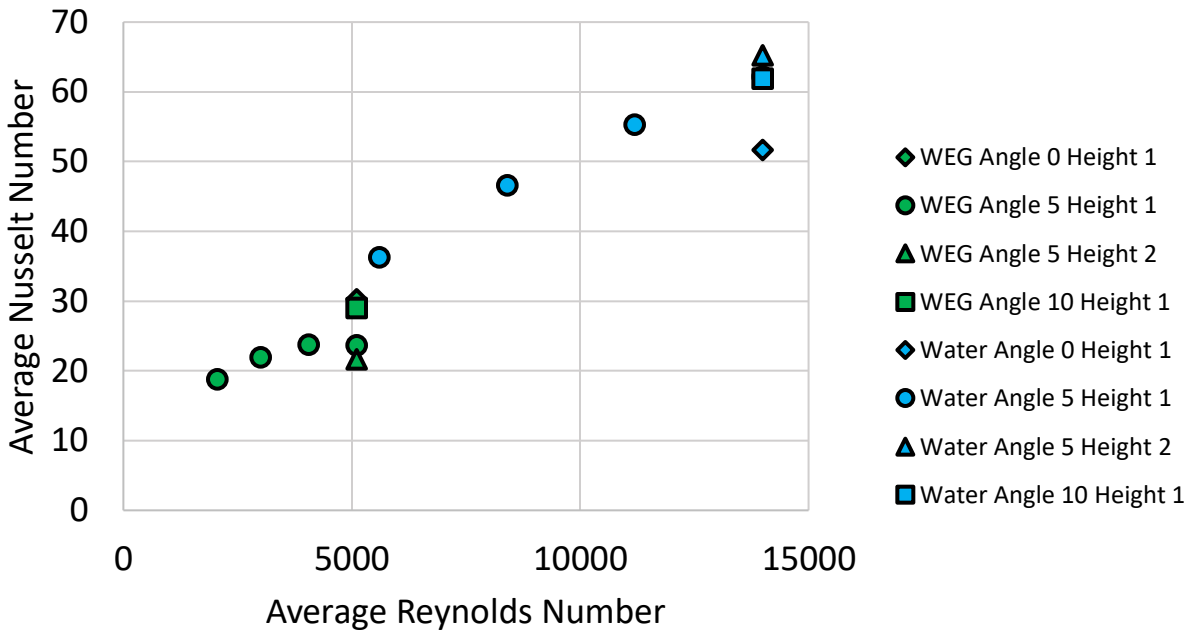

Figure 4.4: Average Nusselt numbers for water and water-ethylene glycol

Figures 4.3 and 4.4 show average heat transfer properties for all the water-ethylene glycol tests conducted as well as pure water tests for the same geometries for use as reference and contrast. The circular symbols represent the increasing flow rate runs featured in Figure 4.2, and it is clear that the heat transfer coefficients and Nusselt numbers increase more steeply for water, increasing from $Nu = 36.26$ to 62.21, than water-ethylene glycol, which increases from $Nu = 18.74$ to 23.67. At the angle $\gamma = 5°$ the test using water performed better at a height of $H^* = 2$ than at $H^* = 1$, where water-ethylene glycol experienced the opposite effect as indicated by the average heat transfer values in Table 4.4. If there is indeed a flow concern with $\gamma = 5$, $P^* = 6$, and $H^* = 1$ water-ethylene glycol test at $Re = 5100$, then the expected value of heat transfer coefficient would further support these opposing trends, and it can be gathered that having low plate-to-surface heights is likely to be better for water-ethylene glycol.

Table 4.4: Varying heights: water compared to WEG

	$\bar{h}\left(\frac{kW}{m^2K}\right)$	
Working Fluid	$H^* = 1$	$H^* = 2$
WEG	3.24	2.96
Water	12.08	12.66

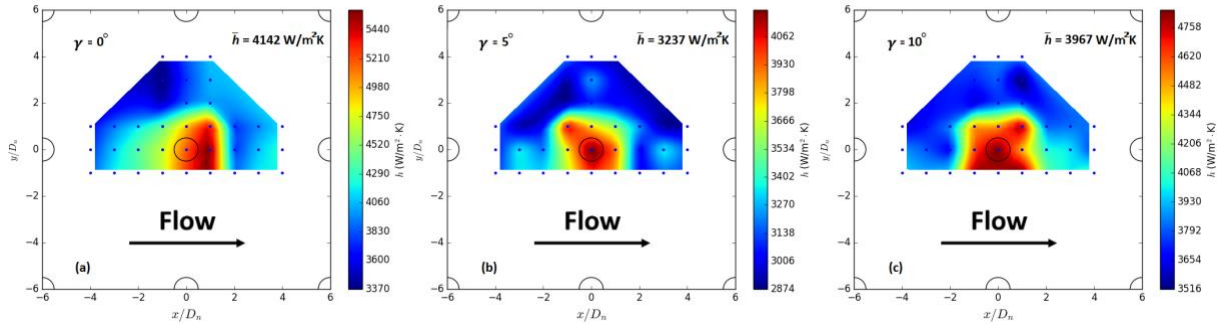

Figure 4.5: Surface maps of water-ethylene glycol with $P^* = 6,\ H^* = 1, Re = 5100$ an increasing manifold angle

There is not a clear trend in the effect of manifold angle when using water-ethylene glycol, as Figure 4.5 demonstrates that the plate with angle $\gamma = 5^\circ$ resulted in an average heat transfer of $\bar{h} = 2.5\ W/m^2K$ value 60 % lower than the $\gamma = 0^\circ$ and 10° plates' $\bar{h} \approx 4\ W/m^2K$. The rise of local heat transfer coefficients slightly downstream of the central nozzle in the $\gamma = 0^\circ$ plate compared to region upstream indicates the possibility that spent flow from the jet directly upstream could be interfering with the central jet, and generated an increase in heat transfer by chance. The $\gamma = 10^\circ$ plate produces a more strongly clustered area of heat transfer directly beneath the jet, and shows nothing that could indicated a spent flow management problem, and prevents ruling out angled manifolds as an entirely ineffective strategy to spent fluid management of water-ethylene glycol.

The study by Narumanchi [5] is significantly different in terms of geometry, i.e. number of nozzles used, surface features applied, and diameter of nozzle, and has results that focus on qualities ranging from surface wear to coefficient of performance to heat transfer coefficient; despite this there is one available line of comparison in what Narumanchi's group refers to as temperature uniformity, or the difference between the maximum and minimum temperatures for a given test. Narumanchi reported $2.7℃$ for their plain, circular surface with diameter $1.4\ mm$, where the results of the current study observed temperature uniformities ranging from $1.0℃$ to $3.5℃$ over a larger square area with side length $76.2\ mm$. The smaller ranges seen over the larger area in the current study support the case for water-ethylene glycol's compatibility with jet impingement arrays and angled confining walls.

4.3 Staggered Array Results and Discussion

A complete set of results is presented in Appendix D. The most significant results are presented in the following paragraphs to highlight the effects of varying nozzle patterns, manifold angle, and pitch in conjunction with water flowing through staggered arrays.

Figure 4.6 shows extrapolated surface maps of temperature rise for the various array patterns tested. The lowest temperature rises are seen for the in-line array (a) with values ranging between around 6 and 6.6 degrees. The highest temperature rises of 11.5 to 13 degrees are on the transverse staggered array (c), where there is no jet directly upstream from the center jet. This highlights the unevenness of cooling that could be expected along in the upstream portion of an expanded staggered array. The streamwise staggered array with the $P^* = 6$ (b) was able to keep the temperature rise below 10 degrees, but the array with a $P^* = 4$ (d) has the most pronounced

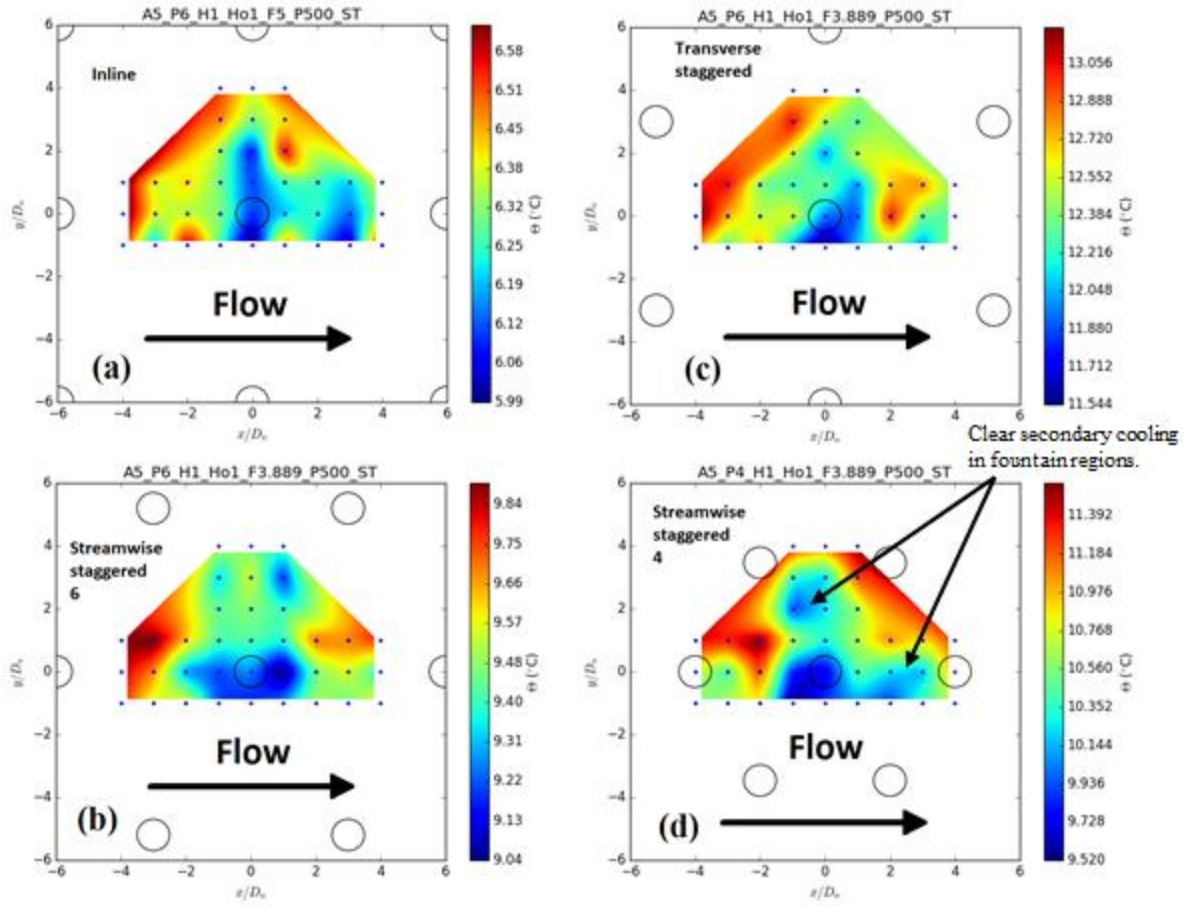

Figure 4.6: Temperature rise surface maps for varying patterns.
(a) Inline, $P^* = 6$ results from Maddox [13], (b) streamwise staggered array, $P^* = 6$,
(c) transverse staggered array, $P^* = 6$, and (d) streamwise staggered array, $P^* = 4$.
All maps are shown for $A^* = 5$, and $Re = 14000$.

fountain region effect. This last array had the largest range of local temperature rise in the area of interest, almost certainly due to the lack of upstream cooling.

For staggered arrays nozzle diameter was kept the same size as inline nozzles, but the number of nozzles was reduced from 9 to 7 which prevents a truly direct comparison between staggered and inline arrays. The decision was made to use only 7 nozzles for staggered arrays for several reasons, including the fact that the concept with inline array testing with the setup was to examine a single, central nozzle and the effects that adjacent nozzles had upon it as well as the

limitations of where nozzles could be placed and still be entirely on the plate and the concern of wall effects.

A marked increase in heat transfer occurs across the angles $\gamma = 2.5°$, 5°, and 7.5° for the streamwise staggered plates of both pitch values, $P^* = 4$ and $P^* = 6$. In the transverse staggered format, however, the $\gamma = 2.5°$ performed the best and the $\gamma = 5°$ performed the the worst. These trends can be seen in Figure 4.7 which indicates a significant increase in Nusselt number for the $\gamma = 2.5°, P^* = 6$ streamwise staggered plate. For the $Re = 14000$ test the $\gamma = 5°$ inline array used as a reference produced an average Nusselt number value of $Nu = 62.21$, while the $\gamma = 7.5°$ streamwise staggered array yielded $Nu = 56.57$, and the next largest value, $\gamma = 2.5°$ transverse staggered, was only $Nu = 41.90$.

A closer examination is provided by the local heat transfer coefficient surface maps for $P^* = 6$ at $Re = 14000$ for increasing angle from $\gamma = 2.5°$ (a) to $\gamma = 7.5°$ (c) shown in Figure

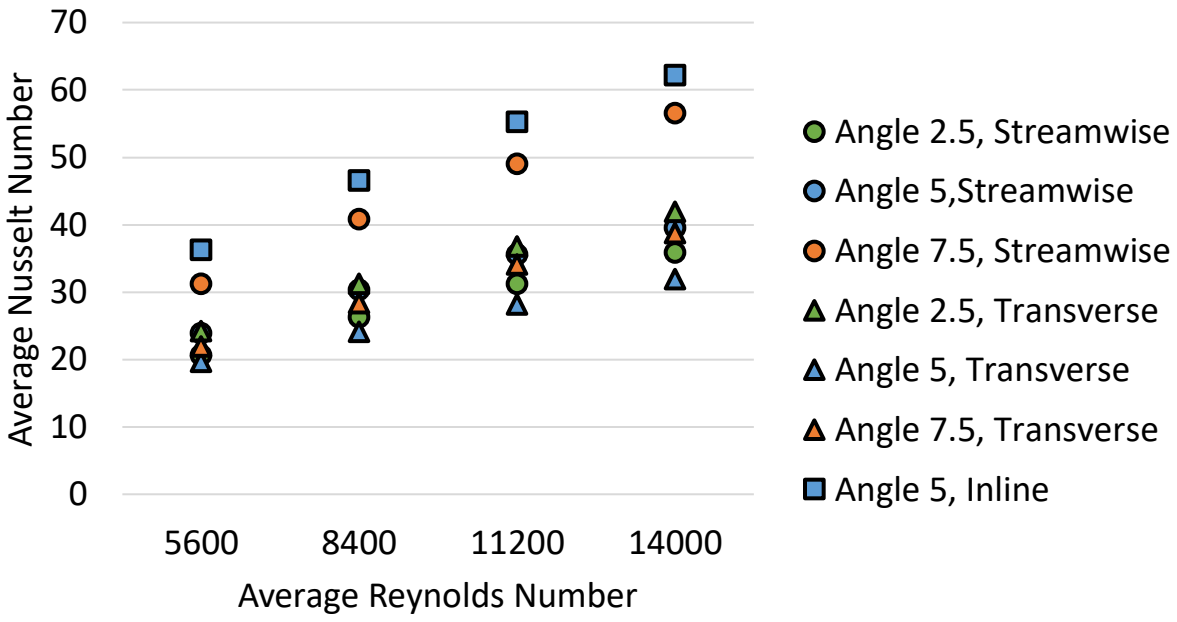

Figure 4.7: Nusselt numbers for varying angle and nozzle pattern for $P^* = 6$

4.8. An isolated region of high heat transfer, $h \approx 34.80\, kW/m^2K$, occurs immediately downstream of the central nozzle in the $\gamma = 7.5°$, compared to the upstream portion of the same region, $h \approx 14.10\, kW/m^2K$, and even further upstream where it drops down as low as $h \approx 3.75\, kW/m^2K$. While the quantitative average values produced are impressive, the stark imbalance is impractical.

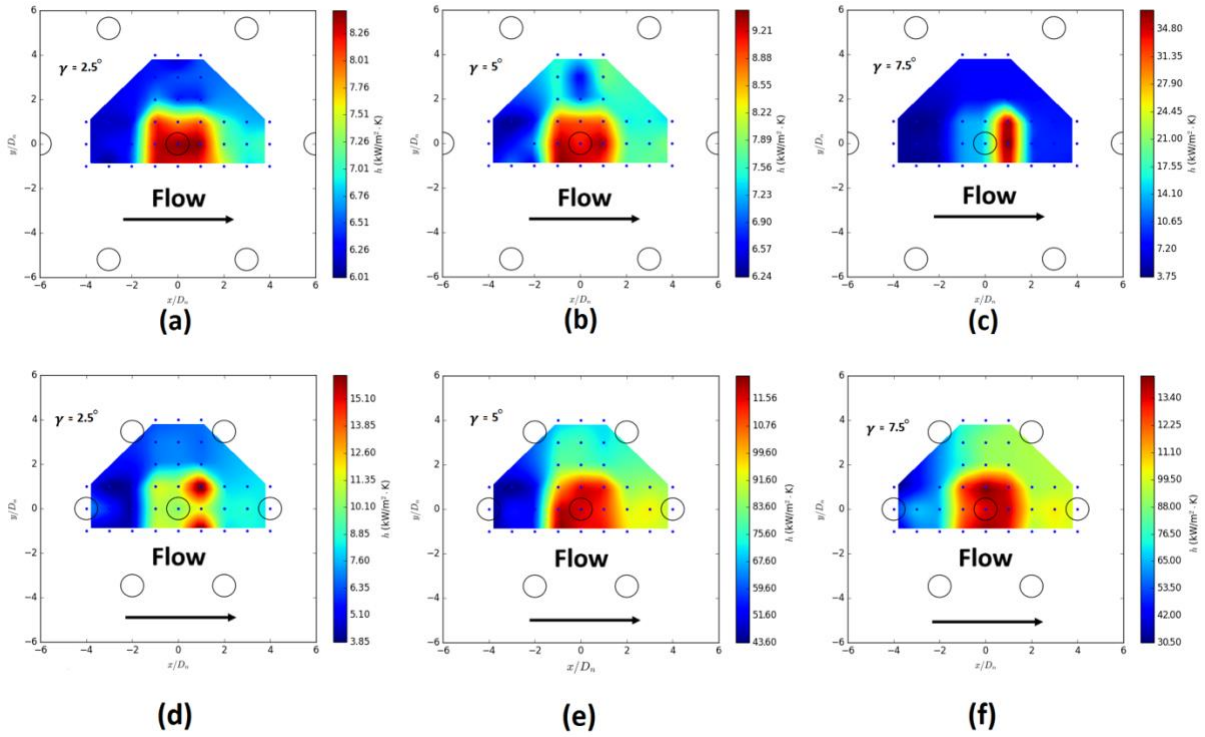

Figure 4.8: Surface maps of staggered plates with increasing angle at $Re = 14{,}000$ and $P^* = 6$ (a, b, c) and $P^* = 4$ (d, e, f)

The $\gamma = 7.5°$, $P^* = 4$ test of the same Reynolds number shows a more reasonable balance for the heat transfer, with a maximum value of $h \approx 13.5\, kW/m^2K$, spread across the central group. While the minimum value is low like the $P^* = 6$ version, this is much more likely due to the reduced pitch resulting in a lack of upstream heat transfer. This indicates the presence of a complex flow pattern produced from the $\gamma = 7.5°, P^* = 6$, plate geometry and further examination

should be carried out with this and similar geometries for greater understanding. Additional flow rates are presented in Appendix D.

Streamwise staggered plates with a pitch $P^* = 4$ consistently produced higher heat transfer than plates with pitch $P^* = 6$, and as $\gamma = 2.5°$ increases to $\gamma = 7.5°$. Figure 4.9 shows that the $\gamma = 7.5°, P^* = 4$ geometry matches Nusselt number values with the anomalous $\gamma = 7.5°, P^* = 6$. Results from a numerical study, discussed later, strengthens the idea of an inverted relationship between pitch and heat transfer for staggered arrays, and go on to suggest that the trend peaks around the pitch, $P^* = 3$, so a supplementary experiment was conducted using a plate with $\gamma = 5°, P^* = 3$. Experimental results corroborate the supposition of the numerical

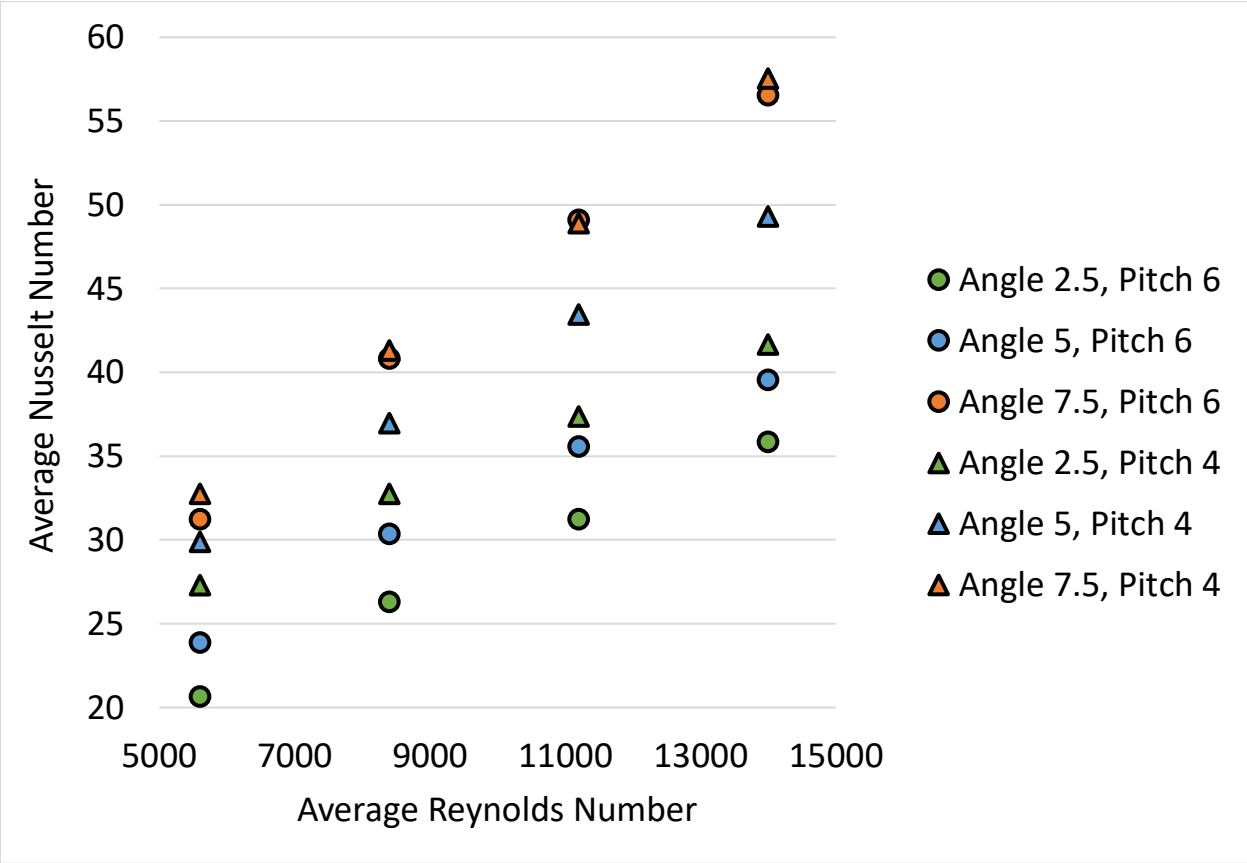

Figure 4.9: Nusselt numbers for varying angle and pitch using plates with the streamwise staggered pattern

results, at least to the extent that a trend of reducing pitch resulting in increased heat transfer approaching $P^* = 3$. Figure 4.10 shows the average Nusselt numbers for the $\gamma = 5°, P^* = 3$ plate compared to the values from $\gamma = 5°$, $P^* = 4$ and $P^* = 6$. Values smaller than $P^* = 3$ have not been tested experimentally, but the supposition is that further reducing the jet-to-jet spacing prevents fountain regions and exit flows from forming a stable flow pattern.

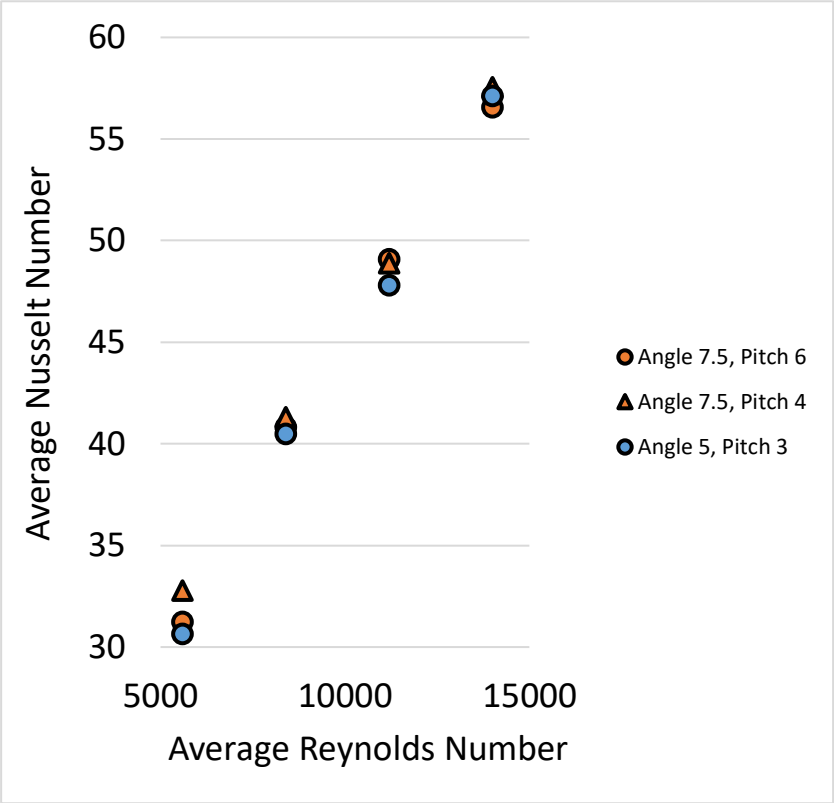

Figure 4.10: Nusselt numbers for $P^* = 3$ compared to higher valued results from $P^* = 4$ and 6.

Table 4.5 below is provided to give a comparison of approximate results from the staggered array portion of this study to those of a handful of the reviewed papers, discussed in Chapter 2, that are somewhat more relevant to this study. Arens et al. [22] found greater heat transfer for their inclined confining walls than tests where manifold had no angle. Michna and Browne [31] and Obot and Trabold [28] both noted greater results with greater 'area ratio' or 'open area', meaning jet area relative to heater area. The area of interest used in measurements in the current study is

small enough compared to the size of the jet arrays that reducing the pitch size from 6 to 3 is somewhat like reducing the area ratio.

Table 4.5: Geometries and results for select papers

Principal Author	$D_n\ (mm)$	Pattern	P^*	H^*	Re	$\bar{h}\ \left(\frac{kW}{m^2K}\right)$	Nu
Henry	3.175	staggered	3-6	1	8600-14000	3.5-12	20-60
Arens et al. [22]	1 – 1.65	inline	3[1]	3.18-3.33	1300-5000	15-35	35-90
Jorg et al. [16]	.6	single	none	5-7	800-4000	4-12	4-12
Mischna et. al. [31]	31-126 (μm)	inline & staggered	3.23-3.97	1.59-6.45	50-3500	40-400	5-75
Obot (air) and Traobld [28]	3.175	inline	6-10 (P/H)	2-16	1300-21000	Not listed	5-90

4.4 Numerical Comparison

A numerical study into jet impingement employing an expanding area manifold and a staggered jet pattern was conducted concurrently to, but separately from, this one. The ANSYS-based computer models were designed to examine an elongated strip of flow and heat transfer within the fluid and on the surface instead of focusing on the surface under a single jet. The differing geometry model incorporates several million data points and allows for a more thorough examination of turbulence and degradation effects in downstream jets as well as a finer view of phenomena in general. The variance in resolution is substantially noticeable in Figure 4.11 where experimentally obtained streamwise staggered surface plots are juxtaposed with numerically

[1] Where D = 1.5 mm

generated ones, at an angle of $\gamma = 5°$, pitch of $P^* = 3$, and Reynolds numbers of $Re = 8400, 11200$.

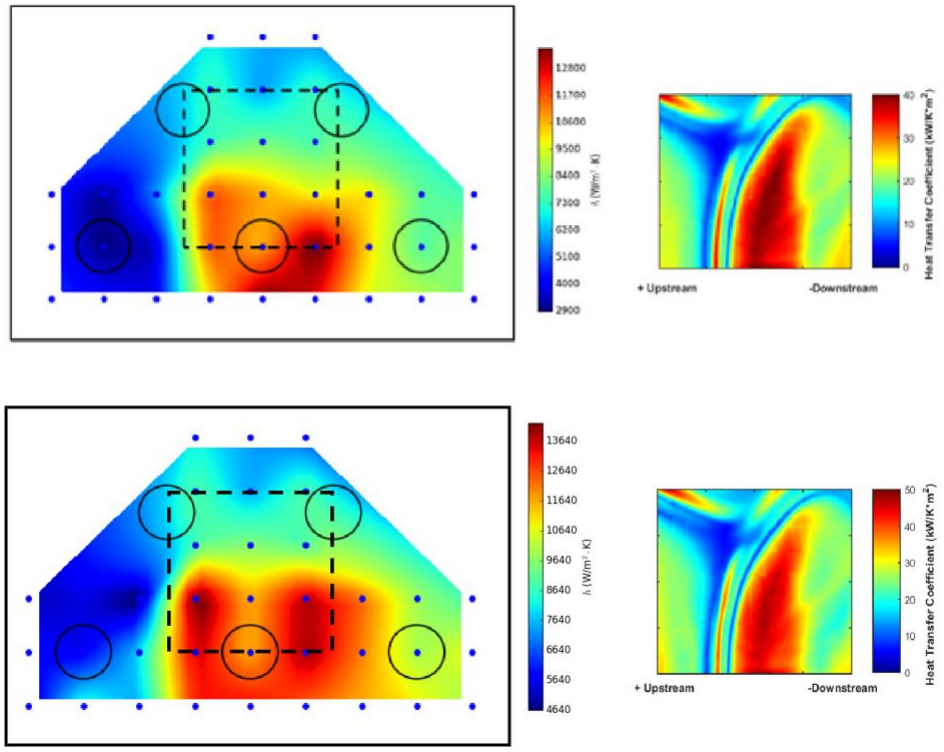

Figure 4.11: Comparison of experimental (left) and numerical (right) plots at $Re = 8400$ (top) and 11200 (bottom) for a streamwise staggered array with $P^* = 3$. The dotted line on the experimental plots delineate the approximate location of the area represented by the numerical plots.

The disparity between the numerical and experimental results tracks with the previously conducted surveys conducted by Maddox [11-13], where the average heat transfer coefficient, $\bar{h}$, heat flux, $\bar{q}''$, and temperature drops, $\bar{\theta}$, are roughly 3-4 times larger in the numerically generated data than the experimentally obtained values. These disparities could be attributed to many factors, including wall effects, unpredicted eddy flows, entrainment of fluid around the adjusting walls of the inner tank, and incongruences between the thermal properties of the actual working fluid and referenced values used in data reduction in the experimental setup, and the limitations of turbulence modelling and the assumption of an infinite space in the transverse directions.

In both experimentally and numerically obtained results, trends were observed to suggest that heat transfer increases with increasing Reynolds numbers, $\bar{h},\ \overline{Nu} \propto Re$, between $Re = 5600$ and 14000, increasing manifold angle, $\bar{h},\ \overline{Nu} \propto \gamma$, between $\gamma = 0°$ and $15°$, and decreasing pitch, $\bar{h},\ \overline{Nu} \propto \frac{1}{P^*}$, between $P^* = 3$ and $P^* = 6$. At pitches smaller than $P^* = 3$, the numerical study found that the proximity of jets suppressed the formation of steady fountain flow patterns. The numerical study also found that the entrainment of jet flows into spent fluid is reduced when angled confining walls are employed.

Chapter 5

Conclusions

Liquid jet impingement can operate with relatively high volumetric flow rates and low pressure drops, making impinging jets more tenable as a cooling system than other popular liquid cooling techniques. In larger scale applications, the greatest problem in jet impingement cooling is the entrainment of downstream jets into the crossflow of spent fluid. A scheme of employing an expanding area manifold to allow spent fluid a recourse was used for alleviating this effect.

An experimental setup was utilized to characterize changes in the heat transfer with varying geometries, flow rates, and working fluids. The setup was designed to be capable of recording local temperature, local surface heat transfer coefficient, and local surface heat flux data. A finer set of data was obtained by translating the test section across the surface to known points relative to measurement locations. The larger data set was then used to generate 2-D maps of the local thermal properties.

The applicability of water-ethylene glycol as a working fluid in this spent-fluid management scheme was examined using the parameters of Reynolds number, jet-to-surface height, and manifold angle containing a 3 x 3 inline array of submerged, normal, single-phase, liquid jets. The highest value of heat transfer coefficient observed with water-ethylene glycol testing was $4{,}000\ W/m^2K$ when $\gamma = 0°$ and $5°$, but for $\gamma = 0°$, distorted heat transfer coefficient values point towards jet degradation. The angled confining wall had mixed results, and when considering

the thermophysical properties of water-ethylene glycol, greater impacts may be seen when employing smaller pitch arrays.

A series of tests using water and 7-nozzle staggered arrays of submerged, single-phase, liquid jets were examined to more consistently locate regions of primary and secondary surface cooling. The effects of Reynolds number, manifold angle, pitch, and pattern orientation were investigated. In all cases, heat transfer coefficient increased with increased Reynolds number, and in flow patterns did not substantially change with the increases in Reynolds number. Distinct trends were observed with heat transfer coefficient increasing both with increasing manifold angle and decreasing pitch. Greater heat transfer values were seen underneath a jet with a jet directly upstream than in a jet with two jets indirectly upstream. The greatest heat transfer coefficients observed in staggered arrays were approximately $40{,}000\ W/m^2K$ and $20{,}000\ W/m^2K$ seen when test sections had the streamwise staggered pattern at $\gamma = 7.5$, $P^* = 6$ and $\gamma = 5$, $P^* = 3$. but in the case of the former, the heat transfer was poorly spread, likely indicating a detrimental flow pattern occurring in the specific geometry. The average Nusselt numbers are more comparable, around $\overline{Nu} = 57$ for both tests.

A note to make in light of these results is that manifold design will change results, but not the trends. This study focused on a central jet, its neighboring jets, and the interactions between these jets. Focusing on a single, upstream jet and its neighbors, it is difficult to make any assertions about the continuing integrity of downstream jets. A numerical sister study was conducted using computational fluid dynamics software ANSYS to confirm integrity of jets further downstream, more convincingly characterize flow phenomena, and assist in determining geometry selection for future study.

5.1 Suggestions for future work

As an empirical field of study, jet impingement requires a lot of experimental information to be accrued to make solid conclusions, and the accuracy of the conclusions can generally be improved by expanding the amount of data amassed. This means that further testing of topics in this study would be valuable:

- Inline arrays using water-ethylene glycol
- Investigating an expansion on the range of angles, heights, pitches, and other values for staggered array with water beyond the results presented in this paper.
- Staggered arrays using water-ethylene glycol
- Downstream testing with angled manifolds[1]
- Flow and heat transfer characteristics edge of staggered arrays[1]

Simple jet impingement has a large numer of parameters that can serve as the focus of study. Adding in any substantial change, such as a spent fluid management strategy, for a specific application or otherwise, warrants that all the considerations for simple jet impingement be re-examined, including any other substantial changes that may be compatible. For example, a spent fluid strategy can often be combined with a modification to inlet flow as shown by Ianiro and Cardone, Arens, et. al., and Trabold and Odot [21, 22, 27], or an enhancement to the surface as Moreno, et. al., Narumanchi, et. al., and several other groups have done [1, 5, 18, 24 -26, 29]. One could go even beyond that and mix a large number of changes, i.e. the modifications presented by each of Ianiro and Cardone, Arens, et. al., and Trabold and Odot do not prevent any of the others from also being applied. Therefore individual suggestions listed below are parameters that can be

[1] Would likely require a substantial change to setup

tested in conjunction with staggered arrays and an expanding manifold spent, but do not preclude other suggestions from also being investigated. Reviewed papers from Chapter 2 that deal with the suggested topics are referenced.

- Inlet/outlet geometry of jets to ease pressure drop [4]
- Outlet geometry to induce turbulence in jet
- Surface roughness within nozzle [27]
- An array of jets with increased diameter at the edge of the array [22] or similar change to compensate for weak heat transfer at boundaries
- Angled jets instead of normal ones
- Internal geometry that generates to induce tangential flow [21]
- Microstructures/roughness on the heated surface[1] [1, 5, 18, 24 -26, 29]
- Orientation of the heated surface[1]

[1]Would require a substantial change to setup

Bibliography

[1] Moreno, Gilbert. "Power electronics thermal management R&D." Retrieved September, 15 2016 from http://www.nrel.gov/docs/fy16osti/64943.pdf, (2016).

[2] Lee, D.-Y., and Vafai, K. “Comparative analysis of jet impingement and microchannel cooling for high heat flux applications”. *Int. J. Mass Heat Trans.*, 42(9), pp. 1555–1568, (1999).

[3] Robinson, A. J. “A thermal–hydraulic comparison of liquid microchannel and impinging liquid jet array heat sinks for high-power electronics cooling”. *Components and Packaging Technologies*, IEEE Transactions on, 32(2), pp. 347–357, (2009).

[4] Whelan, B. P., and Robinson, A. J., “Nozzle geometry effects in liquid jet array impingement”. *Applied Thermal Engineering*, 29(11), pp. 2211–2221, 2009.

[5] Narumanchi, S., Mihalic, M., Moreno, G., and Bennion, K. “Design of light-weight, single-phase liquidcooled heat exchanger for power electronics”. In the *13th Intersociety Conference on Thermal and Thermomechanical Phenomena in Electric Systems* (ITHERM), 2012, IEEE, pp. 693–699.

[6] Rattner, A. S. “General characterization of jet impingement array heat sinks with interspersed fluid extraction ports for uniform high-flux cooling”. ASME. *J. Heat Transfer*. 2017.

[7] Aranzabal, I., Martinez de Alegria, J. I., Garate, J., Andreu and Delmonte, N. "Two-phase liquid cooling for electric vehicle IGBT power module thermal management," *2017 11th IEEE International Conference on Compatibility, Power Electronics and Power Engineering (CPE-POWERENG)*, Cadiz, 2017, pp. 495-500.

[8] Zuckerman, N. and Lior, N. “Jet impingement heat transfer: Physics, correlations, and numerical modeling,” Adv. in Heat Trans., 39(06):565-631. (2006).

[9] Brunschwiler, T., Rothuizen, H., Fabbri, M., Kloter, U., Michel, B., Bezama, R., and Natarajan, G., 2006. "Direct liquid jet-impingment cooling with micron-sized nozzle array and distributed return architecture". In the *10th Intersociety Conference on Thermal and Thermomechanical Phenomena in Electronics Systems* (ITHERM), 2006, IEEE, pp. 196–203.

[10] Onstad, A. J., Elkins, C. J., Moffat, R. J., and Eaton, J. K., 2009. "Full-field flow measurements and heat transfer of a compact jet impingement array with local extraction of spent fluid". *Journal of Heat Transfer*, 131(8), p. 082201.

[11] Maddox, J.F., Knight, R.W., Bhavnani, S.H. and Pool, J. "Correlation for single phase liquid jet impingement with an angled confining wall for power electronics cooling." Proc 15th Int. Conf. on Therm. and Thermomech. Phen. in Elect. Sys. (ITHERM), IEEE, (2016).

[12] Maddox, J.F., Knight, R.W. and Bhavnani, S.H. "Local thermal measurements of a confined array of impinging liquid jets for power electronics cooling". Therm. Meas., Modeling & Management Symp. (SEMI-THERM), 2015 31st , pp. 228-234.IEEE. (March 2015).

[13] Maddox, J., Liquid jet impingement with spent flow management for power electronics cooling, Ph.D. Thesis, Auburn University, (2015).

[14] Rohlfs, W., Bieber, M., Ehrenpreis, C., Jörg, J., Sabelberg, E. and Kneer, R., Flow structures and heat transfer characteristics in arrays of submerged laminar impinging jets. *Proc. Appl. Math.* Mech., 16: 953–956, (2016).

[15] Attalla, M., et al. "Influence of the nozzle shape on heat transfer uniformity for in-line array of impinging air jets." *Applied Thermal Engineering*, vol. 120, 2017, pp. 160–169.

[16] Jörg, J., Taraborrelli, S., Sarriegui, G., De Doncker, R. W., Kneer, R., and Rohlfs, W. "Direct Single Impinging Jet Cooling of a MOSFET Power Electronic Module," in *IEEE Transactions on Power Electronics*, vol. PP, no. 99, pp. 1-1.

[17] Selvaraj, P., Natesan, K., Velusamy, K & Sundararajan, T. "Cooling of small size irradiation specimens using impinging jets". *Journal International Communications in Heat and Mass Transfer*. 84. 20-26, (2017).

[18] Sui, Y., Zhang, H., Li, P., and Lin, T. "Design analysis of minichannel heat sink with indented fins under impingement flow condition," *2017 18th International Conference on Electronic Packaging Technology (ICEPT)*, Harbin, 2017, pp. 336-341.

[19] Leena, R., Syamkumar, G., and Jose Prakash, M."Experimental and numerical analyses of multiple jets impingement cooling for high-power electronics," in *IEEE Transactions on Components, Packaging and Manufacturing Technology*, vol. 8, no. 2, pp. 210-215, Feb. 2018.

[20] Kashi, B., and Haustein, H. D. "Dependence of submerged jet heat transfer on nozzle length", *International Journal of Heat and Mass Transfer*, Volume 121, 2018, Pages 137-152, ISSN 0017-9310.

[21] Ianiro, A., and Cardone, G. "Heat transfer rate and uniformity in multichannel swirling impinging jets", Applied Thermal Engineering, Volume 49, 2012, Pages 89-98, ISSN 1359-4311.

[22] Arens, N. R., Morem, M. P., Doom, J., Michna, G. J. "Reducing crossflow effects in arrays of impinging jets". ASME. Heat Transfer Summer Conference, *Volume 1: Aerospace Heat Transfer; Computational Heat Transfer; Education; Environmental Heat Transfer; Fire and Combustion Systems; Gas Turbine Heat Transfer; Heat Transfer in Electronic Equipment; Heat Transfer in Energy Systems*, 2017.

[23] Yeranee, K.; Wae-hayee, M.; Piya, I.; Rao, Y.; Nuntadusit, C. "The study of flow and heat transfer characteristics of impinging jet array mounting air-induced duct" IOP Conference Series: Materials Science and Engineering, Volume 243, Issue 1, pp. 012001 (09/2017).

[24] Moreno G, Narumanchi S, Venson T, Bennion K. "Microstructured surfaces for single-phase jet impingement heat transfer enhancement". ASME. *J. Thermal Sci. Eng. Appl.* 2013.

[25] Han, Y., Lau, B. L., Tang, G., Zhang, X., and Rhee, D. M V. "Si-based hybrid microcooler with multiple drainage microtrenches for high heat flux cooling," in *IEEE Transactions on Components, Packaging and Manufacturing Technology*, vol. 7, no. 1, pp. 50-57, Jan. 2017.

[26] J. Ditri, M. K. McNulty, and Igoe, S. "S3-P10: Embedded microfluidic cooling of high heat flux electronic components," *2014 Lester Eastman Conference on High Performance Devices (LEC)*, Ithaca, NY, 2014, pp. 1-4.

[27] Trabold, T. A., and Obot, N.T. "Impingement heat transfer within arrays of circular jets: part II—effects of crossflow in the presence of roughness elements". ASME. *J. Turbomach.* 1987;109(4):594-601.

[28] Obot, N. T., and Trabold, T. A. "Impingement heat transfer within arrays of circular jets: part I—effects of minimum, intermediate, and complete crossflow for small and large spacings". ASME. *J. Heat Transfer.* 1987;109(4):872-879.

[29] Ditri, J., Hahn, J., Cadotte, R., McNulty, M., and Luppa, D. “Embedded cooling of high heat flux electronics utilizing distributed microfluidic impingement jets”. ASME. *International Electronic Packaging Technical Conference and Exhibition, Volume 3*

[30] Karwa, N., Stanley, C., Intwala, H., and Rosengarten, G.“Development of a low thermal resistance water jet cooled heat sink for thermoelectric refrigerators”. *Journal Applied Thermal Engineering.*

[31] Michna, J., Browne, E. A., Peles, Y., and Jensen, M. K. “The effect of area ratio on microjet array heat transfer”. *International Journal of Heat and Mass Transfer*. 54. 9. (2011).

[32] *Fluid Properties Calculator*, www.mhtl.uwaterloo.ca/old/onlinetools/airprop/airprop.html.

[33] Moffat, R. J. “Using uncertainty analysis in the planning of an experiment”. *Journal of Fluids Engineering*, 107:173-178, 1985.

[34] Moffat, R. J. “Describing the uncertainties in experimental results”. *Experimental Thermal and Fluid Science*, 1(1):3-17, 1988.

Appendix A

Data Acquisition

A.1 Procedure

In order for the system to perform as intended, the steps for assembling and adjusting the flow chamber need to be performed in a particular order.

A.1.1 Opening the Flow Chamber

1. close the valve beneath the liquid reservoir to prevent the chamber from overflowing when it is opened
2. loosen the top needle valve to relieve the pressure from the lid
3. loosen one of the *x*-direction needle valves by six turns to relieve the pressure from the wall studs against the holes in the lid (keep track of which was loosened)
4. loosen all the wing nuts on the top of the tank by half a turn to relieve the tension
5. finish unscrewing and remove all the wing nuts from the top of the tank
6. tighten the top needle valve to separate the lid from the gasket along the walls (if only one side lifts off of the gasket, it may be necessary to push down on the side that side to force the other side to lift separate as well)
7. remove the lid from the tank and set aside tighten the *x*-direction needle valve, that was loosened in step 3, back to its original location (six turns) to relieve the pressure from the walls of the tank on the interior

8. tighten the *x*-direction needle valve, that was loosened in step 3, back to its original location to relieve the pressure from the walls of the tank on the interior top wall
9. gently peel the rubber gasket apron from the wall of the chamber
10. use the rubber gasket to pull the top wall out of the chamber and set aside

A.1.2 Closing the Flow Chamber

1. ensure that the *x*-direction needle valves are tightened (this pushes the side wall apart slightly, allowing room for the interior top wall to be inserted)
2. ensure that the liquid level in the chamber is flush with the top of the interior movable side wall
3. place the interior top wall into the chamber and align the gasket with the studs extending from the exterior walls of the chamber
4. loosen one of the *x*-direction needle valves by six turns
5. loosen the needle valve on the lid
6. place the lid onto the chamber
7. replace all the wing nuts and tighten them gradually until all are snug
8. tighten the *x*-direction needle valve that was loosened in the step 4 back to its original location
9. tighten the lid needle valve until it is snug

A.1.3 Replacing the Jet Plate

1. open the chamber following the steps in A.1.1
2. loosen one of the *x*-direction needle valves by six turns

3. loosen the *y*-direction translation screws on one side by three turns
4. remove the plenum wall on the downstream side of the chamber
5. remove the old jet plate from the chamber
6. place the new jet plate into the chamber (ensure bubbles are not trapped beneath the plate))
7. replace the plenum wall on the downstream side of the chamber
8. inspect the plenum wall to ensure that the opening in the plenum wall is the correct size for the plate being tested
9. tighten the *y*-direction translation screws that were loosened in step 3 back to their original location
10. tighten the *x*-direction needle valve that was loosened in step 2 back to its original location
11. close the chamber following the steps in A.1.2

A.1.4 Translating in the *x*-direction

1. loosen the lid needle valve
2. loosen the *y*-direction translation screws on one side by three turns
3. loosen the *x*-direction needle valve on the side that the plate will be moving towards (3 full turns of the handle will move the needle 3.175mm (1/8"))
4. tighten the *x*-direction needle valve on the opposite side to push the inner chamber in the desired direction
5. tighten the *y*-direction translation screws that were loosened in step 2 back to their original location

6. tighten the lid needle valve until it is snug

A.1.5 Translating in the *y*-direction

1. loosen the lid needle valve
2. loosen one of the *x*-direction needle valves by three turns
3. loosen the *y*-direction translation screws on the side that the plate will be moving towards (2.5 turns of the screw will move the tip by 3.175mm (1/8"))
4. loosen the *y*-direction translation screws on one side by three turns
5. tighten the *y*-direction translation screws on the opposite side to push the inner chamber in the desired direction
6. tighten the *x*-direction needle valve that were loosened in step 2 back to their original location
7. tighten the lid needle valve until it is snug

A.1.6 Changing the Height of the Jet Plate

1. open the chamber following the steps in A.1.1
2. loosen one of the **x**-direction needle valves by six turns
3. loosen the **y**-direction translation screws on one side by three turns
4. turn the four set screws in the jet plate clockwise to raise the plate or counter-clockwise to lower the plate (three full turns with change the elevation by 3.175 mm (1/8"))
5. tighten the **y**-direction translation screws that were loosened in step 3 back to their original location

6. tighten the **x**-direction needle valve that was loosened in step 2 back to its original location
7. close the chamber following the steps in A.1.2

A.1.7 Initializing the System

1. turn on the chiller
2. set the chiller to approximately 21°C
3. ensure that the valve beneath the liquid reservoir is open
4. ensure that the pump/VFD is plugged into a 3-phase power outlet
5. flip the “On/Off” toggle switch to “On”
6. flip the “Local/Remote” toggle switch to “Local”
7. turn the pump frequency to the desired value (40-50)
8. point the bypass tube into the liquid reservoir and open its valve to allow the liquid to push the air out of the tube
9. close the bypass tube and elevate it to allow the vapor bubbles to collect in it upstream of the flow chamber
10. let the system run for 10-20 minutes to allow the temperatures to equalize

A.2 Considerations for Potential Revisions to the Test Chamber Design

The experimental test chamber used for this study was an original design by Maddox [11-13], and can function as the test chamber for study in the future. There are factors, however, that could be considered when moving forward to facilitate the convenience of future testing. These are listed below in no particular order with some explanation for context. These are presented as

notes, because while they would be helpful, they would not necessarily be applicable, affordable, or required in future versions of the experiment setup.

- Quick release lid – the current setup requires tightening the lid closed using a series of wingnuts. Additionally, it relies on deflection of the side walls to play a role attaching the lid. These are done to establish a strong enough seal to contain the working fluid, but they induce stress in side walls which can cause small fractures to form. This is not generally a problem for water testing, but water-ethylene glycol is more viscous than water, and serves as a lubricant in crack propgation.
- Bonded seams/viewing window – the current setup was designed with aspirations towards Particle Image Velocimetry (PIV) for flow characterizations, and a see-through Lexan polycarbonate was selected as the wall material. Seams between adjoining walls are sealed using gaskets compressed between the plates with fasteners and wingnuts, which induce stress in the side walls. The PIV was ruled untenable with the presence of adjustment screws and inner walls. Future iterations of the project would benefit from either using a material that can be fused at the seams (Lexan releases toxins when welded) or designed with a viewing window in mind. Changing plates requires the removal of the lid, so it cannot be fused.
- Vapor release mechanism – when attaching the lid and in the initial runs after changing plates and fluids there is a likelihood of air being trapped in the test chamber above the outlet/inlet channels. Particularly in water-ethylene glycol testing the working fluid at the liquid-vapor interface can entrain the air and generate a foam that can upset the flow loop if enough forms. Currently, vapor can be released by loosening the tightening screws in the lid, but this can lead to loss of working fluid and repeats stress in the walls as mentioned

above. Including an orifice in the lid that can be tightly plugged for testing would help in ensuring the impingement tank is completely filled before testing.

- Fluid removal – In the current set up, whenever the chamber needs emptied for maintenance or replacing the working fluid, the tank can drain until the fluid level drops below the inlet/outlet flow channels, but then is removed manually using sponges. If conservation of working fluid is a consideration, as with water-ethylene glycol tests, this can result in particulates from the sponge transferring to the working fluid. The high positioning of the outlet flow also means that fluid has to push up to the outlet after leaving the impingement regions, which is more difficult for fluids with higher viscosity. Lowering the outlet channel would provide for more fluid to leave the system before sponges are necessary and be more conducive to flow of higher-viscosity working fluids, which may be better for the life of the pump.
- Motor operational range – the current setup was originally used to run tests with water near its maximum speed (60 Hz on the VFD). Replacing the motor with one that has a greater operational range increases the options for testing with more viscous water-ethylene glycol and larger numbers of nozzles per test plate.

Greater capacity for test plates – the current setup has some, but limited, availability for testing using test plates large than 0.0762 m (3”) on a side, but future testing may require larger test plates. For example, longer plates in the streamwise direction can be used to experimentally confirm the alleviation of degradation effects.

Appendix B

Data Reduction

B.1 Calculating Local Surface Values

A manual series of data reduction has been demonstrated here to display how raw temperature measurements are transformed into a surface map. The reduced data set[1] provided in Table B.1 is for the inlet temperature, $T_{TC,in}$, of flow into the chamber as well as each group of embedded thermocouples: upstream, $T_{TC,1} - T_{TC,3}$, central, $T_{TC,4} - T_{TC,6}$, downstream, $T_{TC,7} - T_{TC,9}$, and transverse, $T_{TC,10} - T_{TC,12}$.

Table B.1: Sample temperature data[1]

Upstream			Central			Downstream			Transverse			
$T_{TC,1}$ (℃)	$T_{TC,2}$ (℃)	$T_{TC,3}$ (℃)	$T_{TC,4}$ (℃)	$T_{TC,5}$ (℃)	$T_{TC,6}$ (℃)	$T_{TC,7}$ (℃)	$T_{TC,8}$ (℃)	$T_{TC,9}$ (℃)	$T_{TC,10}$ (℃)	$T_{TC,11}$ (℃)	$T_{TC,12}$ (℃)	$T_{TC,in}$ (℃)
40.45	41.33	41.95	40.01	41.30	42.04	40.19	41.31	42.32	39.88	40.85	41.57	29.77
40.47	41.34	41.96	40.04	41.32	42.07	40.20	41.32	42.32	39.89	40.85	41.58	29.77
40.48	41.35	41.96	40.06	41.32	42.07	40.23	41.32	42.35	39.91	40.87	41.59	29.76
40.47	41.36	41.93	40.03	41.33	42.07	40.23	41.33	42.34	39.90	40.86	41.59	29.76
40.46	41.33	41.93	40.03	41.33	42.06	40.21	41.31	42.32	39.89	40.86	41.59	29.77

Since the surface value calculations for each thermocouple group are completed independently of each other, only calculations for the central thermocouple group will be carried

[1] While only 5 measurements per thermocouple are presented here, several hundred data points are obtained for every 30 minute run.

out in detail when appropriate. Quantities are being rounded to four significant digits for this demonstration.

Use the inlet temperature as a reference point for standardizing the temperature data by establish temperature rises.

$$\Theta_{TC,i} = T_{TC,i} - T_{TC,in} \tag{B.1}$$

$$\Theta_{TC,4} = T_{TC,4} - T_{TC,in}$$

$$= 40.01℃ - 29.77℃ \tag{B.2}$$

$$= 10.24℃$$

Then find the average of these values for use in a linear regression.

$$\bar{\Theta}_{TC,i} = \frac{1}{n}\sum_{j=1}^{n} \Theta_{TC,ij} \tag{B.3}$$

$$\bar{\Theta}_{TC,4} = \frac{1}{5}\sum_{j=1}^{5} \Theta_{TC,4j}$$

$$= \frac{1}{5}(10.24℃ + 10.27℃ + 10.3℃ + 10.27℃ + 10.26℃) \tag{B.4}$$

$$= 10.27℃$$

The temperature difference values and averages for each thermocouple are notated in Table B.2

Table B.2: Individual and average temperature values

Upstream			Central			Downstream			Transverse		
$\Theta_{TC,1}$ (℃)	$\Theta_{TC,2}$ (℃)	$\Theta_{TC,3}$ (℃)	$\Theta_{TC,4}$ (℃)	$\Theta_{TC,5}$ (℃)	$\Theta_{TC,6}$ (℃)	$\Theta_{TC,7}$ (℃)	$\Theta_{TC,8}$ (℃)	$\Theta_{TC,9}$ (℃)	$\Theta_{TC,10}$ (℃)	$\Theta_{TC,11}$ (℃)	$\Theta_{TC,12}$ (℃)
10.68	11.56	12.18	10.24	11.53	12.27	10.42	11.54	12.55	10.11	11.08	11.8
10.7	11.57	12.19	10.27	11.55	12.3	10.43	11.55	12.55	10.12	11.08	11.81
10.72	11.59	12.2	10.3	11.56	12.31	10.47	11.56	12.59	10.15	11.11	11.83
10.71	11.6	12.17	10.27	11.57	12.31	10.47	11.57	12.58	10.14	11.1	11.83
10.69	11.56	12.16	10.26	11.56	12.29	10.44	11.54	12.55	10.12	11.09	11.82
10.7	11.58	12.18	10.27	11.55	12.3	10.45	11.55	12.56	10.13	11.09	11.82

The linear regression that is applied generates an expression for temperature difference with respect to position in the *z*-direction, where $z = 0$ at the surface and $z < 0$ below the surface,

$$\Theta = m_g z + b_g \tag{B.5}$$

where the subscript, *g*, denotes any given thermocouple group, the slope of the line, m_g, is given by

$$m_g = \frac{\sum_i (z_{TC,i} - \bar{z}_g)(\bar{\Theta}_{TC,i} - \bar{\Theta}_g)}{\sum_i \left(z_{TC,i} - \bar{z}_g\right)^2}, \tag{B.6}$$

the position, *z*, is known for each thermocouple to be

$$z_{TC,1} = z_{TC,4} = z_{TC,7} = z_{TC,10} = -0.003\, m \tag{B.7}$$

$$z_{TC,2} = z_{TC,5} = z_{TC,8} = z_{TC,11} = -0.008\, m \tag{B.8}$$

$$z_{TC,3} = z_{TC,6} = z_{TC,9} = z_{TC,12} = -0.013\, m, \tag{B.9}$$

and the intercept, b_g, is calculated with

$$b_g = \bar{\Theta}_g - m_g \bar{z}_g. \tag{B.10}$$

The mean TC group temperature difference and position are calculated by

$$\bar{\Theta}_2 = \frac{\bar{\Theta}_{TC,4} + \bar{\Theta}_{TC,5} + \bar{\Theta}_{TC,6}}{3}. \tag{B.11}$$

$$\bar{z}_2 = \frac{\bar{z}_{TC,4} + \bar{z}_{TC,5} + \bar{z}_{TC,6}}{3} \tag{B.12}$$

Carrying out the linear regression with the central group gives,

$$\begin{aligned} \bar{\Theta}_2 &= \frac{10.27℃ + 11.55℃ + 12.3℃}{3} \\ &= 11.37℃ \end{aligned} \tag{B.13}$$

$$\begin{aligned} \bar{z}_2 &= \frac{(-0.003\ m) + (-0.008\ m) + (-0.013\ m)}{3} \\ &= -0.008\ m \end{aligned} \tag{B.14}[1]$$

$$\begin{aligned} m_2 &= \frac{\sum_{i=4}^{6}(z_{TC,i} - \bar{z}_2)(\bar{\Theta}_{TC,i} - \bar{\Theta}_2)}{\sum_{i=4}^{6}\left(z_{TC,i} - \bar{z}_2\right)^2} \\ &= \frac{(-0.003\ m - [-0.008\ m])(10.27℃ - 11.37℃) + \cdots}{(-0.003\ m - [-0.008\ m])^2 + \cdots} \\ &= -202.0\ \frac{℃}{m} \end{aligned} \tag{B.15}$$

[1] Equations B.12 and B.14 operate using only constant; as such the average TC group position will be a constant.

$$b_2 = \bar{\Theta}_2 - m_2 \bar{z}_2$$

$$= 11.37℃ - \left(-202.0 \frac{℃}{m}\right)(-0.008\, m) \tag{B.16}$$

$$= 9.75℃$$

The values in equations B.15 and B.16 approximately correspond to the temperature gradient and temperature rise at the surface.

$$\left.\frac{\partial T_g}{\partial z}\right|_{z=0} \approx m_g \tag{B.17}$$

$$\Theta_g \approx b_g \tag{B.18}$$

Fourier's law and the estimated temperature gradient can be used to obtain the local heat flux,

$$\dot{q}_g'' = -k_c \left.\frac{\partial T_g}{\partial z}\right|_{z=0} \tag{B.19}$$

with $k_c = 401\ W/(m \cdot K)$ is the thermal conductivity of the copper block.

The local heat flux obtained in equation B.19 can be used with the estimated surface temperature rise from equation B.18 to find the surface heat transfer coefficient using Newton's law of cooling,

$$h_g = \frac{\dot{q}_g''}{\Theta_g}. \tag{B.20}$$

This, in turn, can be used to find the local Nusselt number,

$$Nu_{D_n,g} = \frac{h_g D_n}{k_w} \tag{B.21}$$

where the inside nozzle diameter, D_n = 3.175 mm and $k_w = 0.614\ kW/(m \cdot K)$ is the thermal conductivity of the water.

For the water-ethylene glycol tests the k_{WEG} of 50% water, 50% ethylene glycol by volume can be found by basic interpolation using the following data obtained from [32], shown in Table B.3.

Table B.3: Thermal conductivity of water-ethylene glycol chart

T (℃)	5	10	15	20	25	30	35	40	45
$k_{WEG}\ W/(m \cdot K)$	0.412	0.417	0.421	0.426	0.430	0.434	0.438	0.442	0.445

T (℃)	50	55	60	65	70	75	80	85	90
$k_{WEG}\ W/(m \cdot K)$	0.449	0.452	0.455	0.458	0.467	0.463	0.466	0.468	0.470

Using the data from the central thermocouple group, the surface values are determined by

$$\Theta_2 \approx b_2 = 9.75℃ \tag{B.22}$$

$$\left.\frac{\partial T_2}{\partial z}\right|_{z=0} \approx m_2 = -202.0\ \frac{℃}{m} \tag{B.23}$$

$$\dot{q}_2'' = -k_c \left.\frac{\partial T_2}{\partial z}\right|_{z=0}$$

$$= -401 \frac{W}{m \cdot K}\left(-202.0\ \frac{℃}{m}\right) \tag{B.24}$$

$$= 81{,}323\ \frac{W}{m^2}$$

$$h_2 = \frac{\dot{q}_2''}{\Theta_2}$$

$$= \frac{81{,}323\ \frac{W}{m^2}}{9.75℃} \tag{B.25}$$

$$= 8{,}341 \frac{W}{m^2 K}$$

$$Nu_{D_n,g} = \frac{h_2 D_n}{k_w}$$

$$= \frac{8{,}341 \ \frac{W}{m^2 K} \cdot 0.003175 \ m}{0.614 \ \frac{W}{m \cdot K}} \tag{B.26}$$

$$= 43.13$$

The local surface values for the sample data are shown in Table B.4 below,

Table B.4: Calculated local surface values

	Upstream	Central	Downstream	Transverse
Θ(℃)	10.30	9.75	9.83	9.66
$\dot{q}'' \ (kW/m^2)$	59,348	81,323	84,932	67,769
$h \ (kW/m^2 \cdot K)$	5,761	8,341	8,643	7,015
Nu_{D_n}	29.79	43.13	44.69	36.27

B.2 Calculating Average Surface Values

In Table B.5 a complete list of local surface values at all 9 test locations, or 36 data points is provided. These numbers were determined through the process in detailed Appendix B.1, with notations regarding the geometric features of the tested plate as well as the streamwise and transverse thermocouple positions relative to the central nozzle when data was obtained.

Table B.5 Sample local surface value data, streamwise staggered, water

$\gamma(°)$	P^*	H^*	L_n^*	Re_{D_n}	x^*	y^*	Θ(℃)	$\dot{q}''$ (kW/m^2)	h $(kW/m^2 \cdot K)$	Nu_{D_n}
5	6	1	0	14,000	-4	-1	9.62	72.77	7.57	32.99
5	6	1	0	14,000	-4	0	9.46	74.53	7.98	41.27
5	6	1	0	14,000	-4	1	9.26	71.67	7.32	37.86
5	6	1	0	14,000	-3	-1	9.46	73.81	7.82	40.46
5	6	1	0	14,000	-3	0	9.25	73.06	7.63	39.48
5	6	1	0	14,000	-3	1	9.62	72.49	7.48	38.66
5	6	1	0	14,000	-2	-1	9.63	72.40	7.62	39.39
5	6	1	0	14,000	-2	0	8.98	72.85	7.70	39.83
5	6	1	0	14,000	-2	1	9.34	71.88	7.40	38.24
5	6	1	0	14,000	-1	-1	9.26	83.19	8.98	32.36
5	6	1	0	14,000	-1	0	9.72	85.11	9.48	49.03
5	6	1	0	14,000	-1	1	9.41	82.99	8.85	45.77
5	6	1	0	14,000	-1	2	9.79	63.43	6.48	33.36
5	6	1	0	14,000	-1	3	9.70	72.12	7.88	40.74
5	6	1	0	14,000	-1	4	9.27	73.44	7.81	40.38
5	6	1	0	14,000	0	-1	9.57	85.13	9.30	48.10
5	6	1	0	14,000	0	0	9.54	84.01	9.06	46.86
5	6	1	0	14,000	0	1	9.44	84.10	8.92	46.14
5	6	1	0	14,000	0	2	9.40	64.96	6.85	35.43
5	6	1	0	14,000	0	3	9.79	61.79	6.45	33.36
5	6	1	0	14,000	0	4	9.30	70.71	7.48	38.65
5	6	1	0	14,000	1	-1	9.79	87.43	9.50	49.15
5	6	1	0	14,000	1	0	9.20	86.46	9.40	48.62
5	6	1	0	14,000	1	1	9.15	84.27	8.96	46.32
5	6	1	0	14,000	1	2	9.69	71.41	7.56	39.11

5	6	1	0	14,000	1	3	9.20	70.74	7.61	39.33
5	6	1	0	14,000	1	4	9.38	71.58	7.53	38.92
5	6	1	0	14,000	2	-1	9.59	61.22	6.38	31.94
5	6	1	0	14,000	2	0	9.40	65.55	7.09	36.65
5	6	1	0	14,000	2	1	9.42	62.53	6.49	33.58
5	6	1	0	14,000	3	-1	9.50	67.45	7.07	36.56
5	6	1	0	14,000	3	0	9.48	63.84	6.59	34.08
5	6	1	0	14,000	3	1	9.51	61.26	6.18	31.94
5	6	1	0	14,000	4	-1	9.88	63.43	6.48	33.51
5	6	1	0	14,000	4	0	9.15	61.55	6.26	32.36
5	6	1	0	14,000	4	1	9.43	63.97	6.47	33.47

Average surface values were obtained by numerically integrating local surface values over the area of interest, shown in Figure 3.7. For the sake of example, the average heat transfer coefficient is shown below. Average heat flux from the surface and average Nusselt number are determined by the same method.

$$\bar{h} = \frac{2}{(P^*)^2} \int_{-\frac{p^*}{2}}^{\frac{p^*}{2}} \int_{0}^{\frac{p^*}{2}} h dy^* dx^* \tag{B.27}$$

The unit cell used for the central jet is not completely represented by the sampled data, leaving roughly a third of the area of interest misrepresented in the above location. This would generate artificially high heat transfer results, so the available information was used to create best guess values for the missing locations within the relevant area. The supplemented values were determined by averaging the known values at approximately the same radial distance along the surface from the origin. The formulaic estimates were determined to be:

$$h_{(-3,2)} \approx h_{(-4,1)} \tag{B.28}$$

$$h_{(-3,3)} \approx \frac{h_{(-4,1)} + h_{(-1,4)}}{2} \tag{B.29}$$

$$h_{(-2,2)} \approx \frac{h_{(-3,1)} + h_{(-1,3)}}{2} \tag{B.30}$$

$$h_{(-2,3)} \approx h_{(-1,4)} \tag{B.31}$$

$$h_{(2,2)} \approx \frac{h_{(3,1)} + h_{(1,3)}}{2} \tag{B.32}$$

$$h_{(2,3)} \approx h_{(1,4)} \tag{B.33}$$

$$h_{(3,2)} \approx h_{(4,1)} \tag{B.34}$$

$$h_{(3,3)} \approx \frac{h_{(4,1)} + h_{(1,4)}}{2} \tag{B.35}$$

Using the information in Table B.5 and equations B.28-35 the approximated values were determined and inserted into Table B.6.

Table B.6: Estimated local surface values

$\gamma(°)$	P^*	H^*	L_n^*	Re_{D_n}	x^*	y^*	Θ(℃)	$\dot{q}''\ (kW/m^2)$	$h\ (kW/m^2 \cdot K)$	Nu_{D_n}
5	6	1	0	14,000	-3	2	9.62	72.77	7.57	32.99
5	6	1	0	14,000	-3	3	9.27	72.56	7.57	39.12
5	6	1	0	14,000	-2	2	9.66	72.31	7.68	39.70
5	6	1	0	14,000	-2	3	9.27	73.44	7.81	40.38
5	6	1	0	14,000	2	2	9.36	66.00	6.90	35.64
5	6	1	0	14,000	2	3	9.38	71.58	7.53	38.92
5	6	1	0	14,000	3	2	9.43	63.97	6.47	33.47
5	6	1	0	14,000	3	3	9.41	67.78	7.00	36.20

Now that the area of interest is sufficiently populated with values a 2-D rectangle rule calculation can be applied to perform the integration. Each value was used to represent an area bounded by the midpoints between its locations and the neighboring ones. In this method, the area of the measurement cell is multiplied by the magnitude of the attributed value, averaged by a $P^* \times P^*$ unit cell for the jet. The result is the average surface value for the jet.

$$\bar{h} = \frac{2}{(P^*)^2} \sum_{x^*=-\frac{p^*}{2}}^{\frac{p^*}{2}} \sum_{y^*=0}^{\frac{p^*}{2}} h_{(x^*,y^*)} \cdot A_{(x^*,y^*)} \tag{B.36}$$

$$A_{(x^*,y^*)} = \begin{cases} \Delta x^* \cdot \Delta y^* & |x^*| < \frac{P^*}{2} \, and \; 0 < y^* < \frac{P^*}{2} \\ \frac{\Delta x^* \cdot \Delta y^*}{2} & |x^*| < \frac{P^*}{2} \, and \; y^* = 0 \; or \frac{P^*}{2} \\ \frac{\Delta x^* \cdot \Delta y^*}{2} & |x^*| = \frac{P^*}{2} \, and \; 0 < y^* < \frac{P^*}{2} \\ \frac{\Delta x^* \cdot \Delta y^*}{2} & |x^*| = \frac{P^*}{2} \, and \; y^* = 0 \; or \frac{P^*}{2} \end{cases} \tag{B.37}$$

Using the data provided in Table B.5, the integration is conducted below as

$$\begin{aligned} \bar{h} = \frac{2\Delta x^* \cdot \Delta y^*}{(P^*)^2} \Big(& \frac{h_{(-3,0)}}{4} + \frac{h_{(-2,0)}}{2} + \frac{h_{(-1,0)}}{2} + \frac{h_{(0,0)}}{2} + \frac{h_{(1,0)}}{2} + \frac{h_{(2,0)}}{2} + \frac{h_{(3,0)}}{4} \\ & \ldots + \frac{h_{(-3,1)}}{2} + h_{(-2,1)} + h_{(-1,1)} + h_{(0,1)} + h_{(1,1)} + h_{(2,1)} + \frac{h_{(3,1)}}{2} \\ & \ldots + \frac{h_{(-3,2)}}{2} + h_{(-2,2)} + h_{(-1,2)} + h_{(0,2)} + h_{(1,2)} + h_{(2,2)} + \frac{h_{(-3,2)}}{2} \\ & \ldots + \frac{h_{(-3,3)}}{4} + \frac{h_{(-2,3)}}{2} + \frac{h_{(-1,3)}}{2} + \frac{h_{(0,3)}}{2} + \frac{h_{(1,3)}}{2} + \frac{h_{(2,3)}}{2} + \frac{h_{(3,3)}}{4} \Big) \end{aligned} \tag{B.38}$$

$$\bar{h} = \frac{2}{36}\left(\frac{7.63}{4} + \frac{7.70}{2} + \frac{9.48}{2} + \frac{9.06}{2} + \frac{9.40}{2} + \frac{7.09}{2} + \frac{6.59}{4}\right.$$
$$\ldots + \frac{7.48}{2} + 7.40 + 8.85 + 8.92 + 8.96 + 6.49 + \frac{6.18}{2}$$
$$\ldots + \frac{7.57}{2} + 7.68 + 6.48 + 6.85 + 7.56 + 6.90 + \frac{7.57}{2} \tag{B.39}$$
$$\left.\ldots + \frac{7.57}{4} + \frac{7.81}{2} + \frac{7.88}{2} + \frac{6.45}{2} + \frac{7.61}{2} + \frac{7.53}{2} + \frac{7.00}{4}\right)\frac{kW}{m^2 \cdot K}$$

$$\bar{h} = 7.655\,\frac{kW}{m^2 \cdot K} \tag{B.40}$$

This value for a $\gamma = 5,\ P^* = 6$ plate can be seen in Table D.1 and Figures D.6, D.9, and D.11 of Appendix D. This plate was compared and contrasted to others in Chapter 4.3

Appendix C

Experimental Uncertainty Analysis

C.1 Determining Thermocouple Uncertainty Using Sequential Perturbations

Thermocouples were calibrated in turn using a thermistor as a reference. A curve fit was applied to the calibrated values. The uncertainty of the calibration fits were used to approximate the uncertainty of the temperature measurements.

$$\delta_{T_1} = \pm(0.0091 \cdot T_1 + 0.569)℃ \quad \text{(C.1)}$$

$$\delta_{T_2} = \pm(0.0109 \cdot T_2 + 0.676)℃ \quad \text{(C.2)}$$

$$\delta_{T_3} = \pm(0.0054 \cdot T_3 + 0.334)℃ \quad \text{(C.3)}$$

$$\delta_{T_4} = \pm(0.0051 \cdot T_4 + 0.318)℃ \quad \text{(C.4)}$$

$$\delta_{T_5} = \pm(0.0034 \cdot T_5 + 0.223)℃ \quad \text{(C.5)}$$

$$\delta_{T_6} = \pm(0.0035 \cdot T_6 + 0.219)℃ \quad \text{(C.6)}$$

$$\delta_{T_7} = \pm(0.0035 \cdot T_7 + 0.221)℃ \quad \text{(C.7)}$$

$$\delta_{T_8} = \pm(0.0049 \cdot T_8 + 0.307)℃ \quad \text{(C.8)}$$

$$\delta_{T_9} = \pm(0.0046 \cdot T_9 + 0.290)℃ \quad \text{(C.9)}$$

$$\delta_{T_{10}} = \pm(0.0085 \cdot T_{10} + 0.527)℃ \quad \text{(C.10)}$$

$$\delta_{T_{11}} = \pm(0.0092 \cdot T_{11} + 0.573)℃ \quad \text{(C.11)}$$

$$\delta_{T_{12}} = \pm(0.0115 \cdot T_{12} + 0.718)℃ \quad \text{(C.12)}$$

Each run of the experiment was allowed to reach steady state. The several hundred readings taken at steady state were averaged for the steady state temperature. The uncertainty of the average temperature values was calculated using a method of sequential perturbations described by Moffat [33,34].

This method is somewhat similar to a root-mean-square method, but adjusted to account for a range of uncertainty. The general expression for this is given as

$$\delta_X = \pm\sqrt{\sum_i \left(\frac{|X_O - X_{i+\delta_i}| + |X_O - X_{i-\delta_i}|}{2}\right)^2} \tag{C.13}$$

where X_O is a given measurement ignoring uncertainty, $X_{i+\delta_i}$ is the value of the i^{th} measurement plus the uncertainty, and $X_{i-\delta_i}$ is the value of the i^{th} measurement minus the uncertainty. In the context of these thermocouple measurements, X_O would be the average temperature calculated from the several hundred, $X_{i+\delta_i}$ would be the i^{th} measurement plugged into whichever equation C.1-12 corresponds to the thermocouple and added to itself, and $X_{i-\delta_i}$ would be the i^{th} measurement plugged into whichever equation C.1-12 corresponds to the thermocouple and subtracted from itself. Considering the stark number of measurements involved, these calculations are not demonstrated.

The average uncertainties come out to be:

$$\delta_{T_{1,avg}} = \pm 0.054℃ \quad \delta_{T_{2,avg}} = \pm 0.064℃ \quad \delta_{T_{3,avg}} = \pm 0.032℃ \tag{C.14}$$

$$\delta_{T_{4,avg}} = \pm 0.030℃ \quad \delta_{T_{5,avg}} = \pm 0.021℃ \quad \delta_{T_{6,avg}} = \pm 0.021℃ \tag{C.15}$$

$$\delta_{T_{7,avg}} = \pm 0.021℃ \quad \delta_{T_{8,avg}} = \pm 0.030℃ \quad \delta_{T_{9,avg}} = \pm 0.027℃ \tag{C.16}$$

$$\delta_{T_{10,avg}} = \pm 0.050℃ \quad \delta_{T_{11,avg}} = \pm 0.054℃ \quad \delta_{T_{12,avg}} = \pm 0.068℃ \tag{C.17}$$

C.2 Local Surface Measurement Uncertainties

A method of applying a linear fit to thermocouple measurements to predict temperature and temperature gradient at the surface was outlined in Appendix B.1. The values were then used to display how surface heat flux and heat transfer coefficients could be calculated. The method of sequential perturbations is able to use temperature uncertainty values from equations C.14-C.17 to identify uncertainties for heat flux and heat transfer coefficient as well. Typical values for these uncertainties are:

$$\delta_{\Theta_{s,1}} = \pm 1.07\% \qquad \delta_{\dot{q}''_{s,1}} = \pm 7.72\% \qquad \delta_{h_1} = \pm 8.73\% \tag{C.18}$$

$$\delta_{\Theta_{s,2}} = \pm 1.24\% \qquad \delta_{\dot{q}''_{s,2}} = \pm 7.63\% \qquad \delta_{h_2} = \pm 8.76\% \tag{C.19}$$

$$\delta_{\Theta_{s,3}} = \pm 1.15\% \qquad \delta_{\dot{q}''_{s,3}} = \pm 6.40\% \qquad \delta_{h_3} = \pm 7.42\% \tag{C.20}$$

$$\delta_{\Theta_{s,4}} = \pm 1.14\% \qquad \delta_{\dot{q}''_{s,4}} = \pm 7.70\% \qquad \delta_{h_4} = \pm 8.77\% \tag{C.21}$$

Where $\delta_{\Theta_{s,i}}$ is the uncertainty in the local temperature rise at the surface, $\delta_{\dot{q}''_{s,i}}$ is the uncertainty in the local heat flux at the surface, and δ_{h_i} is the uncertainty of local heat transfer coefficient for the i^{th} location.

C.3 Surface Average Measurement Uncertainties

The mean heat transfer coefficient and mean Nusselt number for each case were determined through a double integration demonstrated in Appendix B.2. The method of sequential perturbations is again used to determine the uncertainties of the average heat transfer coefficients, the values typically come out to be:

$$\delta_{\bar{h}} = \pm 2.50\% \quad for \quad P^* = 4 \tag{C.22}$$

$$\delta_{\bar{h}} = \pm 1.89\% \quad for \quad P^* = 6 \tag{C.23}$$

The region of interest involved in the integration contains a varying number of local measurements depending on the value of pitch, P^*. The are of interest for larger pitch values contain more measurements, which means each individual measurement's uncertainty is less impactful than a small pitch value's area of interest.

Appendix D

Experimental Results

D.1 Experimental Data Summary

Experimentally obtained results are presented in the form of numerical values in table D.1. Each listing includes geometry and both average and local maximum values for both heat transfer coefficient and Nusselt number. Each geometry and Reynolds value required testing a 9 locations, for 36 surface measurements and was actively running for at least 4.5 hours per each row on the table. Streamwise staggered and transverse staggered will be abbreviated to 'stream' and 'tverse' for simplicity.

Table D.1: Summary of experimental data

Fluid	Pattern	γ	P^*	H^*	Re_{D_n}	$\bar{h}\left(\frac{W}{m^2K}\right)$	$h_{max}\left(\frac{W}{m^2K}\right)$	$\overline{Nu}_{D_n}$	$Nu_{D_{n,max}}$
WEG	inline	0	6	1	5100	4,143	5,659	30.29	41.38
WEG	inline	5	6	1	2050	2,563	3,345	18.74	24.47
WEG	inline	5	6	1	3000	3,002	3,901	21.96	28.53
WEG	inline	5	6	1	4050	3,247	4,107	23.75	30.03
WEG	inline	5	6	1	5100	3,237	4,248	23.67	31.06
WEG	inline	5	6	2	5100	2,958	3,883	21.63	28.41
WEG	inline	10	6	1	5100	3,967	4,903	29.00	35.85
water	stream	5	3	1	8400	7,825	14,247	40.50	73.74
water	stream	5	3	1	11200	9,236	14,872	47.81	76.97
water	stream	5	3	1	14000	11,041	19,479	57.14	100.81
water	stream	2.5	4	1	5600	6,380	10,958	33.02	56.72
water	stream	2.5	4	1	8400	7,669	13,138	39.70	68.01

Fluid	Pattern	γ	P^*	H^*	Re_{D_n}	$\bar{h}\left(\frac{W}{m^2K}\right)$	$h_{max}\left(\frac{W}{m^2K}\right)$	$\overline{Nu}_{D_n}$	$Nu_{D_{n,max}}$
water	stream	2.5	4	1	11200	8,902	15,596	46.07	80.71
water	stream	2.5	4	1	14000	9,952	18,020	51.50	93.23
water	stream	5	4	1	5600	5,779	7,195	29.90	37.22
water	stream	5	4	1	8400	7,145	9,419	36.98	48.74
water	stream	5	4	1	11200	8,396	10,875	43.45	56.28
water	stream	5	4	1	14000	9,527	12,388	49.30	64.10
water	stream	7.5	4	1	5600	6,344	8,219	32.78	42.46
water	stream	7.5	4	1	8400	7,985	10,208	41.33	52.83
water	stream	7.5	4	1	11200	9,449	12,733	48.90	65.89
water	stream	7.5	4	1	14000	11,124	14,590	57.56	75.48
water	stream	2.5	6	1	5600	3,995	5,093	20.67	26.36
water	stream	2.5	6	1	8400	5,087	6,494	26.33	33.62
water	stream	2.5	6	1	11200	6,039	7,599	31.26	39.34
water	stream	2.5	6	1	14000	6,929	8,509	35.86	44.03
water	stream	5	6	1	5600	4,631	6,237	23.91	32.20
water	stream	5	6	1	8400	5,879	7,590	30.37	39.20
water	stream	5	6	1	11200	6,890	8,705	35.59	44.95
water	stream	5	6	1	14000	7,661	9,504	39.57	49.07
water	stream	7.5	6	1	5600	6,040	20,862	31.26	107.97
water	stream	7.5	6	1	8400	7,890	27,446	40.84	142.07
water	stream	7.5	6	1	11200	9,489	34,478	49.11	178.44
water	stream	7.5	6	1	14000	10,930	40,389	56.57	209.04
water	tverse	2.5	6	1	5600	4,675	6,456	24.19	33.31
water	tverse	2.5	6	1	8400	6,034	8,145	31.23	42.15
water	tverse	2.5	6	1	11200	7,115	9,766	36.82	50.54
water	tverse	2.5	6	1	14000	8,097	11,006	41.90	56.97
water	tverse	5	6	1	5600	3,810	5,745	19.71	29.72
water	tverse	5	6	1	8400	4,663	6,715	24.13	34.76
water	tverse	5	6	1	11200	5,449	8,244	28.20	42.66
water	tverse	5	6	1	14000	6,172	9,232	31.94	47.78
water	tverse	7.5	6	1	5600	4,244	5,882	21.96	30.44
water	tverse	7.5	6	1	8400	5,489	7,483	28.41	38.73
water	tverse	7.5	6	1	11200	6,584	8,721	34.18	45.14
water	tverse	7.5	6	1	14000	7,494	9,958	38.78	51.54

D.2 Experimental Surface Maps

Provided below surface maps generated from local values of experimentally obtained heat transfer data.

- Figures D.1-D.3 display results for water-ethylene glycol results at varying flow rates and geometric parameters.
- Figures D.4 – D.7 display results for staggered arrays at the three largest Reynolds numbers for $\gamma = 5°$ of each staggered geometry tested.
- Figure D.8 displays results for $\gamma = 5°$ for each pitch value of streamwise staggered plate.
- Figure D.9 displays results for $\gamma = 5°$, $P^* = 6$ for both streamwise and transverse staggered plates.
- Figures D.10-D.12 display results for staggered arrays with varying angle for the three patterns tested at all three angles.
- Figure D.13 displays results for staggered arrays with varying Reynolds numbers for $\gamma = 5°$, $P^* = 6$ to demonstrate skewed results just downstream of center. The plate was tested twice with intermediating tests between, showing no concerning results. Only the more recent set of acquired data for this geometry is presented in this study

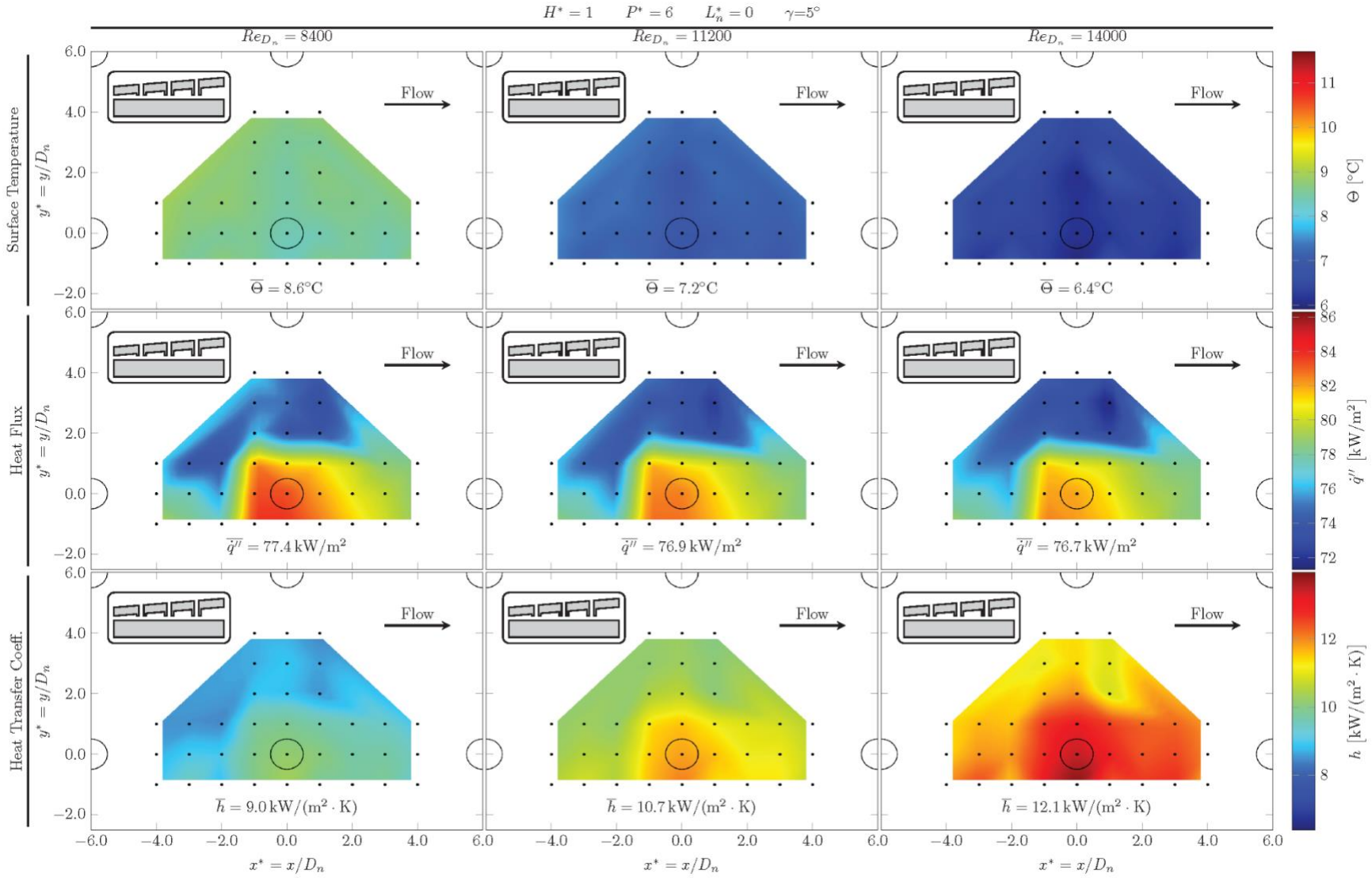

Figure D.1: Water-ethylene glycol over increasing Reynolds numbers

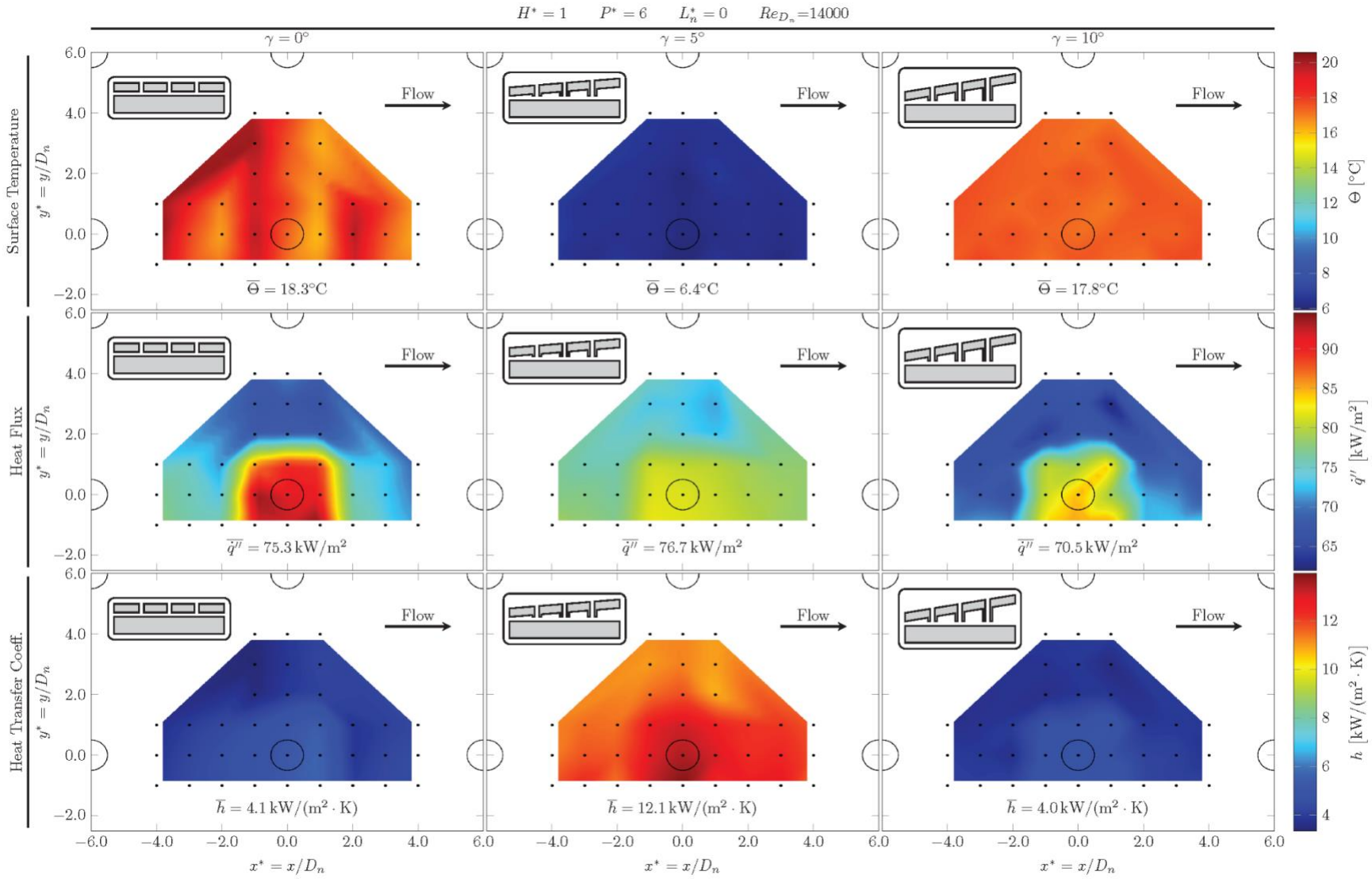

Figure D.2: Water-ethylene glycol over increasing manifold angle

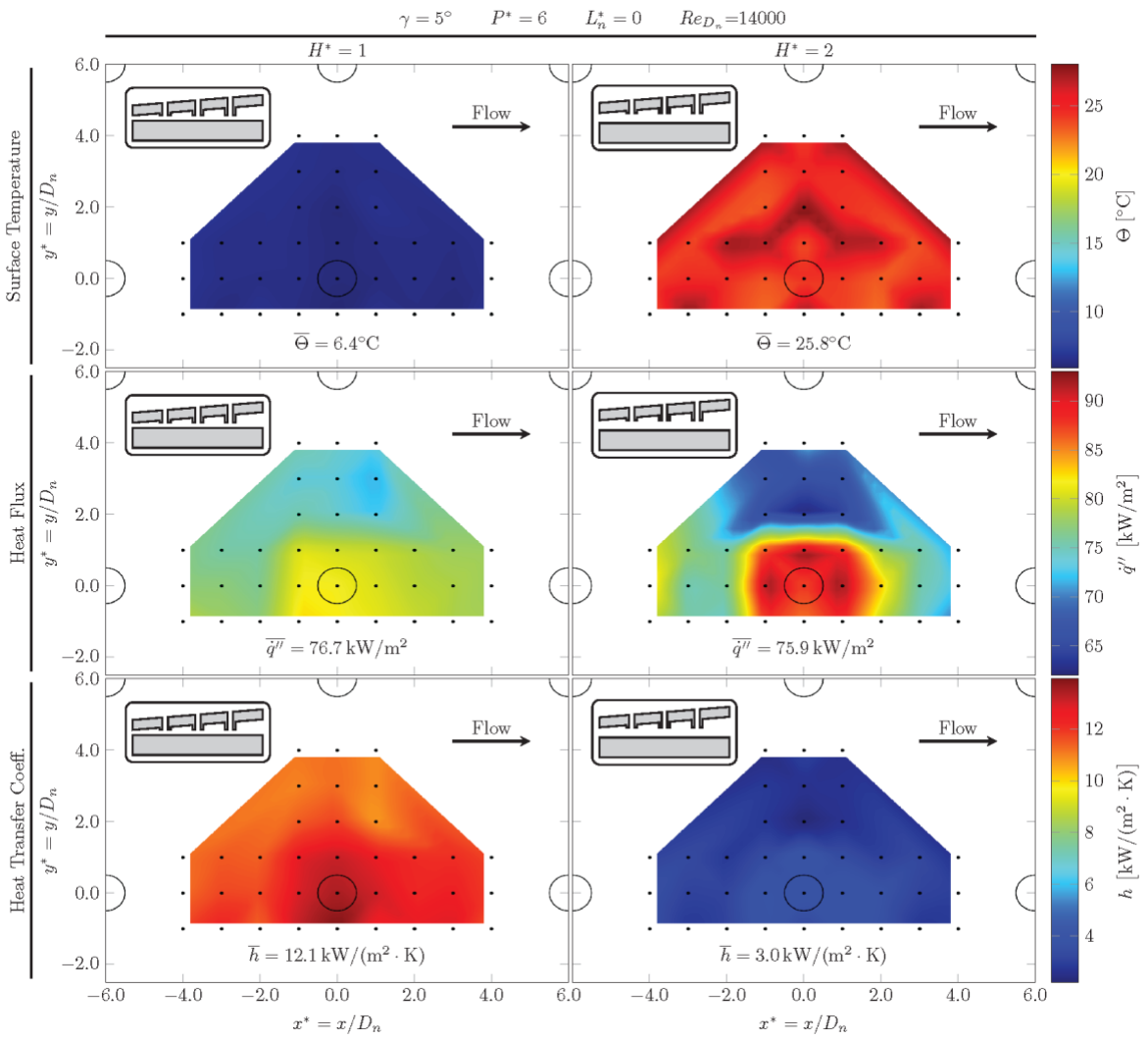

Figure D.3: Water-ethylene glycol with $H^* = 1$ and 2

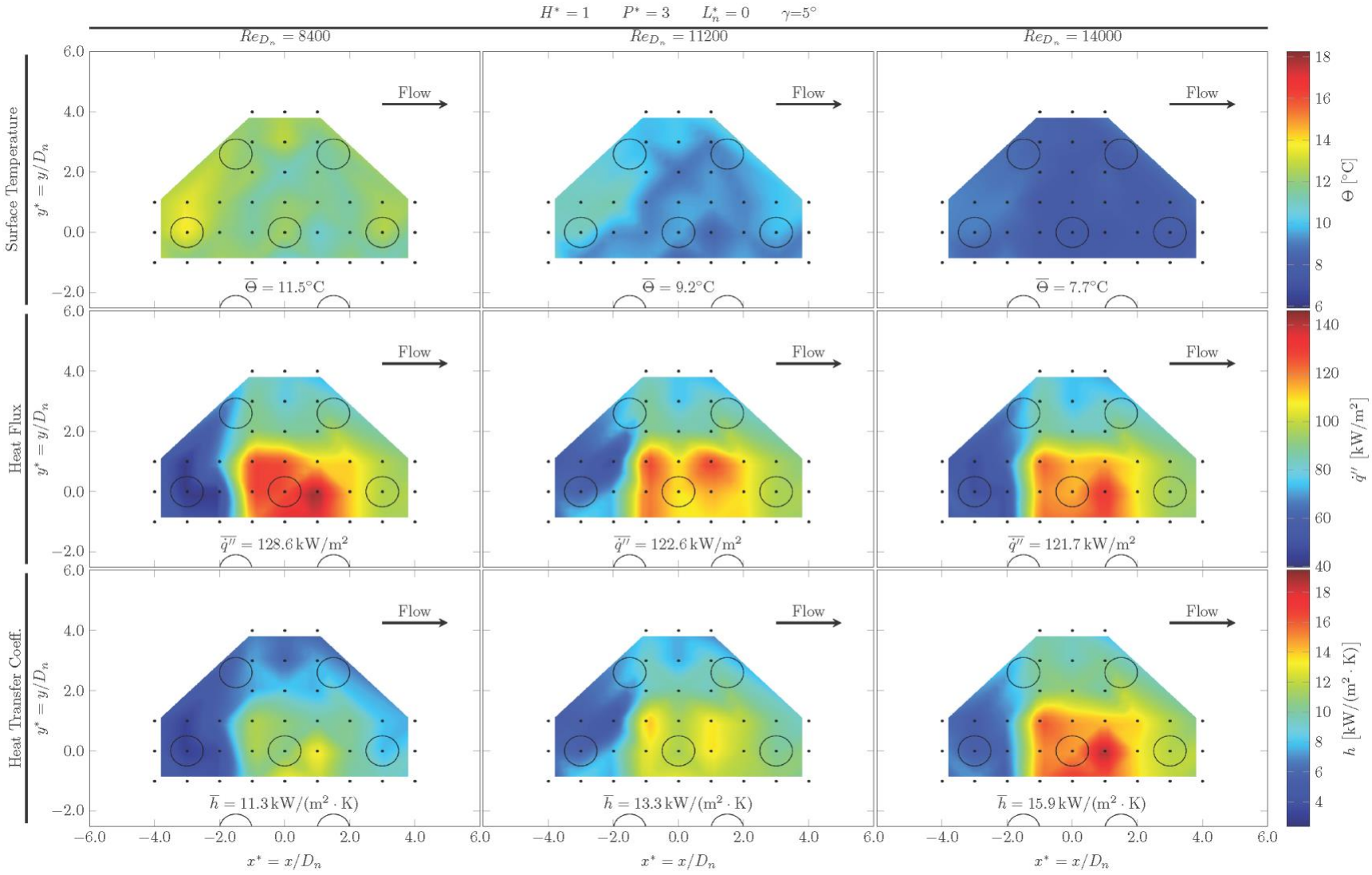

Figure D.4: Streamwise staggered array with $P^* = 3$ and increasing Reynolds number

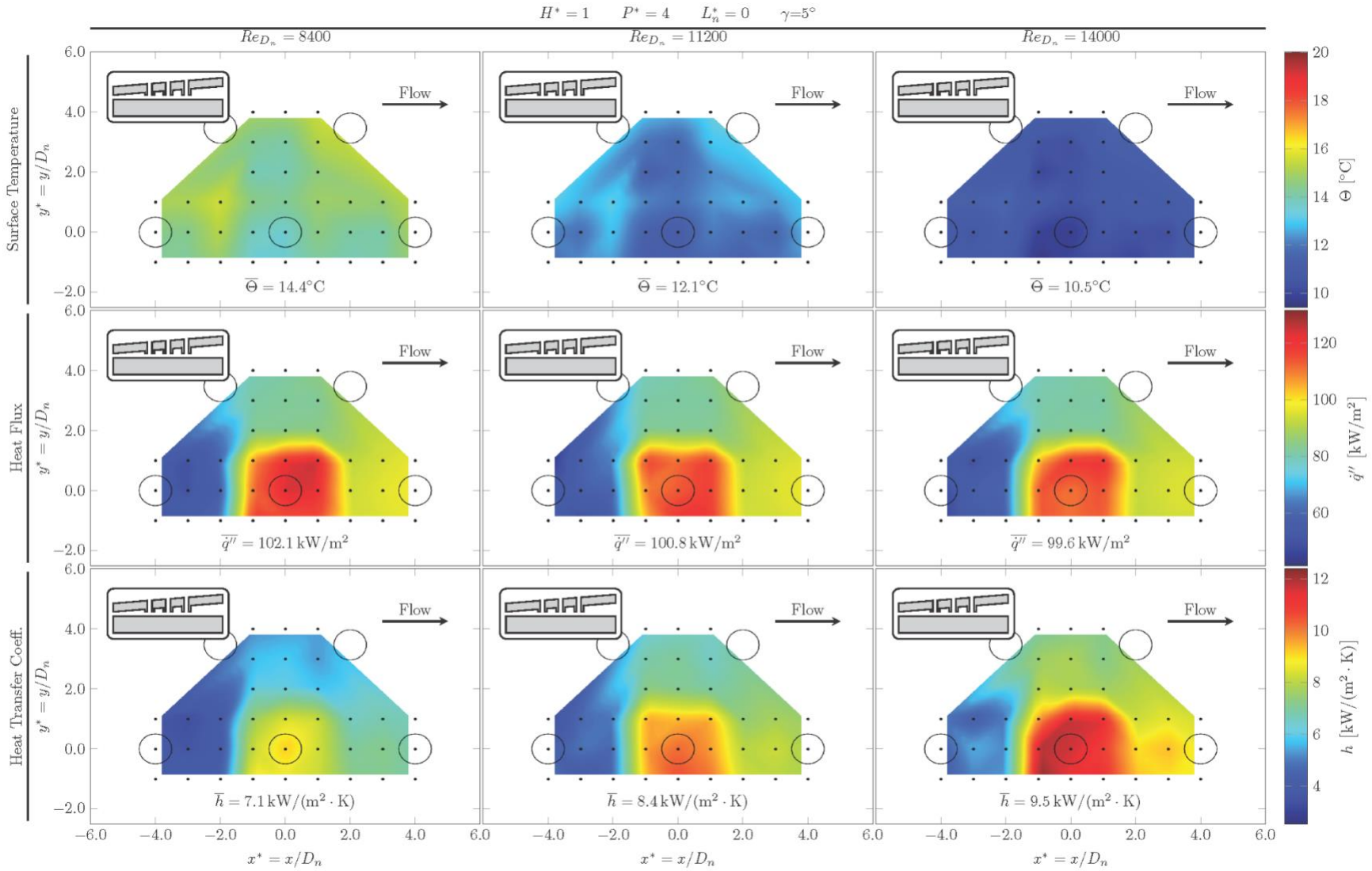

Figure D.5: Streamwise staggered array with $P^* = 4$ and increasing Reynolds number

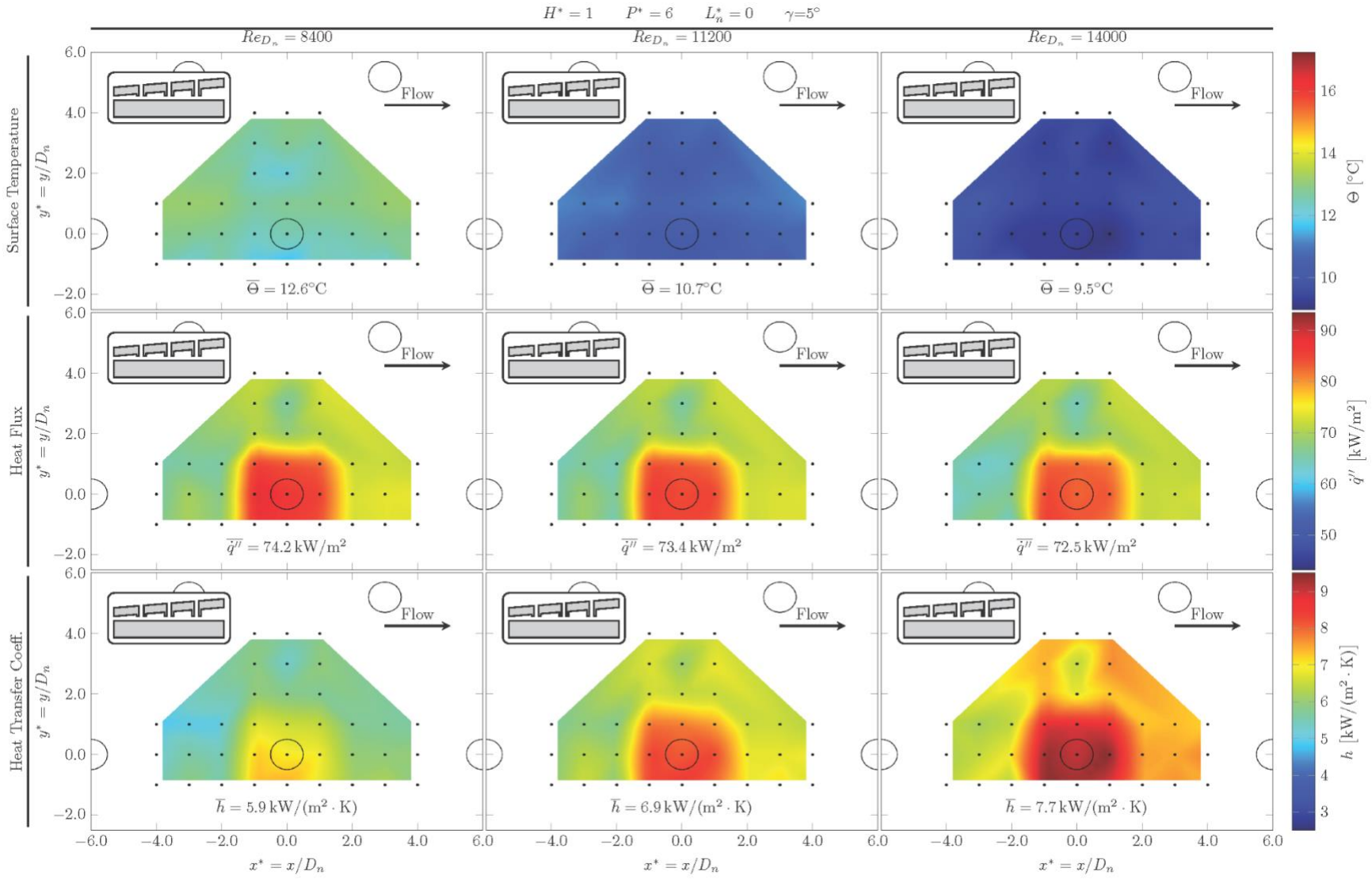

Figure D.6: Streamwise staggered array with $P^* = 6$ and increasing Reynolds number

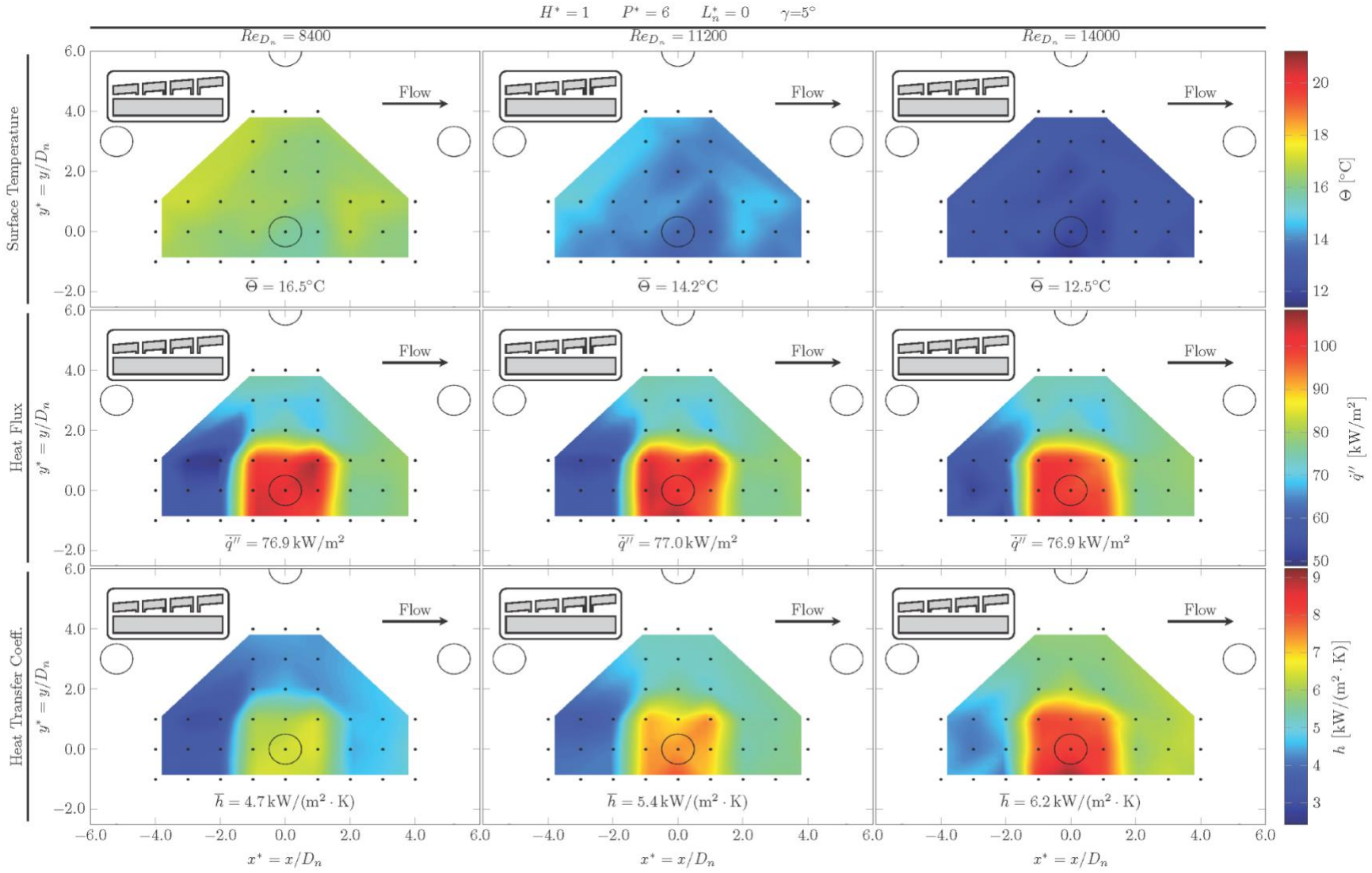

Figure D.7: Transverse staggered array with $P^* = 6$ and increasing Reynolds number

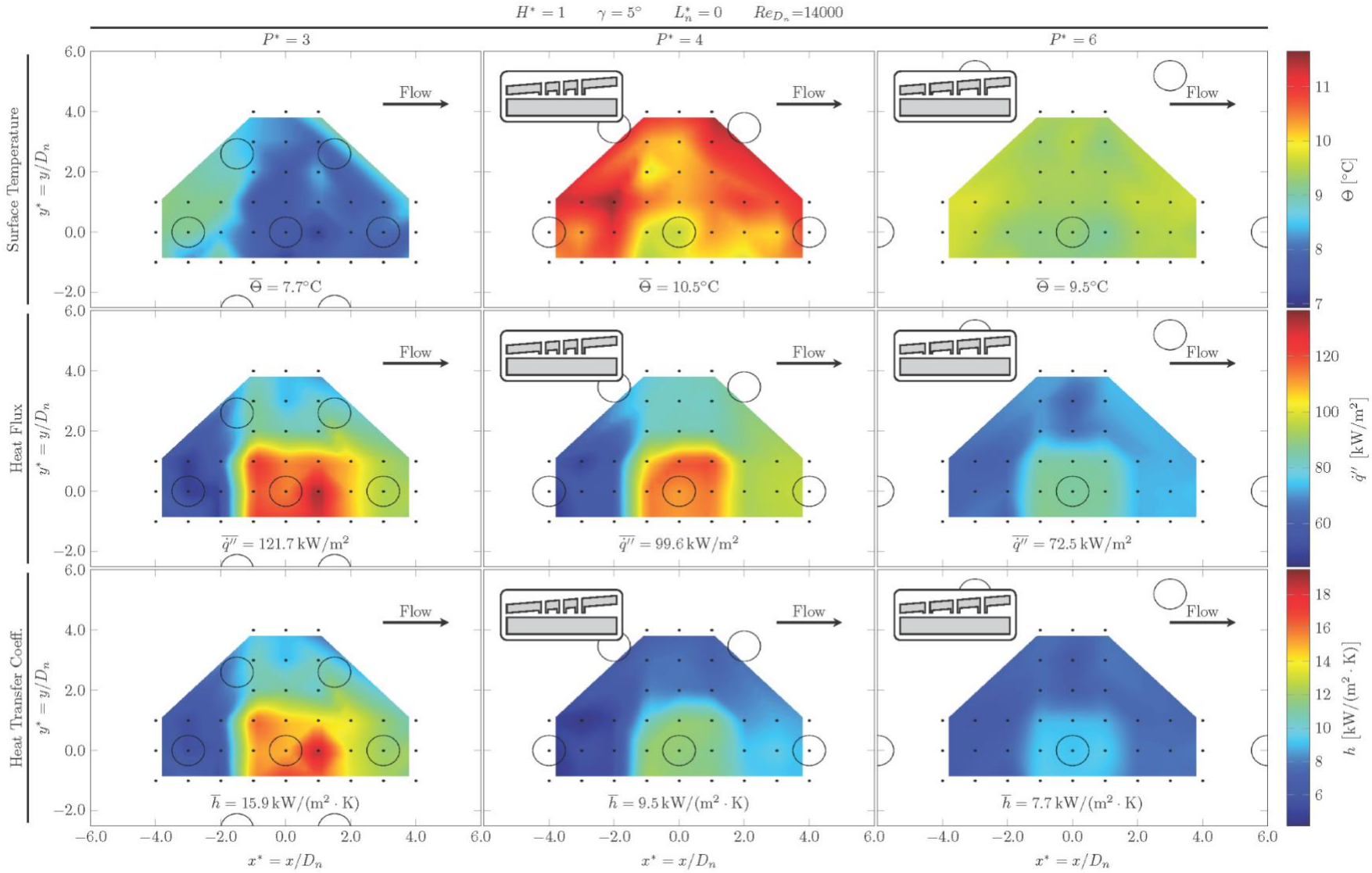

Figure D.8: Streamwise staggered arrays with increasing pitch

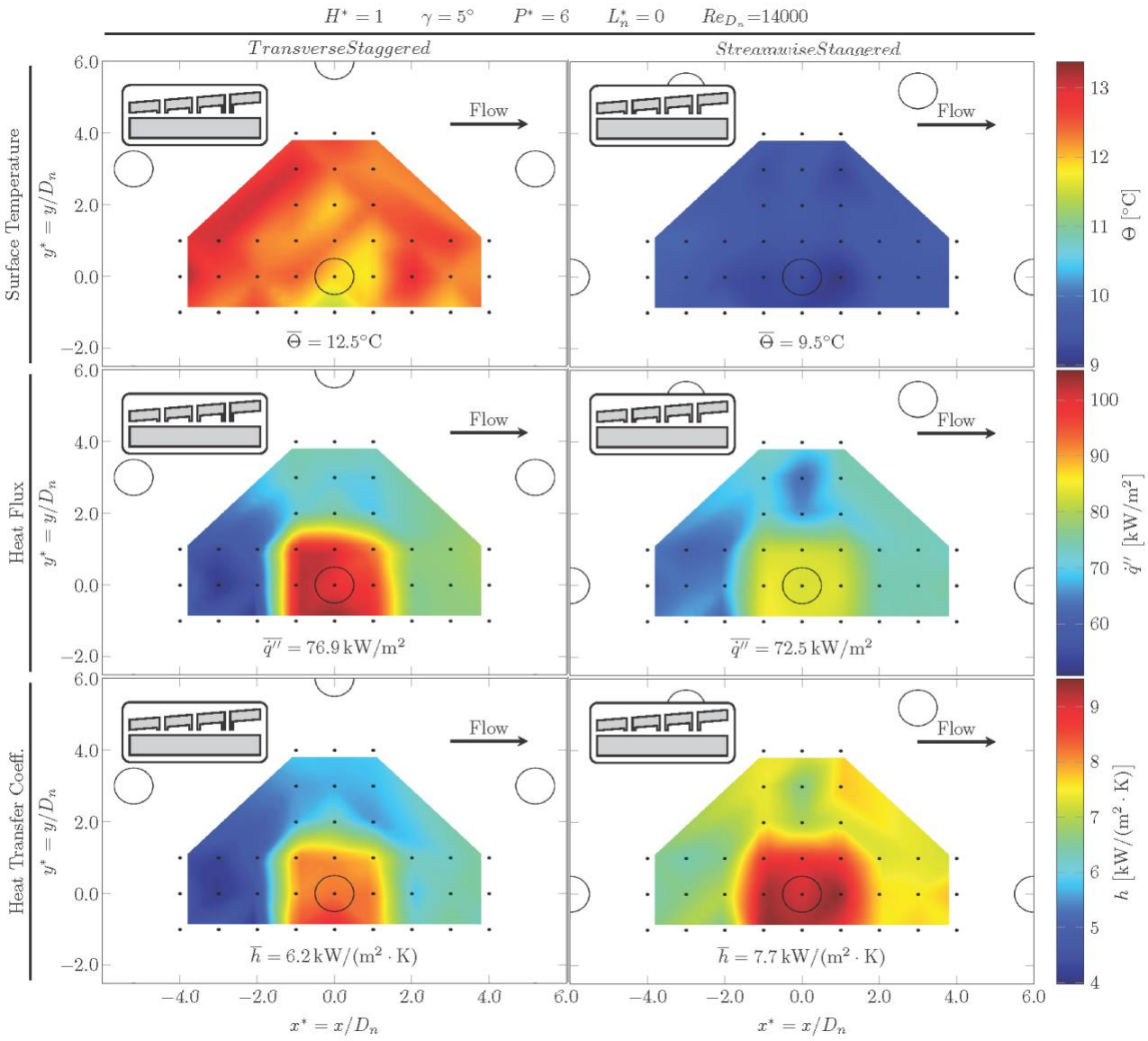

Figure D.9: Streamwise staggered compared to transverse staggered

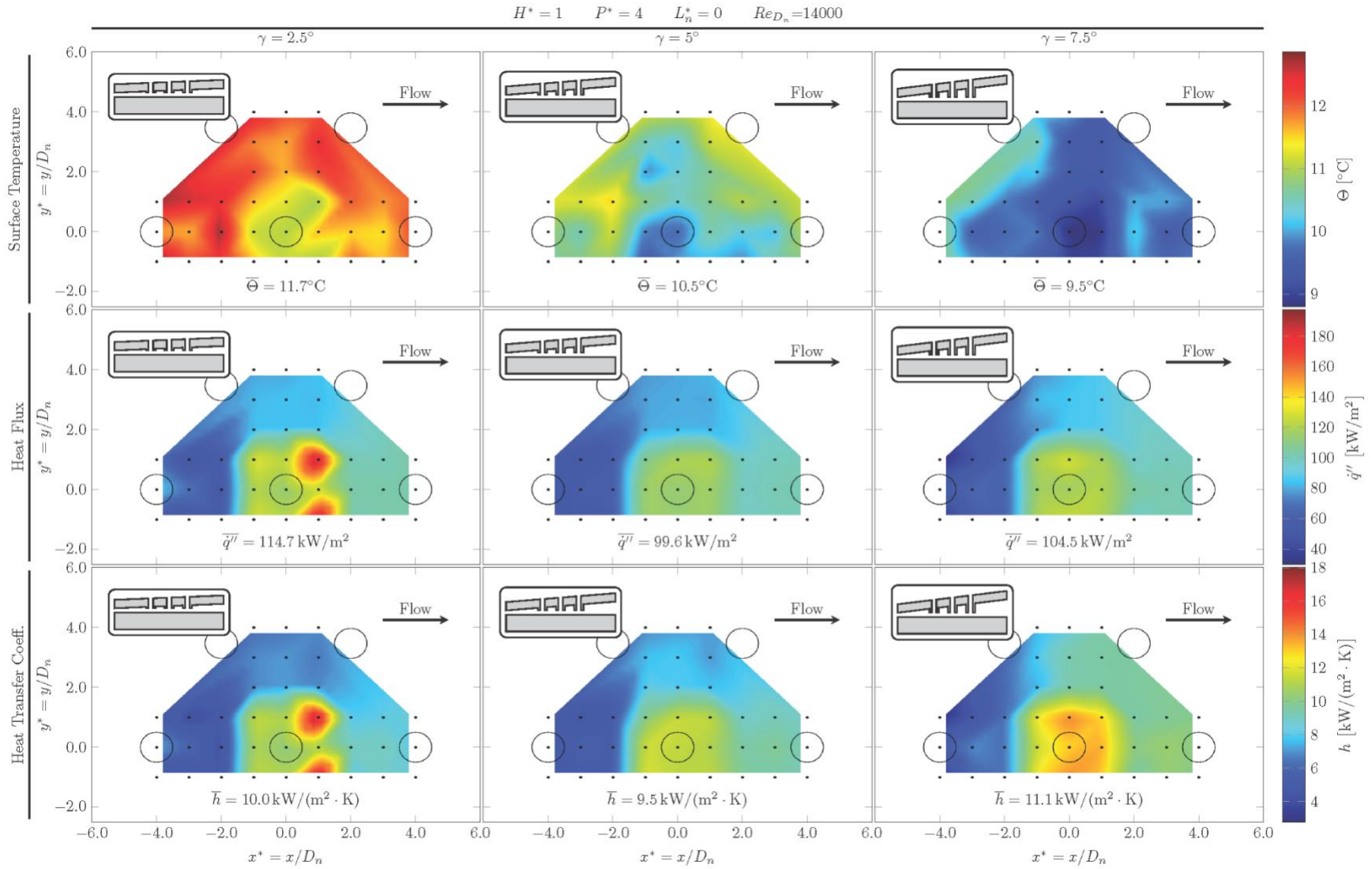

Figure D.10: Streamwise staggered increasing angle with $P^* = 4$

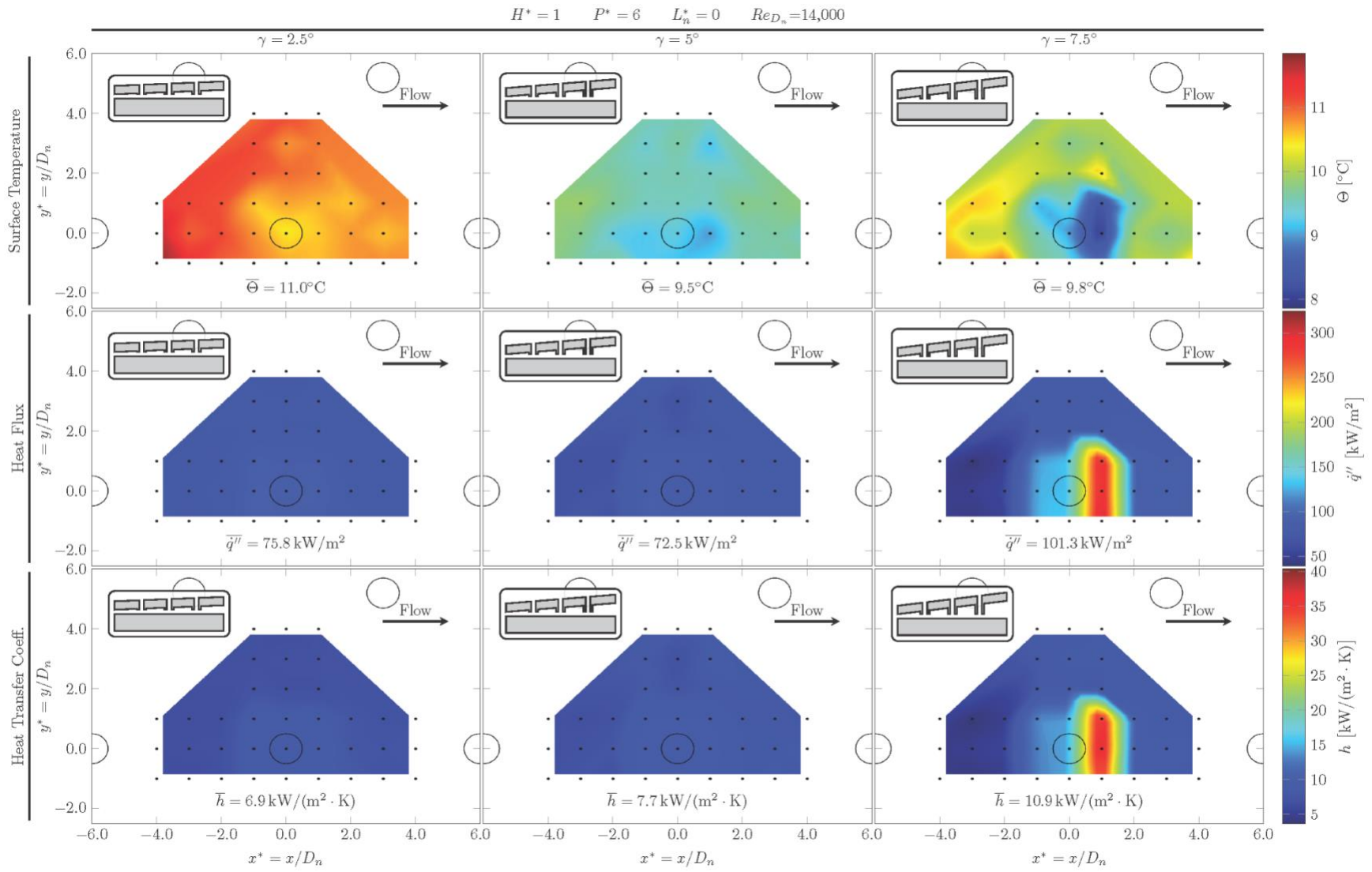

Figure D.11: Streamwise staggered increasing angle with $P^* = 6$

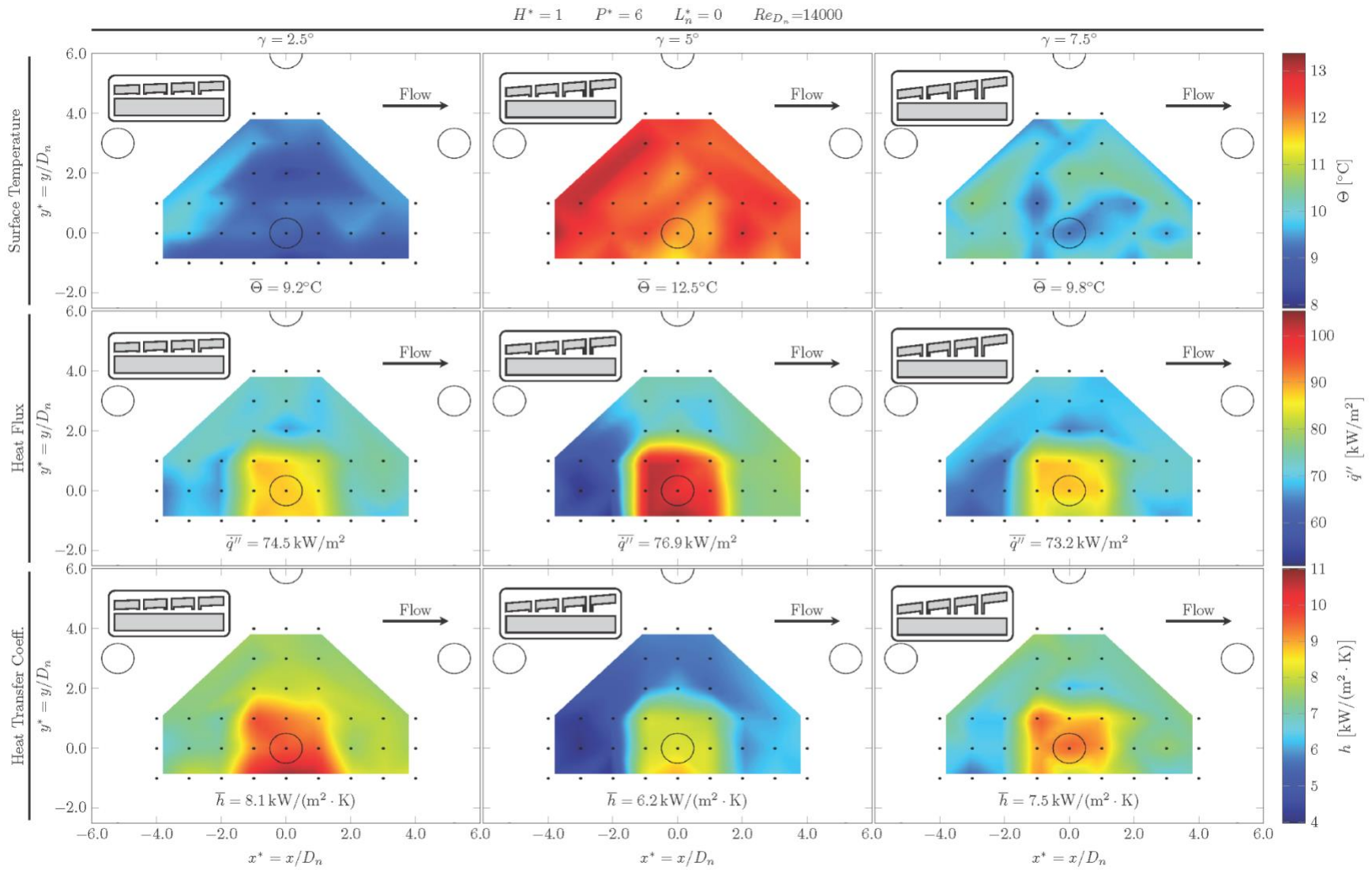

Figure D.12: Transverse staggered increasing angle with $P^* = 6$

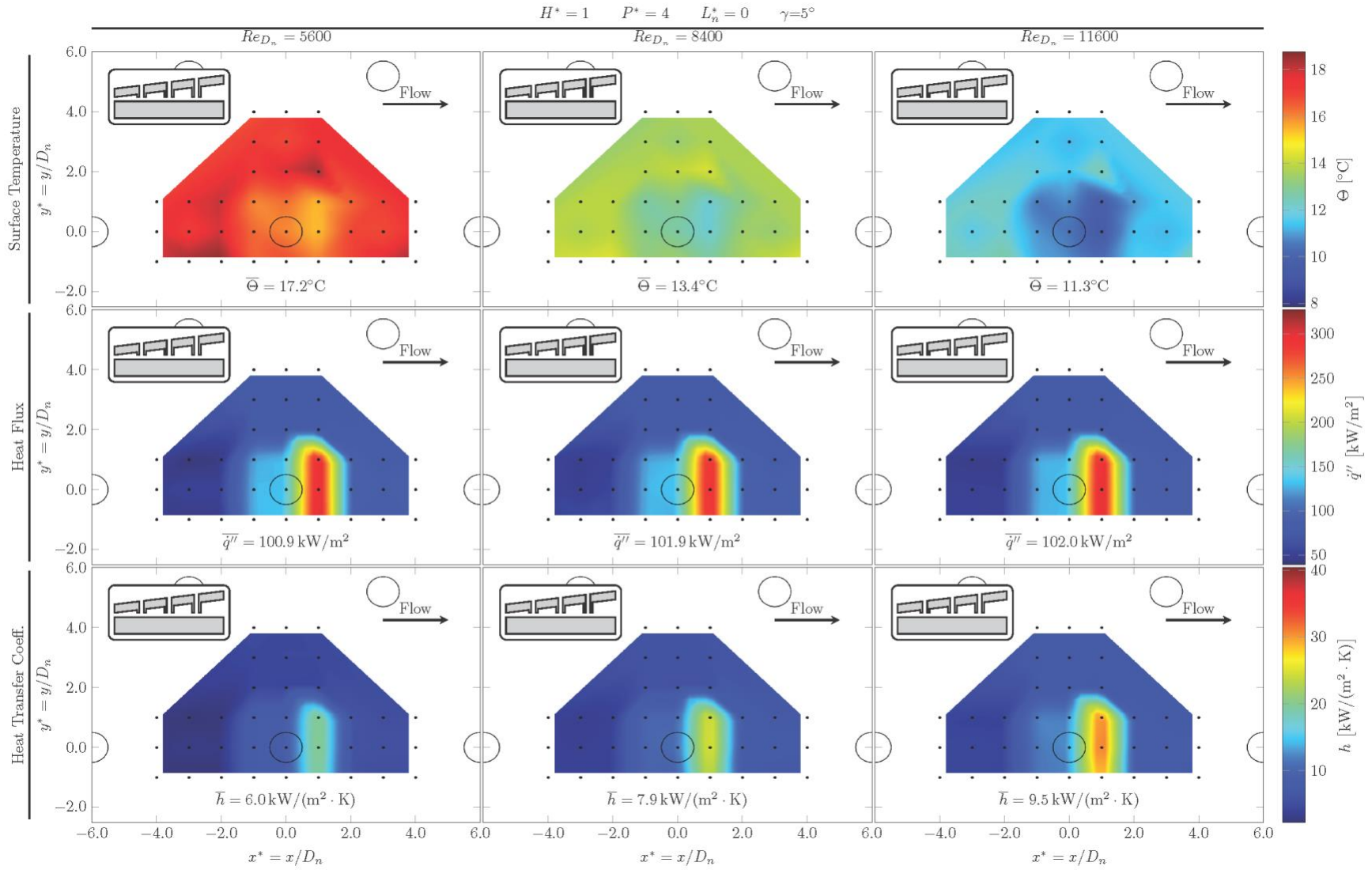

Figure D.13: Streamwise staggered increasing Reynolds number with $\gamma = 7.5°$ and $P^* = 6$